Loudspeakers: Modeling and Control

by

Khalid Mohammad Al-Ali

B.S. (University of Colorado at Boulder) 1993
M.S. (University of California at Berkeley) 1995

A dissertation submitted in partial satisfaction of the
requirements for the degree of
Doctor of Philosophy

in

Engineering-Mechanical Engineering

in the

GRADUATE DIVISION
of the
UNIVERSITY of CALIFORNIA at BERKELEY

Committee in charge:

Professor Andrew K. Packard, Chair
Professor Benson H. Tongue
Professor James M. Kelly

Fall 1999

The dissertation of Khalid Mohammad Al-Ali is approved:

Chair Date

Date

Date

University of California at Berkeley

Fall 1999

Loudspeakers: Modeling and Control

by

Khalid Mohammad Al-Ali

Abstract

Loudspeakers: Modeling and Control

by

Khalid Mohammad Al-Ali

Doctor of Philosophy in Engineering-Mechanical Engineering

University of California at Berkeley

Professor Andrew K. Packard, Chair

This thesis documented a comprehensive study of loudspeaker modeling and control. A lumped-parameter model for a voice-coil loudspeaker in a vented enclosure was presented that derived from a consideration of physical principles. In addition, a low-frequency (20 Hz to 100 Hz), feedback control method designed to improve the nonlinear performance of the loudspeaker and a suitable performance measure for use in design and evaluation were proposed. Data from experiments performed on a variety of actual loudspeakers confirmed the practicality of the theory developed in this work.

The lumped-parameter loudspeaker model, although simple, captured much of the nonlinear behavior of the loudspeaker. In addition, the model formulation allowed a straightforward application of modern control system methods and lent itself well to modern parametric identification techniques.

The nonlinear performance of the loudspeaker system was evaluated using a suitable distortion measure that was proposed and compared with other distortion measures currently used in practice. Furthermore, the linearizing effect of feedback using a linear controller (both static and dynamic) was studied on a class of nonlinear systems. The results illustrated that the distortion reduction was potentially signifi-

cant and a useful upper bound on the closed-loop distortion was found based on the sensitivity function of the system's linearization.

A feedback scheme based on robust control theory was chosen for application to the loudspeaker system. Using the pressure output of the loudspeaker system for feedback, the technique offered significant advantages over those previously attempted.

Illustrative examples were presented that proved the applicability of the theory developed in this dissertation to a variety of loudspeaker systems. The examples included a vented loudspeaker model and actual loudspeakers enclosed in both vented and sealed configurations. In each example, predictable and measurable distortion reduction at the output of the closed-loop system was recorded.

Professor Andrew K. Packard
Dissertation Committee Chair

To my family and friends

Contents

List of Figures

List of Tables

List of Symbols

$\blacksquare$	denotes end of proof
$\forall$	reads "for all"
$:=$	"is defined to be"
$a \in A$	means "a is an element of A"
$a \approx b$	reads "b is an approximation of a"
$a \equiv b$	means "a is identically equal to b"
$a \ll b$	means "a is much less than b"
$a \gg b$	reads "a is much greater than b"
$f : X \to Y$	implies that f is a function mapping the set X into the set Y
$X \cap Y$	the intersection of the sets X and Y
$X \cup Y$	the union of the sets X and Y
$X \subset Y$	means "the set X is a subset of the set Y"
$\{\mathcal{A} : \mathcal{B}\}$	reads "the set of all (*expression* $\mathcal{A}$) such that (*expression* $\mathcal{B}$)",
	e.g. $\{u \in \mathbb{R} : u > 0\}$ is the set of all real, positive numbers
$\{a_n\}_{n=0}^{n=N}$	the sequence $\{a_0, a_1, a_2, \ldots, a_N\}$
$\mathbb{R}$	the set of real numbers
$\mathbb{C}$	the set of complex numbers
$\mathbb{R}_+$	the set of non-negative real numbers
$\mathbb{R}^n$	the set of $n \times 1$ column vectors with real number entries
$\mathbb{R}^{m \times n}$	the set of $m \times n$ matrices with real number entries

$\mathbb{C}^{m\times n}$	the set of $m \times n$ matrices with complex number entries
0_n	the zero element of $\mathbb{R}^n$
$0_{m\times n}$	the zero element of $\mathbb{R}^{m\times n}$
I_n	the $n \times n$ identity matrix
$\mathbb{R}^n/0_n$	the set of $n \times 1$ vectors with the zero vector 0_n excluded
$\mathcal{B}(0, R)$	the closed ball of radius $R > 0$, centered at the origin in n-dimensional Euclidean space
$\partial\mathcal{B}(0, R)$	the boundary of $\mathcal{B}(0, R)$
sup	supremum, the least upper bound
ess sup	the essential supremum
$\mathcal{L}_{1,\mathrm{loc}}$	the space of locally integrable functions
$\mathcal{L}_\infty(\mathbb{R}^n)$	the space of vector-valued functions (e.g. $y : \mathbb{R}^n \to \mathbb{R}^m$) that are measurable and essentially bounded
$\mathcal{C}_c(\mathbb{R}^n)$	the space of vector-valued, continuous functions defined on $\mathbb{R}^n$ with compact support
$\mathcal{C}_c^\infty(\mathbb{R}^n)$	the space of vector-valued, infinitely differentiable functions defined on $\mathbb{R}^n$ with compact support
$\Re(s)$	the real part of the complex number $s \in \mathbb{C}$
M_{ij}	the i, j element of the matrix M
$\bar{\sigma}(M)$	largest singular value of M
$\mathrm{diag}(M_1, \ldots, M_n)$	a block-diagonal matrix with diagonal entries $M_1, \ldots, M_n$
$\det(M)$	the determinant of a square matrix $M \in \mathbb{C}^{n\times n}$
M^T	the transpose of a matrix M
M^{-1}	the inverse of a square matrix $M \in \mathbb{C}^{n\times n}$
$\lvert \cdot \rvert$	absolute value of elements in $\mathbb{R}$ or $\mathbb{C}$
$\lVert v \rVert$	the Euclidean norm of a vector $v \in \mathbb{C}^n$, $\lVert v \rVert := \left(\sum_{i=1}^n \lvert v_i \rvert^2\right)^{\frac{1}{2}}$
$\lVert v \rVert_\infty$	the infinity norm of a vector $v \in \mathbb{C}^n$, $\lVert v \rVert_\infty := \max_{1\le i\le n} \lvert v_i \rvert$

$\|y\|_\infty$	the infinity norm of a vector-valued function $y \in \mathcal{L}_\infty(\mathbb{R})$ with elements y_i, $\|y\|_\infty := \max_i \{\text{ess sup}_{t\in\mathbb{R}} \|y_i(t)\|\}$
$\|P\|_\infty$	$\mathcal{H}_\infty$ norm of a LTI system represented by the transfer function $P(s)$, $\|P\|_\infty := \sup_{\omega\in\mathbb{R}} \bar{\sigma}\left(P(j\omega)\right)$
$G := \left[\begin{array}{c\|c} A & B \\ \hline C & D \end{array}\right]$	the shorthand notation for the state-space representation of a Linear, Time Invariant (LTI) system $\dot{x} = Ax + Bu$, $y = Cx + Du$, where, u, y, x, and $\dot{x}$ are the input, output, state, and state-derivative vectors, respectively. Note that G may also represent the system's transfer function or frequency response, where appropriate
Δ	the *Laplace* operator. For the Cartesian coordinates $(x, y, z) \in \mathbb{R}^3$, $\Delta := \frac{\partial^2}{\partial x^2} + \frac{\partial^2}{\partial y^2} + \frac{\partial^2}{\partial z^2}$, e.g. for $p(x, y, z) : \mathbb{R}^3 \to \mathbb{R}$, $\Delta p := \frac{\partial^2 p}{\partial x^2} + \frac{\partial^2 p}{\partial y^2} + \frac{\partial^2 p}{\partial z^2}$. In spherical coordinates $(r, \theta, \phi) \in \mathbb{R}^3$, $\Delta := \frac{\partial^2}{\partial r^2} + \frac{2}{r}\frac{\partial}{\partial r} + \frac{1}{r^2 \sin^2\phi}\frac{\partial^2}{\partial \theta^2} + \frac{1}{r^2}\frac{\partial^2}{\partial \phi^2} + \frac{\cot\phi}{r^2}\frac{\partial}{\partial \phi}$
$\vec{\nabla}$	the gradient operator. For the Cartesian coordinates $(x, y, z) \in \mathbb{R}^3$, $\vec{\nabla} := \left(\frac{\partial}{\partial x}, \frac{\partial}{\partial y}, \frac{\partial}{\partial z}\right)$, e.g. for $p(x, y, z) : \mathbb{R}^3 \to \mathbb{R}$, $\vec{\nabla} := \left(\frac{\partial p}{\partial x}, \frac{\partial p}{\partial y}, \frac{\partial p}{\partial z}\right)$. In spherical coordinates $(r, \theta, \phi) \in \mathbb{R}^3$, $\vec{\nabla} := \left(\frac{\partial}{\partial r}, \frac{1}{r\sin\phi}\frac{\partial}{\partial \theta}, \frac{1}{r}\frac{\partial}{\partial \phi}\right)$

Acknowledgements

If I were to list all the people who have had an impact on this thesis, I would have to write another dissertation just for that. Therefore, I will only mention those who I am still in touch with and who have given me the most direct help during my graduate career.

First and foremost, I would like to convey my deepest regards and love for my family, especially my parents, Mohammad Al-Ali and Latifa Al-Houty. Their patience, dedication and unbounded affection provided me with the fertile grounds on which this work has reached fruition. Being half a world away from Qatar (my home country) for more than a decade was a difficult task, and it has finally paid off with this.

Also, my friends deserve special attention. To me, friends are some of life's precious treasures. They were there for me during the good times and bad. Of note are the ones that kept in contact with me throughout my student life. They are (in alphabetical order) F. Al-Sumait, H. Al-Thani, R. Carr, A. Darwish, M. Kelly, P. Kohut, D. Kwong, G. McKinney, A. Meziane, J. Mileham, H. Nordskog, C. Petersen, N. Tenbrink, B. Rambo, A. Zaabalawi, and many more. I feel extremely lucky being with such good company.

I am greatly indebted to my advisor, Professor Andrew Packard not only for his contributions, advice, and guidance, but for being such a good friend. He was also an older brother whenever I needed one. He is a mentor that I have come to highly respect and admire. His selfless care and devotion were responsible in taking my research to a "higher level". I am still at awe at how hard he works. My thanks also go to the professors whom I've had the fortune to meet and converse with at Berkeley and Colorado. Special note goes to Professors Benson Tongue, James M. Kelly, and Kameshwar Poolla for their interest in my work. I view them as sources of a great wealth of knowledge that I frequently tapped into. Professor Tongue graciously allowed me the use of his acoustic analysis and measurement equipment for the experiments performed for this dissertation. Sharing much in common, we often discussed a variety of topics of interest, including high-performance automobiles, which we both are passionate about. He is a great friend. Also thanks go to Professors David Auslander, Karl Hedrick, George Johnson, Homayoon Kazerooni, Dorian Liepmann, and Fai Ma for their valued support. Furthermore, I want to take this opportunity to thank the person who has introduced me to this field, Professor Mark Balas, even though he repeatedly apologizes for doing so. His excellent and unique style of teaching the undergraduate courses in controls at the University of Colorado at Boulder has provided me with the solid controls background necessary for this work. Also, thanks to Doug Crawford, my licensing officer at the Office of Technology Licensing at UC Berkeley. His interest in my research and the efforts he put forth may realize a patent protection (currently pending) of some of this work.

Many thanks go to the University of Qatar and the Ministry of Education in Qatar for providing me with perhaps the best academic scholarship, which paid for all my expenses while I was away from home, and offering me a guaranteed faculty position when my career as a student is over. Some support was also provided via the National Science Foundation Grant ECS90-96223.

My list of thanks would be incomplete without mentioning the Berkeley Center for Control and Identification (BCCI), my workplace. Its residents, visitors, and alumni provided me with a productive atmosphere that positively influenced this research. I also consider them as my friends. They had to endure the often loud acoustic tests that I performed on loudspeakers in order to collect the data for this dissertation. That place will always be remembered.

Finally, for all whom I may have omitted here, you also have my deepest regards.

Chapter 1

Introduction

This thesis documents a comprehensive study of loudspeaker modeling and control. A lumped-parameter model for a voice-coil loudspeaker in a vented enclosure is presented that derives from a consideration of physical principles. In addition, a low-frequency, feedback control method designed to improve the nonlinear performance of the loudspeaker and a suitable performance measure for use in design and evaluation are proposed. Data from experiments performed on a variety of actual loudspeakers will be used to confirm the usefulness of the theory developed in this work.

Recent demands in the audio industry include flatter amplitude response and lower nonlinear distortion for the output pressure response of loudspeakers that operate in the low-frequency region (typically from 20 Hz to 100 Hz). Also, modern recording techniques and contemporary playback systems (e.g. Compact Disc (CD) and Digital Versatile Disc (DVD) players) are capable of reproducing signals in the full range of the audible spectrum (from 20 Hz to 20 kHz). Since the weakest link in the chain of components comprising a well designed acoustic reproduction system is usually its loudspeaker system, rigid requirements are placed on the loudspeaker's design, especially at the low frequencies in which some operate. Moreover, loudspeaker systems are limited by their inherent dynamics in low-frequency reproduction and become highly nonlinear well before reaching their maximum acoustic output.

Faithful reproduction of low-frequency signals by conventional loudspeakers requires sophisticated electromechanical design techniques, advanced materials, and tight manufacturing tolerances, necessitating a better understanding of the underlying physical processes that govern their operation. Most of the earlier work in modeling low-frequency, voice-coil loudspeakers treated them as lumped-parameter linear systems as described in [7] for loudspeakers without enclosures, [55], [54], and [57] for loudspeakers in sealed enclosures, [64], [65], and [66] for loudspeakers in vented enclosures, and [41] and [63] for loudspeakers in both sealed and vented boxes. Although the work was ground-breaking, especially in light of the fact that some of these models became industry standards, they are not sufficient in analyzing today's high-performance loudspeakers, which are typically driven beyond their linear output range. More significant was the work by [28], [31], and [33], where lumped-parameter nonlinear models were analyzed.

While modern computers have allowed for the use of complex models based on numerical approximations (e.g. finite element models), these are typically specific to a particular loudspeaker system and are sometimes intractable when dealing with modern system identification and control techniques. For these techniques to apply seamlessly to loudspeakers, the loudspeaker models should be constructed with system analysis and theory in mind. This approach benefits applications where maximum performance is extracted from loudspeakers, such as high-fidelity sound reproduction and active-noise cancellation [26]. In Chapter 2, the current understanding of a loudspeaker's dynamics in the low-frequency region will be extended and clarified by way of a simple nonlinear parametric model that captures much of the behavior of real loudspeakers with nonlinearities. The model will be laid out in a specific structure, each element of which will be individually studied. The model will include loudspeakers in vented enclosures, which can be easily specialized to deal with sealed boxes, as well.

As shown in [14], [27], [48], and [8], the linearizing effect of feedback using a linear controller on some nonlinear systems is widely known, but has only recently been exploited in loudspeakers. In Chapter 3, a suitable measure for the nonlinear distortion of the low-frequency loudspeaker is proposed, analyzed, and compared with distortion measures currently used in practice. Also, the effect of feedback (using both a static and dynamic linear controller) on the distortion in the output of a special class of nonlinear systems is detailed. Results relating to the linear controller are found, including a practical upper-bound on the distortion of the closed-loop system, along with some illustrative examples.

In the past, several control methods have been proposed in order to improve the response of the pressure generated by the loudspeaker system. These methods fall into the following categories:

Direct Inversion: The most straightforward approaches are given by [32], [23], [5], [12] and [10], where direct, nonlinear inversion of the loudspeaker's dynamics are performed via a nonlinear system. The nonlinear filter is a pre-processor of the desired input signal, the output of which is connected to the loudspeaker system's input. If the loudspeaker system is perfectly known and time-invariant, the distortion reduction potential is large. This, however, is not the case in practice due to unmodeled effects such as aging and changes to the acoustic environment within which the loudspeaker is operating. Moreover, the pre-filter does not compensate for disturbances due to extraneous sounds present in the environment. Even a slight change in the system's dynamics may adversely affect the loudspeaker's performance bringing it to a level lower than that of the loudspeaker without the pre-filter. Another dynamic inversion method is studied in [36], where an adaptive linear pre-filter is used. Since the adaptive process is on-line, the pre-filter offers the advantage of adjusting the filter coefficients in response to changes in the loudspeaker system's dynamics. On the other hand, the method only deals with the linear dynamics of the loudspeaker and does not offer any rejection to exogenous disturbances.

Nonlinear Feedback Control: As outlined in [61], [52] and [34], nonlinear control schemes are proposed, where the loudspeaker cone's position is used as the feedback signal. While these methods can theoretically fully linearize the cone motion's dynamics, they rely on an exact understanding of the loudspeaker system's dynamics and a noise free measurement signal. This is not realistic due to unmodeled effects (as mentioned earlier) and noise introduced by the sensor measuring the feedback signal. Furthermore, the methods depend on the cone's position as the feedback signal, which is currently less practical than using the cone's acceleration or the loudspeaker's pressure output.

Linear Feedback Control: To reduce the control system's complexity, techniques by which the voice-coil current is fed back using a linear controller are developed in [62], [9], [30], [24], [38], [37] and [3]. Even though the techniques have the advantage of not requiring a sensor for feedback use, they have to infer the voice-coil velocity information via a linear map involving the voice-coil current. Since that map may not actually be linear (or fixed), the available distortion reduction potential of feedback control may not be fully exploited. To deal with this issue, [11], and [1] consider the use of an accelerometer (to measure the cone's acceleration) as the feedback sensor. This method has been successfully implemented in several commercial products, with significant performance improvement. However, since the ultimate goal is to improve the output pressure response of the loudspeaker, assumptions are made with regard to the map from the cone's acceleration to the pressure output. Since the pressure information is not fed back to the controller, the closed-loop system may be sensitive to changes in that map. Moreover, the feedback sensor must be physically attached to the loudspeaker's cone. Even though modern accelerometers are light and compact, the loudspeaker's moving mass is measurably increased, which can adversely affect the system's performance potential.

In Chapter 4, a feedback scheme based on modern control systems theory is applied to a loudspeaker system. The control system utilizes the pressure output of the loudspeaker system for feedback. One of the advantages of this technique over those previously attempted is that it controls more of the loudspeaker's dynamics, while simultaneously remaining simple to implement. All that is necessary is a pressure transducer and a properly designed, simple linear filter for the control method to be realized. Also, the method results in a closed-loop system that guarantees the specified performance in the face of uncertainties in the system's dynamics, offers exogenous disturbance rejection, and exhibits reduced sensitivity to sensor noise. Furthermore, its non-invasive nature allows its use as a retrofit to existing loudspeaker systems, without the added penalty of increasing their moving mass.

To demonstrate the applicability of the theory developed in this dissertation to a variety of loudspeaker systems, three examples are discussed in Chapter 5. The first uses the vented loudspeaker model developed in Chapter 2, while the other two involve actual loudspeaker systems in both vented and sealed configurations. Data from the examples are presented and the results are evaluated. Some concluding remarks and summary of the findings are given in Chapter 6.

In Appendix A, proofs for the theoretical results involving the interaction between the loudspeaker cone's motion and the acoustic environment are given. Appendix B documents a linear algebra derivation which involves converting implicit state-space equations to explicit expressions, while Appendix C shows how to perform a state-space extraction of a blocking zero. Finally, Appendix D lists some linear system matrices for the first example of Chapter 5.

Chapter 2

Loudspeaker Model

This chapter details the development of a lumped-parameter loudspeaker model. The approach taken is to capture as much of the nonlinear behavior of the loudspeaker as possible while keeping the model simple, so that it lends itself to control and parametric identification techniques currently available from the literature. Figure 2.1 shows a schematic of a voice-coil loudspeaker in a vented enclosure.

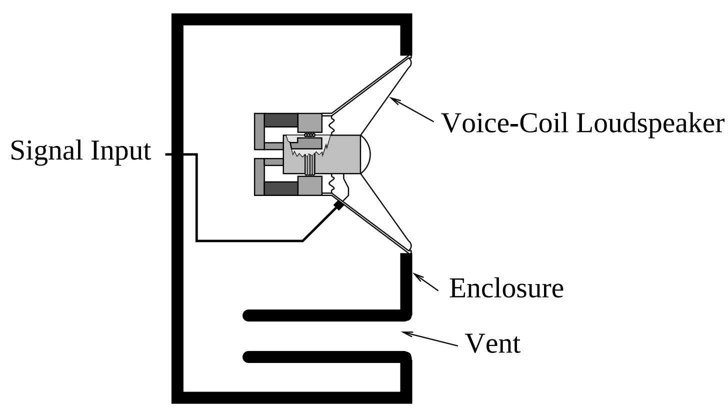

Figure 2.1: The Vented-Box Loudspeaker

The enclosed loudspeaker is modeled as a combination of the following components: A voice-coil loudspeaker, a vented enclosure, an acoustic environment, and a duct attached to the vent. These components are detailed as follows.

2.1 Voice-Coil Loudspeaker

A typical voice-coil loudspeaker is illustrated in Figure 2.2. A time varying cur-

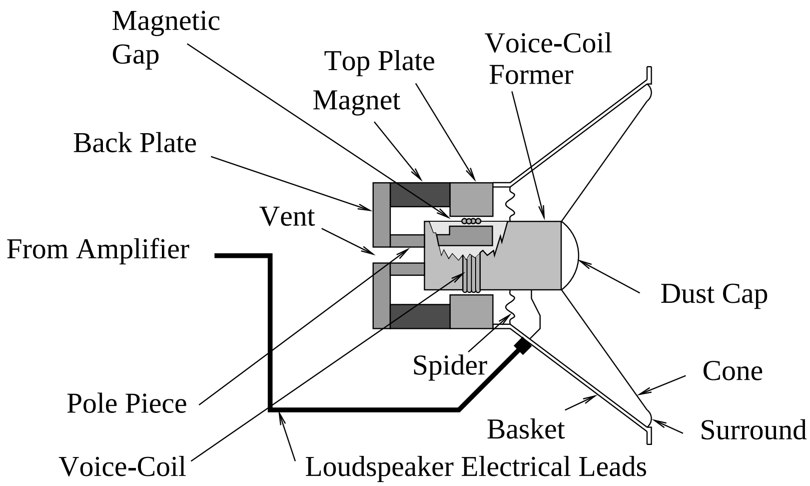

Figure 2.2: Voice-Coil Loudspeaker

rent from an amplifier drives a voice-coil motor attached to a rigid cone. The cone motion is constrained to move predominantly in the axial direction by the *spider* and *surround* (together forming the mechanical suspension), which are rigidly attached to the loudspeaker's *basket*. This attachment method also introduces mechanical stiffness and damping which forces the cone to rest in a nominal position when no current is fed into the voice-coil.

2.1.1 Free Body Analysis

A one-dimensional free body diagram of the loudspeaker is sketched in Figure 2.3. The cone is viewed as a rigid piston that is free to move axially.

A z-coordinate force balance results in the governing differential equation

$$F - F_k - F_{R_m} + F_{\mathrm{b}} - F_{\mathrm{H}} = m\ddot{z}, \tag{2.1}$$

where m is the loudspeaker's moving mass, $\ddot{z}$ is the cone's acceleration ($=: \frac{d^2z}{dt^2}$), and the forces are due to

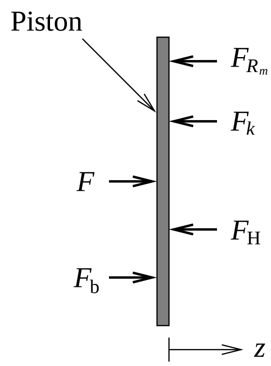

Figure 2.3: Loudspeaker Free-Body

F: voice-coil motor,

F_k, F_{R_m}: mechanical stiffness and damping introduced by the mechanical suspension, respectively, and

F_{H}, F_{b}: acoustic environments the cone faces are exposed to.

2.1.2 Voice-Coil Motor

Figure 2.4 shows the electrical circuit diagram of the voice-coil motor where u is the voltage applied across the voice-coil, and i, L_{e}, and R_{e} are the voice-coil current, inductance, and resistance, respectively [28]. The voice-coil motion generates the back-emf term ($=: Bl(z)\dot{z}$), where z, $\dot{z}$, and $Bl(z)$ are the motor's position, velocity ($=: \frac{dz}{dt}$), and force factor, respectively. The force factor is the product of the magnetic flux density ($=: B$) and the length of the voice-coil conductor immersed in the magnetic field ($=: l$).

Assuming that L_{e} and R_{e} are constant while applying Kirchhoff's voltage law to the circuit yields the governing differential equation [53]

$$L_{\mathrm{e}}\frac{di}{dt} = u - R_{\mathrm{e}}i - Bl(z)\dot{z}. \tag{2.2}$$

The force generated by the motor is proportional to the voice-coil current and is

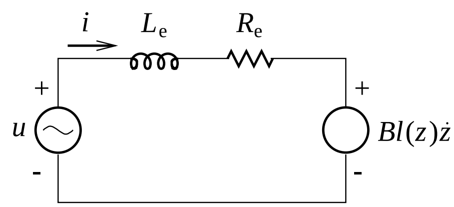

Figure 2.4: Voice-Coil Motor's Electrical Circuit

described as [28]

$$F(i, z) := Bl(z)i =: F. \tag{2.3}$$

Typically, the motor's magnetic structure produces a non-uniform magnetic field that the voice-coil moves in, such as Figure 2.5 illustrates.

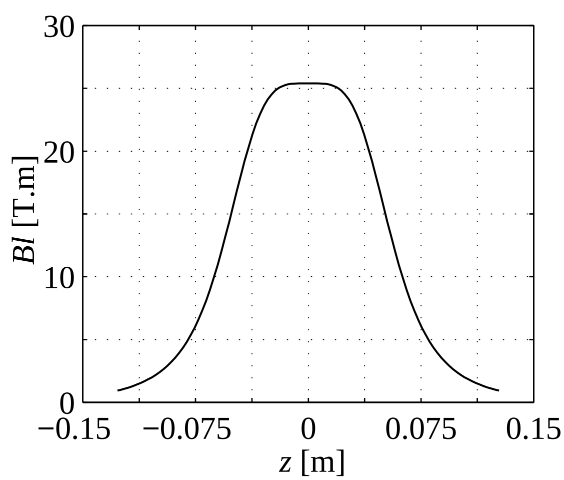

Figure 2.5: Voice-Coil Motor's Force Factor

Assuming a symmetric magnetic field, the nonlinearity can be parametrized by

$$Bl(z) := \frac{Bl_0}{1 + Bl_1 z^{\kappa}}, \tag{2.4}$$

where Bl_0 and Bl_1 are the linear and nonlinear force factors, respectively, and κ is a positive, even integer ($Bl_0 = 25.4$ T $\cdot$ m, $Bl_1 = 10^5$ m^{-4}, and $\kappa = 4$ for Figure 2.5).

2.1.3 Mechanical Suspension

The mechanical suspension comprised of the spider and surround can be modeled as a nonlinear spring and a linear damper connected in parallel. Figure 2.6 shows a a plot of force vs. displacement for a typical stiffening spring.

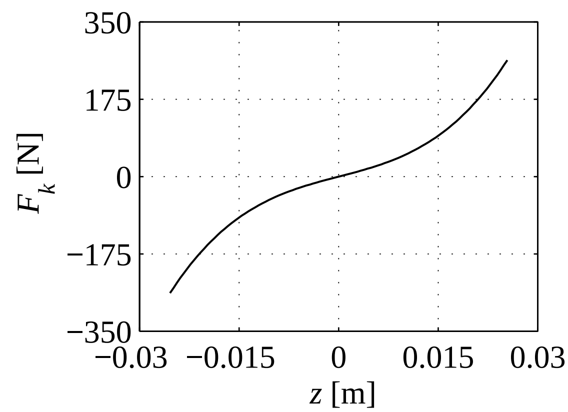

Figure 2.6: Stiffening Spring

This nonlinear map can be well described by the polynomial

$$F_k(z) := k_0 z + k_1 z^2 + k_2 z^3 =: F_k, \tag{2.5}$$

where k_0 is the linear spring constant, k_1 and k_2 are the quadratic and cubic coefficients, respectively. Note that for a symmetric curve, $k_1 := 0$ is assumed ($k_0 = 3922$ N/m, $k_1 = 0$, and $k_2 = 10^7$ N/m^3 for Figure 2.6).

Finally, the mechanical damping is modeled as

$$F_{R_m}(\dot{z}) := R_m \dot{z} =: F_{R_m}, \tag{2.6}$$

where R_m is the mechanical damping factor.

Substituting (2.3), (2.4), (2.5), and (2.6) into (2.1) and combining with (2.2) yields the nonlinear voice-coil loudspeaker equations

$$\frac{d^2 z}{dt^2} = \frac{1}{m}\left[Bl(z)i - F_k(z) - R_m \frac{dz}{dt} + F_\mathrm{b} - F_\mathrm{H}\right], \tag{2.7}$$

$$\frac{di}{dt} = \frac{1}{L_e}\left[u - R_e i - Bl(z)\frac{dz}{dt}\right]. \tag{2.8}$$

2.2 Acoustic Environment

Consider a rigid infinite baffle residing in a $\mathbb{R}^3$ half-space ($\{(x, y, z) \in \mathbb{R}^3 : z \geq 0\}$) with a prescribed normal velocity $u_z(x, y, t)$ confined to a finite region $\Omega \in \mathbb{R}^2$ on its surface ($z = 0$), as illustrated in Figure 2.7.

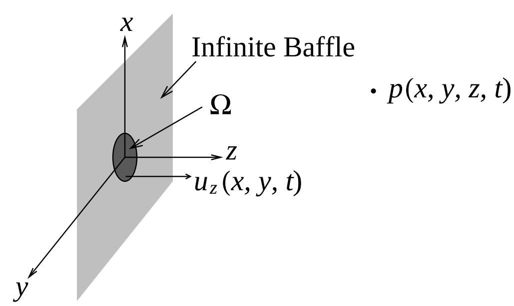

Figure 2.7: Baffled Source

The linearized wave and Euler's equations governing the pressure $p(x, y, z, t)$ in the half-space are [44], [29]

$$\Delta p = \frac{1}{c^2}\frac{\partial^2 p}{\partial t^2}, \tag{2.9}$$

$$\rho_0 \frac{\partial u}{\partial t} = -\vec{\nabla} p, \tag{2.10}$$

where $u(:= u(x, y, z, t))$, c, and ρ_0 are the particle velocity, wave speed, and equilibrium density of the medium, respectively. The boundary condition is expressed as

$$\left.\frac{\partial p}{\partial z}\right|_{z=0} = -\rho_0 \frac{\partial u_z}{\partial t}. \tag{2.11}$$

Taking the Fourier transforms of (2.9), (2.10), and (2.11) yields [42]

$$\Delta \hat{P} = -\frac{w^2}{c^2}\hat{P}, \tag{2.12}$$

$$j\omega\rho_0 \hat{U} = -\vec{\nabla}\hat{P}, \tag{2.13}$$

$$\left.\frac{\partial \hat{P}}{\partial z}\right|_{z=0} = -j\omega\rho_0 \hat{U}_z, \tag{2.14}$$

where $\hat{P}$, $\hat{U}$, and $\hat{U}_z$ are the Fourier transforms of p, u, and u_z, respectively. Equation (2.12) is referred to as the *Helmholtz Equation*.

Separating the spatial and temporal components of the source velocity yields

$$u_z(x, y, t) := l(x, y) f(t), \tag{2.15}$$

as illustrated in Figure 2.8. Taking the Fourier transform of (2.15) gives

$$\hat{U}_z(x, y, \omega) = l(x, y) \hat{f}(j\omega), \tag{2.16}$$

where $\hat{f}$ is the Fourier transform of f.

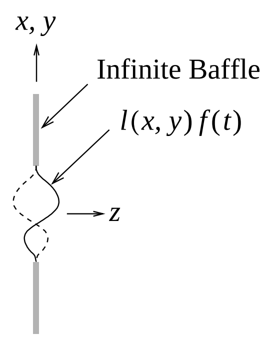

Figure 2.8: The Function $l(x, y)f(t)$

Assuming $l(x, y) \in \mathcal{C}_c(\mathbb{R}^2) \cap \mathcal{L}_\infty$, the solution which satisfies (2.12), (2.13), and (2.14) that is valid everywhere except at $(x, y, z) \equiv (0, 0, 0)$ is given by

$$\hat{P}(x, y, z) = \left[\int_{\mathbb{R}^2} \phi(x - \eta, y - \xi, z) l(\eta, \xi) \, d\eta \, d\xi \right] \hat{f}(j\omega), \tag{2.17}$$

where

$$\phi(x, y, z) := \frac{j\omega\rho_0}{2\pi} \frac{e^{-j\frac{\omega}{c}\sqrt{x^2+y^2+z^2}}}{\sqrt{x^2 + y^2 + z^2}}. \tag{2.18}$$

The proof is given in Appendix A.

Then, the integral

$$H := \int_{\Omega} \hat{P}(\eta, \xi, 0) d\eta \, d\xi \tag{2.19}$$

is the Fourier transform of the force ($:= F_{\mathrm{H}}(t)$) exerted on the source, averaged over Ω.

Fix the location $(x, y, z) := (\bar{x}, \bar{y}, \bar{z})$ and define

$$G_p(j\omega) := \hat{P}(\bar{x}, \bar{y}, \bar{z}). \tag{2.20}$$

Note that $G_p(j\omega)$ and H ($=: H(j\omega)$) relate the steady-state pressure and force responses to the source velocity, respectively, where $G_p(j\omega)$ is parametrized by the location $(\bar{x}, \bar{y}, \bar{z})$. These relations can be computed as follows.

Letting $f(t) := e^{j\omega t}$ (for a sinusoidal, steady-state source motion) the steady-state pressure can be described as

$$p(\bar{x}, \bar{y}, \bar{z}, t) = G_p e^{j\omega t}. \tag{2.21}$$

The integral in (2.17) can be approximated for a fixed $(x, y, z) := (\bar{x}, \bar{y}, \bar{z})$, pointwise in ω, by numerical methods (e.g. rectangular rule). Then, a finite-dimensional, rational, frequency domain fit (cascaded with a pure time delay) of the generated data from the integral can be obtained.

The steady-state force can be written as

$$F_{\mathrm{H}}(t) = H e^{j\omega t} \tag{2.22}$$

and the integral in (2.19) can be similarly approximated and fit with a rational system.

Since the acoustic equations support superposition, this analysis can be easily extended to include the case of multiple sources on an infinite baffle (e.g. a loudspeaker with a vent). When the assumptions are made that the loudspeaker cone and the air on the face of the vent (baffle-side) act as rigid pistons, are constrained to move axially, and are mounted on an infinite baffle in a half-space, (2.21) can be used to obtain the pressure at any point in the half-space. Also, (2.22) can be utilized to determine the forces F_{H} or F_{b} in (2.1), the equation governing the motion of the loudspeaker's cone.

As an illustration, the frequency response from the source velocity to the pressure at the location $(\bar{x}, \bar{y}, \bar{z}) = (-0.15, 0, 1)$ (in meters) was computed for an infinitely baffled, circular piston with radius $a := 0.16$ meters vibrating in air ($\rho_0 = 1.21$ kg/m^3, $c = 343$ m/s). The shape function was given as

$$l(x, y) := \begin{cases} 1 & \text{for } \sqrt{x^2 + y^2} \leq a \\ \frac{a+\epsilon-\sqrt{x^2+y^2}}{\epsilon} & \text{for } a \leq \sqrt{x^2 + y^2} \leq a + \epsilon \\ 0 & \text{elsewhere,} \end{cases} \tag{2.23}$$

where $\epsilon \in \mathbb{R}_+$ is small and nonzero. Since the data contained a pure time delay of $\frac{\bar{z}}{c} = 2.9 \times 10^{-3}$ seconds, it was removed for the purposes of performing a rational fit. Therefore, Figure 2.9 shows a 5^{th}-order, frequency-domain fit (using a least squares algorithm) that is in good agreement with the data (without the delay). Now that the fit is computed, it can be cascaded with a time delay element to obtain the map from the source velocity to $p(\bar{x}, \bar{y}, \bar{z}, t)$.

Similarly, the frequency response from the source velocity to the average force acting on the piston was computed and fit with a 6^{th}-order, rational function. Since the calculation involved the pressure on the face of the piston itself (rather than another surface), there was no time delay.

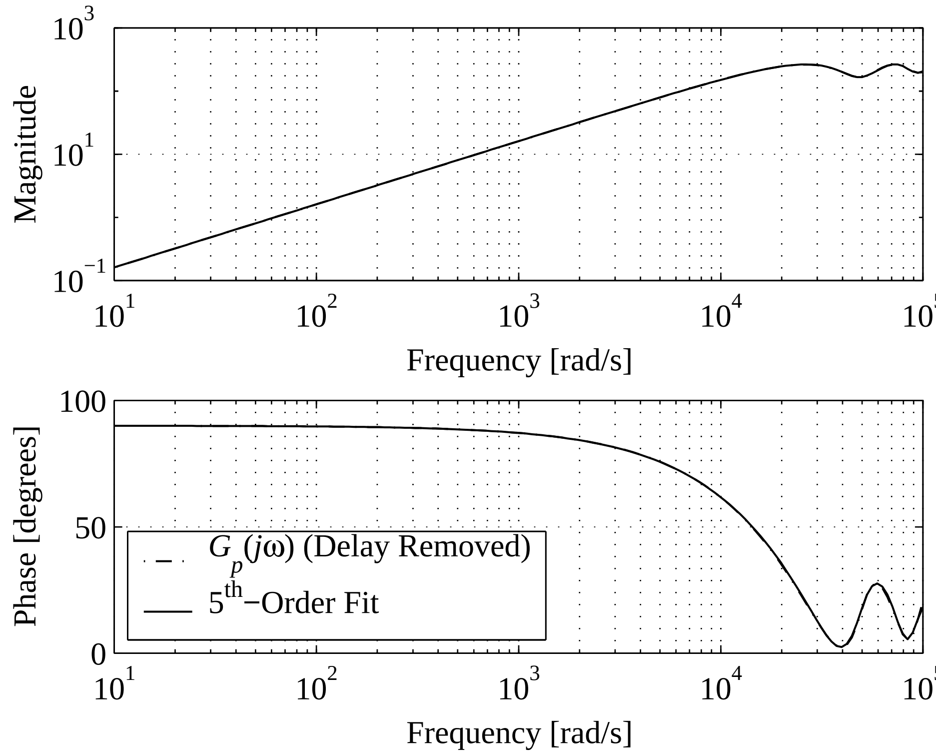

Figure 2.9: Velocity to Pressure Frequency Response at $(\bar{x}, \bar{y}, \bar{z}) = (-0.15, 0, 1)$ meters with the Delay Removed

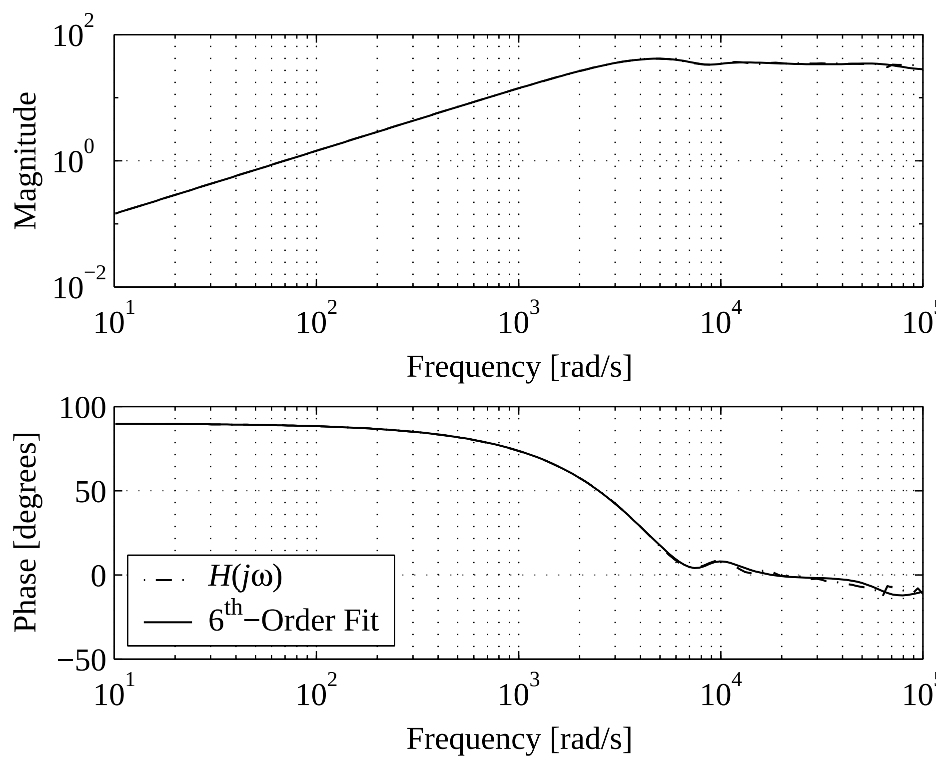

Figure 2.10: Velocity to Average Force Frequency Response

2.3 Enclosure

Figure 2.11 shows an insulated enclosure of volume V_{b}, filled with air at pressure P_{b}. The enclosure has two openings which are covered with two rigid pistons with cross sectional areas Ω_1 and Ω_2, respectively (the theory can be easily extended to an arbitrary number of openings). The pistons are allowed to freely move in the z_1 and z_2 directions, respectively, while no air is permitted to escape or enter the enclosure.

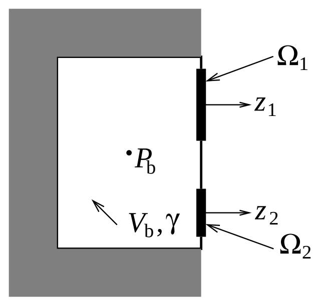

Figure 2.11: Vented Enclosure

2.3.1 Assumptions

In order to obtain a simple enclosure model, the following assumptions were made:

- Perfect gas with constant specific heats.
- Isentropic thermodynamic process (reversible and adiabatic).
- Uniform static compression within the enclosure.

Under these assumptions, the thermodynamic relationship between $P_{\mathrm{b}} := P_{\mathrm{b}}(z_1, z_2)$, and $V_{\mathrm{b}} := V_{\mathrm{b}}(z_1, z_2)$ is derived from the ideal gas law to be [47]

$$P_{\mathrm{b}}(z_1, z_2)V_{\mathrm{b}}^{\gamma}(z_1, z_2) = C, \tag{2.24}$$

where γ is the ratio of the specific heat at a constant pressure to the specific heat at a constant volume ($\gamma = 1.4$ for air) and C is a constant. Define $P_{\mathrm{b}_0} := P_{\mathrm{b}}(0, 0)$ and

$V_{b_0} := V_b(0,0)$. Then, given P_{b_0} and V_{b_0},

$$\frac{P_b(z_1,z_2)}{P_{b_0}} = \left(\frac{V_{b_0}}{V_b(z_1,z_2)}\right)^{\gamma}. \tag{2.25}$$

Let

$$p_b(z_1,z_2) := P_b(z_1,z_2) - P_{b_0}, \tag{2.26}$$

$$v_b(z_1,z_2) := V_b(z_1,z_2) - V_{b_0}. \tag{2.27}$$

Realizing that $v_b(z_1,z_2) = \Omega_1 z_1 + \Omega_2 z_2$, the final relationship reduces to

$$p_b(z_1,z_2) = P_{b_0}\left[\left(1 + \frac{\Omega_1 z_1 + \Omega_2 z_2}{V_{b_0}}\right)^{-\gamma} - 1\right]. \tag{2.28}$$

Therefore, the forces exerted on the pistons with cross sectional areas Ω_1 and Ω_2 are

$$F_{b_1}(z_1,z_2) := p_b(z_1,z_2)\Omega_1, \tag{2.29}$$

$$F_{b_2}(z_1,z_2) := p_b(z_1,z_2)\Omega_2, \tag{2.30}$$

respectively.

2.3.2 Issues Relating to Loudspeakers

The following issues are observed when dealing with enclosed loudspeakers:

- Given that $|p_b|$ is never more that 10^4 Pa and the temperatures are not extremely low (e.g. near 0 K), the ideal gas law holds for air.
- If the process is not perfectly adiabatic (e.g. due to poorly insulated enclosure walls, etc.), γ has to be experimentally determined.
- Equation (2.24) is not valid if the thermodynamic process is not reversible:
  - Irreversible processes produce entropy (:= total molecular "disorganization" within the system).

  - Examples of irreversible processes: Unrestrained expansion (leaks through the enclosure's walls, flexure of the piston and the enclosure's walls that have not been taken into account) and energy transfer due to large temperature non-uniformities (i.e. large temperature gradients in the enclosed air).

- Since this is a static model, it is not valid at high frequencies ($>$ 170 Hz for a typical, $0.5 \times 0.5 \times 0.5$ m^3 enclosure with $c = 343$ m/s). The development of standing waves in the enclosure cause the pressure to be nonuniform across the box.

With the assumptions and issues in mind, (2.29) and (2.30) can be incorporated in (2.1), the loudspeaker cone's equation of motion.

2.4 Duct Model

Consider a one-dimensional duct of length L with cross sectional area Ω_{d}. The governing linearized acoustic equations are given by [44], [29]

$$\frac{\partial^2 p(\xi,t)}{\partial \xi^2} = \frac{1}{c^2}\frac{\partial^2 p(\xi,t)}{\partial t^2}, \tag{2.31}$$

$$\rho_0 \frac{\partial u(\xi,t)}{\partial t} = -\frac{\partial p(\xi,t)}{\partial \xi}, \tag{2.32}$$

where $p(\xi,t)$ is the pressure inside the duct as a function of space ξ and time t, $u(\xi,t)$ is the particle velocity, and c and ρ_0 are the speed of sound in air and corresponding density at equilibrium, respectively. The values for $p(0,t)$, $p(L,t)$, $\frac{\partial u(0,t)}{\partial t} =: \ddot{z}(0,t)$, $\frac{\partial u(L,t)}{\partial t} =: \ddot{z}(L,t)$ are given as boundary conditions, where $\ddot{z}(0,t)$ and $\ddot{z}(L,t)$ are the particle accelerations at $\xi = 0$ and $\xi = L$, respectively.

To solve this problem, a finite difference approximation for (2.31) and (2.32) is proposed [35]. Figure 2.12 shows the duct divided into N+1 sections, each with width $h := \frac{L}{N+1}$.

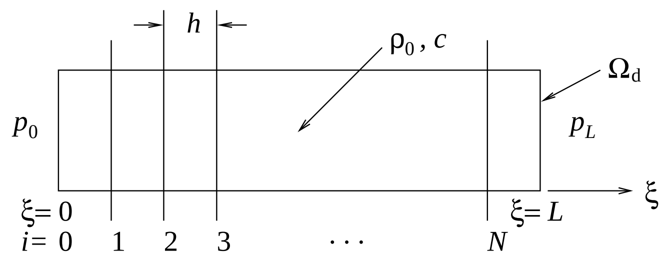

Figure 2.12: One-Dimensional Duct

Approximating (2.31) yields

$$\frac{p_{i+1}(t) - 2p_i(t) + p_{i-1}(t)}{h^2} = \frac{1}{c^2}\ddot{p}_i(t), \; i = 1, 2, \ldots, N+1, \tag{2.33}$$

where $p_i(t)$ is the pressure at the i-th face in the duct and $\ddot{p}_i(t) := \frac{\partial^2 p(ih,t)}{\partial t^2}$. Note that $p_{N+1}(t) = p_L(t)$. Equation (2.32), which furnishes the boundary condition relationships, yields the approximations

$$\frac{-p_1(t) + p_0(t)}{\rho_0 h} = \ddot{z}(0,t) =: \ddot{z}_0(t), \tag{2.34}$$

$$\frac{-p_L(t) + p_N(t)}{\rho_0 h} = \ddot{z}(L,t) =: \ddot{z}_L(t). \tag{2.35}$$

Letting $\eta := \begin{bmatrix} p \\ \dot{p} \end{bmatrix}$, the foregoing equations can be expressed implicitly as

$$\begin{bmatrix} \dot{\eta} \\ 0_2 \end{bmatrix} := \begin{bmatrix} \hat{A} & \hat{B}_1 & \hat{B}_2 & \hat{B}_3 & \hat{B}_4 \\ \hat{C} & \hat{D}_1 & \hat{D}_2 & \hat{D}_3 & \hat{D}_4 \end{bmatrix} \begin{bmatrix} \eta \\ p_0 \\ p_L \\ \ddot{z}_0 \\ \ddot{z}_L \end{bmatrix} \tag{2.36}$$

where

$$\hat{A} := \left[\begin{array}{c|c} 0_{N\times N} & \left(\frac{c}{h}\right) I_N \\ \hline \left(\frac{c}{h}\right)\begin{bmatrix} -2 & 1 & 0 & \cdots & & & 0 \\ 1 & -2 & 1 & 0 & \cdots & & 0 \\ 0 & 1 & -2 & 1 & 0 & \cdots & 0 \\ & \ddots & \ddots & \ddots & \ddots & \ddots & \\ 0 & 0 & \cdots & & & 1 & -2 \end{bmatrix}_{N\times N} & 0_{N\times N} \end{array}\right], \tag{2.37}$$

$$\hat{B}_1 := \left[\begin{array}{c} 0_N \\ \hline \begin{bmatrix} \left(\frac{c}{h}\right) \\ 0_{(N-1)} \end{bmatrix} \end{array}\right], \ \hat{B}_2 := \left[\begin{array}{c} 0_N \\ \hline \begin{bmatrix} 0_{(N-1)} \\ \left(\frac{c}{h}\right) \end{bmatrix} \end{array}\right], \tag{2.38}$$

$$\hat{B}_3 := 0_{2N} =: \hat{B}_4, \tag{2.39}$$

$$\hat{C} := \begin{bmatrix} -\left(\frac{1}{\rho_0 h}\right) & 0 & & \cdots & & & 0 \\ 0 & & \cdots & \left(\frac{1}{\rho_0 h}\right)_{(N^{\text{th}} \text{ location})} & 0 & \cdots & 0 \end{bmatrix}_{2\times 2N}, \tag{2.40}$$

$$\hat{D}_1 := \begin{bmatrix} \left(\frac{1}{\rho_0 h}\right) \\ 0 \end{bmatrix}, \ \hat{D}_2 := \begin{bmatrix} 0 \\ -\left(\frac{1}{\rho_0 h}\right) \end{bmatrix}, \tag{2.41}$$

$$\hat{D}_3 := \begin{bmatrix} -1 \\ 0 \end{bmatrix}, \ \hat{D}_4 := \begin{bmatrix} 0 \\ -1 \end{bmatrix}. \tag{2.42}$$

Note that the row and column separation lines were added for clarity. Define the pressures and accelerations at the ends of the duct as the inputs and outputs, respectively. Since $\begin{bmatrix} \hat{D}_3 & \hat{D}_4 \end{bmatrix}$ is invertible, the $2N^{\text{th}}$-order equations can be written explicitly as

$$\begin{bmatrix} \dot{\eta} \\ \ddot{z}_0 \\ \ddot{z}_L \end{bmatrix} = \begin{bmatrix} A_{\text{duct}} & B_{\text{duct}} \\ C_{\text{duct}} & D_{\text{duct}} \end{bmatrix} \begin{bmatrix} \eta \\ p_0 \\ p_L \end{bmatrix}, \tag{2.43}$$

where

$$A_{\text{duct}} := \hat{A}, \tag{2.44}$$

$$B_{\mathrm{duct}} := \begin{bmatrix} \hat{B}_1 & \hat{B}_2 \end{bmatrix}, \tag{2.45}$$

$$C_{\mathrm{duct}} := -\begin{bmatrix} \hat{D}_3 & \hat{D}_4 \end{bmatrix}^{-1} \hat{C}, \tag{2.46}$$

$$D_{\mathrm{duct}} := \begin{bmatrix} \hat{D}_3 & \hat{D}_4 \end{bmatrix}^{-1} \begin{bmatrix} \hat{D}_1 & \hat{D}_2 \end{bmatrix}. \tag{2.47}$$

The details of converting the equations from implicit to explicit expressions can be found in Appendix B.

Chapter 3

Nonlinear Distortion Measures

To quantify the loudspeaker's nonlinear behavior, some measures of the nonlinear distortion must be defined. Recent findings in low-frequency psychoacoustics indicate that the most significant (and likely to be heard) type of distortion is harmonic, with the odd-order harmonics being the most bothersome. Hence, harmonic distortion performance has been found to be a suitable measure in determining a loudspeaker's linearity when operating in the low-frequency region [19]. One attractive property of using the harmonic distortion as a measure of the nonlinearity is its ability to capture in a single number the level of distortion from the complex harmonic spectrum produced by the output of a nonlinear system. In this chapter, several measures are proposed and their properties analyzed with suitable examples.

3.1 Fourier Theory Preliminaries

Given a real, periodic function $y(t)$ defined on $t \in [0, T] \subset \mathbb{R}_+$, its Fourier series can be described as [50]

$$y(t) := a_0 + \sum_{n=1}^{\infty} a_n \cos \frac{2\pi}{T} nt + \sum_{n=1}^{\infty} b_n \sin \frac{2\pi}{T} nt, \tag{3.1}$$

where the coefficients $\{a_n\}_{n=0}^{\infty}$ and $\{b_n\}_{n=1}^{\infty}$ are called the *Fourier coefficients* of y. These can be computed as

$$\begin{aligned} a_0 &= \frac{1}{T}\int_0^T y(t)\ dt, \\ a_n &= \frac{2}{T}\int_0^T y(t)\cos\frac{2\pi}{T}nt\ dt, \\ b_n &= \frac{2}{T}\int_0^T y(t)\sin\frac{2\pi}{T}nt\ dt,\ \ n>0. \end{aligned} \tag{3.2}$$

Note that $\left\{\frac{2\pi}{T}n\right\}_{n=1}^{\infty}$ and $\left\{a_n\cos\frac{2\pi}{T}nt + b_n\sin\frac{2\pi}{T}nt\right\}_{n=1}^{\infty}$ are referred to as the *harmonic frequencies* and *harmonic components* in y, respectively. Also, $\left(\frac{2\pi}{T}\right)$ is called the *fundamental frequency* and $\left(a_1\cos\frac{2\pi}{T}t + b_1\sin\frac{2\pi}{T}t\right)$ the *fundamental component* or *first harmonic* in y.

3.2 Harmonic Distortion: Definition

Figure 3.1 shows a causal nonlinear system f that maps u into y with the property that for bounded sinusoidal inputs, f produces bounded periodic outputs, in the steady state [51].

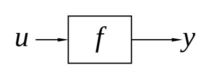

Figure 3.1: Nonlinear System

Let

$$u(t) := \bar{u}\sin\omega t \tag{3.3}$$

and assume the steady-state output to be periodic with period $T := \frac{2\pi}{\omega}$. Therefore, the Fourier decomposition of the output signal y is given in (3.1) and (3.2).

Let

$$\Upsilon(y) := \sqrt{|a_1|^2 + |b_1|^2}, \tag{3.4}$$

i.e. Υ is the amplitude of the fundamental component in y. The following measures of the harmonic distortion in y are considered. Define

$$\mathrm{THD}\left(\Upsilon,\omega\right) := \sqrt{\frac{\sum_{n=2}^{\infty}\left(\left|a_n\right|^2+\left|b_n\right|^2\right)}{\sum_{n=1}^{\infty}\left(\left|a_n\right|^2+\left|b_n\right|^2\right)}}. \tag{3.5}$$

Furthermore, a slightly modified version of THD that has some desirable properties (to be shown later) is proposed as

$$\mathrm{THD_A}\left(\Upsilon,\omega\right) := \sqrt{\frac{\sum_{n=2}^{\infty}\left(\left|a_n\right|^2+\left|b_n\right|^2\right)}{\left|a_1\right|^2+\left|b_1\right|^2}}. \tag{3.6}$$

Also, a simple measure that relates the amplitude of the k^{th} harmonic component to that of the fundamental component is given by

$$\mathrm{HD_k}\left(\Upsilon,\omega\right) := \sqrt{\frac{\left|a_k\right|^2+\left|b_k\right|^2}{\left|a_1\right|^2+\left|b_1\right|^2}}. \tag{3.7}$$

For instance, suppose the input-output relation of a static map is

$$y := \Psi_1(u) := \begin{cases} 1 & \text{if } u > 0 \\ -1 & \text{if } u < 0. \end{cases} \tag{3.8}$$

Then, if $u(t) = \bar{u}\sin\omega t$, $y(t) := \Psi_1(u(t))$ will be a square wave with unit amplitude, and frequency ω.

A square wave is periodic, and thus a Fourier series can be computed with

$$a_0 = 0,\ a_1 = 0, \ldots,\ a_n = 0, \ldots \tag{3.9}$$

$$b_1 = \frac{4}{\pi},\ b_2 = 0,\ b_3 = \frac{4}{3\pi},\ b_4 = 0,\ b_5 = \frac{4}{5\pi},\ b_6 = 0, \ldots \tag{3.10}$$

Therefore, $\Upsilon = b_1$ and $\mathrm{THD}\left(\Upsilon,\omega\right) \approx 0.435$, i.e. the map Ψ_1 produces about 43.5% harmonic distortion. In this case, the THD and the fundamental component's amplitude values don't change regardless of the input signal. Hence, the "graph" of THD is a single point.

To illustrate how THD and $\mathrm{THD_A}$ change as functions of Υ, consider the following examples.

Figure 3.2 illustrates a static, piecewise linear function described by

$$y := \Psi_2(u) := \begin{cases} 1 + \frac{1}{2}(u-1) & \text{if } u > 1 \\ u & \text{if } -1 \leq u \leq 1 \\ -1 + \frac{3}{2}(u+1) & \text{if } u < 1. \end{cases} \tag{3.11}$$

Using (3.5) and (3.6), Figure 3.3 shows both nonlinear measures as functions of Υ.

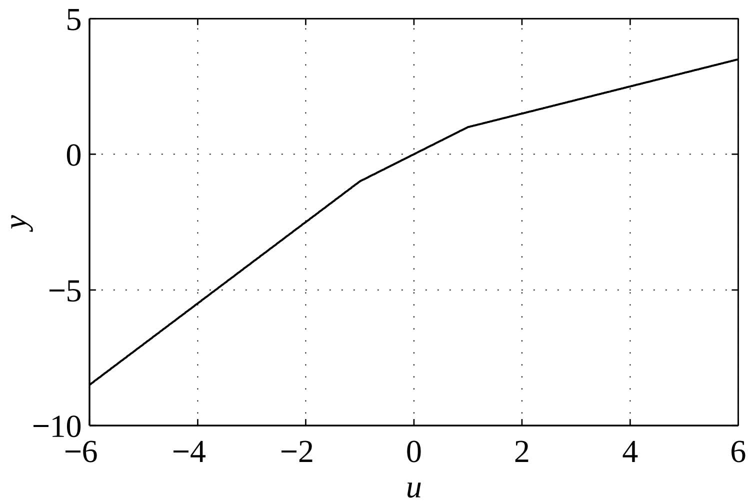

Figure 3.2: Static, Piecewise Linear Function

Similarly, Figures 3.4 shows a nonlinear function described by

$$y := \Psi_3(u) := u + \epsilon u^3, \tag{3.12}$$

where $\epsilon = 1.66 \times 10^{-4}$ for this example. The distortion characteristics for this cubic polynomial are illustrated in Figure 3.5.

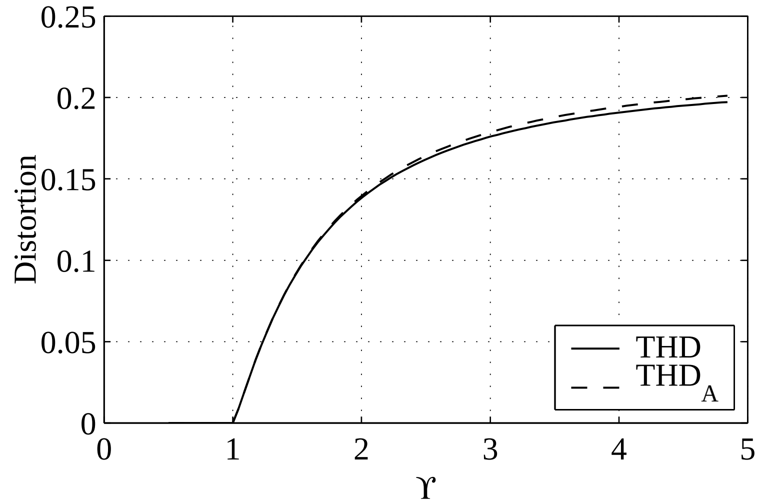

Figure 3.3: Two Measures of Harmonic Distortion for the Piecewise Linear Function

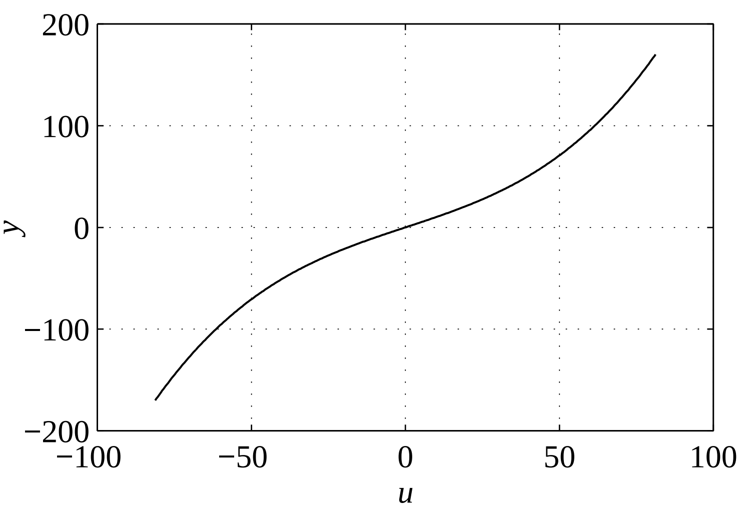

Figure 3.4: Cubic Polynomial

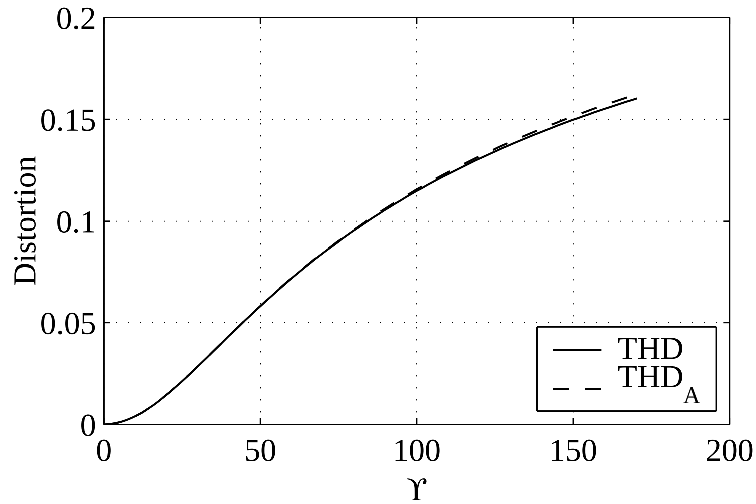

Figure 3.5: Two Measures of Harmonic Distortion for the Cubic Polynomial

3.3 Harmonic Distortion: Properties

One of the attractive features of the measure defined in (3.5) is that it describes the percentage of "energy" in the output signal that is not at the input sinusoidal frequency, ω. It is also a nonlinearity measure widely adopted by the audio industry. On the other hand, the measure described in (3.6) will be used when investigating the effects of feedback on the nonlinear distortion (Section 3.4). By investigating (3.5) and (3.6) and Figures 3.3 and 3.5, it is evident that both measures agree well when the distortion is small, with $\mathrm{THD_A}$ being the larger of the two. Another observation is that THD has a limit approaching unity (which can be interpreted as that the "energy" in y resides entirely outside the fundamental frequency), whereas $\mathrm{THD_A}$ does not. Moreover, both measures yield zero distortion when the output signal's spectrum contains only the frequency of the input sinusoid, indicating that the system producing the output is linear.

In addition, (3.7) is useful when assessing the audibility of harmonic distortion for humans, when sine-wave inputs are used to drive nonlinear acoustic sources. Even though two signals may have the same THD (or $\mathrm{THD_A}$), the audibility of the distortion may be different. This is partly due to the fact that humans' perception of a periodic, acoustic signal is a function of the period and the amplitudes of the harmonic components. As a matter of fact, studies have shown that if

$$\begin{aligned}
\mathrm{HD_2}\left(\Upsilon,\omega\right)\Big|_{\substack{\Upsilon\in[0.2,6.5]\ \mathrm{Pa},\\ \omega\in[20\pi,200\pi]\ \mathrm{rad/sec}}} &\leq 0.03,\\
\mathrm{HD_3}\left(\Upsilon,\omega\right)\Big|_{\substack{\Upsilon\in[0.2,6.5]\ \mathrm{Pa},\\ \omega\in[20\pi,200\pi]\ \mathrm{rad/sec}}} &\leq 0.01,\\
\mathrm{HD_k}\left(\Upsilon,\omega\right)\Big|_{\substack{\Upsilon\in[0.2,6.5]\ \mathrm{Pa},\\ \omega\in[20\pi,200\pi]\ \mathrm{rad/sec}}} &\leq 0.003,\ \ k\geq 4,
\end{aligned} \tag{3.13}$$

then the distortion in y is inaudible [19]. Therefore, this guideline is suitable in determining the nonlinear performance of a loudspeaker and suggests that it is sufficient to linearize a loudspeaker system up to the point where this guideline is met. Beyond this point, the difference in linearity between this system and another, more linear one is difficult to perceive by humans. The $\mathrm{HD_k}$ measure is the subject of ongoing research and will not be addressed further here.

Consider the static nonlinearity shown in Figure 3.6, where $u(t) := \bar{u} \sin \omega t$.

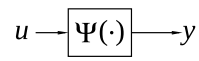

Figure 3.6: Static Nonlinearity

The distortion for this system can be easily computed using (3.5) and (3.6). The effect on the distortion measures of introducing a stable linear system in an interconnection with the nonlinearity will be studied using the following examples.

First, augment a Linear, Time Invariant (LTI) system L to the input side of the nonlinearity, as shown in Figure 3.7, where $u_1 := A_1 u(t)$, for some constant A_1. Therefore, $y_1 = \Psi(v_1) = \Psi(Lu_1) =: f_1(u_1)$. Let Υ and Υ_1 be defined as the steady-

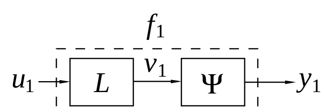

Figure 3.7: Static Nonlinearity with a LTI System Augmented to its Input

state amplitudes of the fundamental components in y (for the system in Figure 3.6) and y_1, respectively. Choose A_1 so that $\Upsilon_1 = \Upsilon$, i.e. $A_1 := \frac{1}{|L(j\omega)|}$. This can be seen by observing that in the steady state, $v_1(t)$ is a sinusoid with amplitude $|L(j\omega)|\,|A_1\bar{u}| = |\bar{u}|$ and frequency w. Let $\{a_{1_n}\}_{n=0}^{\infty}$ and $\{b_{1_n}\}_{n=1}^{\infty}$ be the Fourier coefficients of the steady state of y_1. For this case, $\Upsilon_1 := \sqrt{|a_{1_1}|^2 + |b_{1_1}|^2} = \sqrt{|a_1|^2 + |b_1|^2} = \Upsilon$. This constraint is necessary in order to properly compare the distortions of both systems. Since Ψ is static, its distortion depends only on the amplitude of $v_1(t)$. Equations (3.5) and (3.6) yield

$$\mathrm{THD}_1(\Upsilon_1, \omega) \; := \; \sqrt{\frac{\sum_{n=2}^{\infty}\left(|a_{1_n}|^2 + |b_{1_n}|^2\right)}{\sum_{n=1}^{\infty}\left(|a_{1_n}|^2 + |b_{1_n}|^2\right)}}$$

$$= \sqrt{\frac{\sum_{n=2}^{\infty}\left(|a_n|^2+|b_n|^2\right)}{\sum_{n=1}^{\infty}\left(|a_n|^2+|b_n|^2\right)}} = \mathrm{THD}\left(\Upsilon,\omega\right) \tag{3.14}$$

and

$$\begin{aligned} \mathrm{THD_{A_1}}\left(\Upsilon_1,\omega\right) &:= \sqrt{\frac{\sum_{n=2}^{\infty}\left(|a_{1_n}|^2+|b_{1_n}|^2\right)}{|a_{1_1}|^2+|b_{1_1}|^2}} \\ &= \sqrt{\frac{\sum_{n=2}^{\infty}\left(|a_n|^2+|b_n|^2\right)}{|a_1|^2+|b_1|^2}} = \mathrm{THD_A}\left(\Upsilon,\omega\right), \end{aligned} \tag{3.15}$$

respectively. Therefore, both THD and $\mathrm{THD_A}$ are invariant to augmenting a linear system to the input of a static nonlinearity.

Next, Figure 3.8 shows another interconnection where L is instead augmented to the output of Ψ.

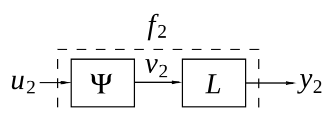

Figure 3.8: Static Nonlinearity with a LTI System Augmented to its Output

In this case, $y_2 = Lv_2 = L\Psi(u_2) =: f_2(u_2)$. Define $\{a_{2_n}\}_{n=0}^{\infty}$ and $\{b_{2_n}\}_{n=1}^{\infty}$ to be the Fourier coefficients of the steady state of y_2. Let $u_2 := A_2 u(t)$, where $u(t) := \bar{u}\sin\omega t$ and A_2 is a constant chosen so that $\Upsilon_2 := \sqrt{|a_{2_1}|^2+|b_{2_1}|^2} = \Upsilon$. Furthermore, define $\{\tilde{a}_{2_n}\}_{n=0}^{\infty}$ and $\left\{\tilde{b}_{2_n}\right\}_{n=1}^{\infty}$ to be the Fourier coefficients of v_2. Now,

$$\begin{aligned} \mathrm{THD_2}\left(\Upsilon_2,\omega\right) &:= \sqrt{\frac{\sum_{n=2}^{\infty}\left(|a_{2_n}|^2+|b_{2_n}|^2\right)}{\sum_{n=1}^{\infty}\left(|a_{2_n}|^2+|b_{2_n}|^2\right)}} \\ &= \sqrt{\frac{\sum_{n=2}^{\infty}|L(j\omega n)|^2\left(|\tilde{a}_{2_n}|^2+\left|\tilde{b}_{2_n}\right|^2\right)}{\sum_{n=1}^{\infty}|L(j\omega n)|^2\left(|\tilde{a}_{2_n}|^2+\left|\tilde{b}_{2_n}\right|^2\right)}} \\ &= \sqrt{\frac{\sum_{n=2}^{\infty}|L(j\omega n)|^2\left(|\tilde{a}_{2_n}|^2+\left|\tilde{b}_{2_n}\right|^2\right)}{|a_1|^2+|b_1|^2+\sum_{n=2}^{\infty}|L(j\omega n)|^2\left(|\tilde{a}_{2_n}|^2+\left|\tilde{b}_{2_n}\right|^2\right)}} \end{aligned}$$

$$\neq \sqrt{\frac{\sum_{n=2}^{\infty}\left(|a_n|^2+|b_n|^2\right)}{\sum_{n=1}^{\infty}\left(|a_n|^2+|b_n|^2\right)}} = \mathrm{THD}\left(\Upsilon,\omega\right) \tag{3.16}$$

and

$$\begin{aligned}
\mathrm{THD}_{\mathrm{A}_2}\left(\Upsilon_2,\omega\right) &:= \sqrt{\frac{\sum_{n=2}^{\infty}\left(|a_{2_n}|^2+|b_{2_n}|^2\right)}{|a_{2_1}|^2+|b_{2_1}|^2}} \\
&= \sqrt{\frac{\sum_{n=2}^{\infty}|L(j\omega n)|^2\left(|\tilde{a}_{2_n}|^2+\left|\tilde{b}_{2_n}\right|^2\right)}{|a_1|^2+|b_1|^2}} \\
&\neq \sqrt{\frac{\sum_{n=2}^{\infty}\left(|a_n|^2+|b_n|^2\right)}{|a_1|^2+|b_1|^2}} = \mathrm{THD}_{\mathrm{A}}\left(\Upsilon,\omega\right). \qquad (3.17)
\end{aligned}$$

Therefore, the measures are not invariant to augmenting a linear system to the output of a static nonlinearity.

Finally, consider the interconnection illustrated in Figure 3.9 where the output of Ψ is summed with the output of L, while both are driven with u_3.

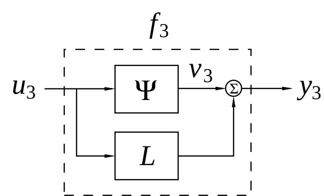

Figure 3.9: Static Nonlinearity Summed with a LTI System

For this case, $y_3 = \Psi(u_3) + Lu_3 =: f_3(u_3)$. The Fourier coefficients of the steady state of y_3 can be computed and are defined to be $\{a_{3_n}\}_{n=0}^{\infty}$ and $\{b_{3_n}\}_{n=1}^{\infty}$. Let $u_3 := A_3u(t)$, where $u(t) := \bar{u}\sin\omega t$ and A_3 is a properly picked constant so that $\Upsilon_3 := \sqrt{|a_{3_1}|^2+|b_{3_1}|^2} = \Upsilon$. Let $\{\tilde{a}_{3_n}\}_{n=0}^{\infty}$ and $\left\{\tilde{b}_{3_n}\right\}_{n=1}^{\infty}$ be the Fourier coefficients of v_3. This gives

$$\mathrm{THD}_3\left(\Upsilon_3,\omega\right) := \sqrt{\frac{\sum_{n=2}^{\infty}\left(|a_{3_n}|^2+|b_{3_n}|^2\right)}{\sum_{n=1}^{\infty}\left(|a_{3_n}|^2+|b_{3_n}|^2\right)}}$$

$$
\begin{aligned}
&= \sqrt{\frac{\sum_{n=2}^{\infty}\left(\left|\tilde{a}_{3_n}\right|^2+\left|\tilde{b}_{3_n}\right|^2\right)}{\left|a_1\right|^2+\left|b_1\right|^2+\sum_{n=2}^{\infty}\left(\left|\tilde{a}_{3_n}\right|^2+\left|\tilde{b}_{3_n}\right|^2\right)}} \\
&\neq \sqrt{\frac{\sum_{n=2}^{\infty}\left(\left|a_n\right|^2+\left|b_n\right|^2\right)}{\sum_{n=1}^{\infty}\left(\left|a_n\right|^2+\left|b_n\right|^2\right)}} = \mathrm{THD}\left(\Upsilon,\omega\right). \qquad (3.18)
\end{aligned}
$$

and

$$
\begin{aligned}
\mathrm{THD}_{\mathrm{A}_3}\left(\Upsilon_3,\omega\right) &:= \sqrt{\frac{\sum_{n=2}^{\infty}\left(\left|a_{3_n}\right|^2+\left|b_{3_n}\right|^2\right)}{\left|a_{3_1}\right|^2+\left|b_{3_1}\right|^2}} \\
&= \sqrt{\frac{\sum_{n=2}^{\infty}\left(\left|\tilde{a}_{3_n}\right|^2+\left|\tilde{b}_{3_n}\right|^2\right)}{\left|a_1\right|^2+\left|b_1\right|^2}} \\
&\neq \sqrt{\frac{\sum_{n=2}^{\infty}\left(\left|a_n\right|^2+\left|b_n\right|^2\right)}{\left|a_1\right|^2+\left|b_1\right|^2}} = \mathrm{THD}_{\mathrm{A}}\left(\Upsilon,\omega\right). \qquad (3.19)
\end{aligned}
$$

Note that $\Upsilon_3 = \sqrt{\left|L(j\omega)\right|^2\left|A_3\bar{u}\right|^2+\left|\tilde{a}_{3_1}\right|^2+\left|\tilde{b}_{3_1}\right|^2}$. As the equations illustrate, THD and $\mathrm{THD}_{\mathrm{A}}$ are not invariant to summing the output of L to the output of Ψ, when both are driven by the same input.

As can be seen by the previous 3 cases, even though the only nonlinear element in the interconnections f_1, f_2, and f_3 was always Ψ, the distortions were not necessarily the same as those for the map $y = \Psi(u)$.

3.4 Harmonic Distortion: Effect of Feedback

3.4.1 Static Feedback

Consider the feedback interconnection with a nonlinear function Ψ and constant gain K, as shown in Figure 3.10.

Note that y_c is a function of r, and it is implicitly given by the equation

$$
y_c = \Psi\left(K \cdot r - K \cdot y_c\right). \qquad (3.20)
$$

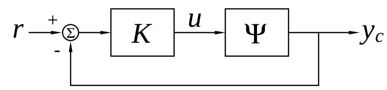

Figure 3.10: Static Nonlinearity in Constant Gain Feedback

More precisely, for a given r, $y_c(r)$ is the number that solves the equation

$$y_c(r) = \Psi\left(K \cdot r - K \cdot y_c(r)\right). \tag{3.21}$$

It is useful to study how "linear" the relationship $y_c(r)$ is. This is done by differentiating y_c with respect to r ($=:\frac{dy_c}{dr}$) and observing how "constant" that is.

Using the chain rule, (3.21) is differentiated on both sides (with respect to r) to get

$$\frac{dy_c}{dr} = \Psi'(u)\big|_{u=Kr-Ky_c(r)}\left[K - K\frac{dy_c}{dr}\right], \tag{3.22}$$

where $\Psi'(u)\big|_{u=Kr-Ky_c(r)}$ is the derivative of Ψ evaluated at $u = Kr - Ky_c(r)$. Solving for $\frac{dy_c}{dr}$ gives

$$\frac{dy_c}{dr} = \frac{\Psi' K}{1 + \Psi' K}, \tag{3.23}$$

which is the *complementary sensitivity* function.

So, if $\Psi' K$ is large, then $\frac{dy_c}{dr}$ is "more constant" than Ψ'. In other words, $y_c(r)$ is more linear than $\Psi(u)$. This is the basic reason that feedback can reduce the nonlinear distortion of a component, i.e. it has a *linearizing effect*.

3.4.2 Dynamic Feedback

The analysis in this section is based on the treatment given in [27], with some modifications. Let the static nonlinearity in Figure 3.6 be given by

$$\Psi(u) := u + \epsilon\tilde{\Psi}(u), \tag{3.24}$$

where $\epsilon \in \mathbb{R}$ is small and $\tilde{\Psi}(u)$ is a nonlinear function satisfying

$$\int_0^{2\pi} \tilde{\Psi}(\sin(x))\sin(x)\ dx = 0. \tag{3.25}$$

Consider the closed-loop system in Figure 3.11, where C is a LTI system. Assume that C is such that the closed-loop system produces bounded y_c for bounded r.

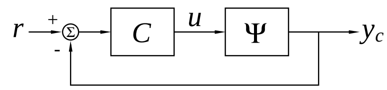

Figure 3.11: Static Nonlinearity in Dynamic Feedback

The loop equation is implicit in y_c where

$$\begin{aligned} y_c(r) &= \Psi\left(C \cdot r - C \cdot y_c(r)\right) \\ &= C \cdot r - C \cdot y_c(r) + \epsilon\tilde{\Psi}(C \cdot r - C \cdot y_c(r)) \\ &= \frac{C}{1+C} r + \frac{1}{1+C}\epsilon\tilde{\Psi}(C \cdot r - C \cdot y_c(r)). \end{aligned} \tag{3.26}$$

Note that (3.26) is implicit in ϵ, as well. One way to obtain an explicit approximation is to perform a *Taylor series* expansion on y_c as a function of ϵ about $\epsilon = 0$ [27]. Considering only terms up to first-order (in ϵ) yields

$$y_c(r) \approx \frac{C}{1+C} r + \frac{1}{1+C}\epsilon\tilde{\Psi}(\frac{C}{1+C} r) =: y_c^{(1)}(r). \tag{3.27}$$

Setting $\epsilon = 0$ in (3.27) gives

$$y_c^{(1)}(r)\Big|_{\epsilon=0} = \frac{C}{1+C} r =: \bar{y}_c(r). \tag{3.28}$$

Similarly, Figure 3.12 shows a system where $T := \frac{C}{1+C}$.

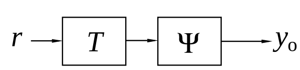

Figure 3.12: Pre-Filtered Static Nonlinearity

So,

$$\begin{aligned} y_o(r) = \Psi(Tr) &= Tr + \epsilon\tilde{\Psi}(Tr) \\ &= \frac{C}{1+C} r + \epsilon\tilde{\Psi}(\frac{C}{1+C} r). \end{aligned} \tag{3.29}$$

Setting $\epsilon = 0$ yields

$$y_o(r)|_{\epsilon=0} = \frac{C}{1+C} r =: \bar{y}_o(r). \tag{3.30}$$

Given $r := \bar{r}\sin(\frac{2\pi}{T})$, examining (3.27) and (3.29), and realizing that $\tilde{\Psi}$ is static reveals that $y_c^{(1)}$ and y_o are periodic with period T, in the steady state. Their Fourier decompositions can be computed using (3.1) and (3.2) to be

$$\begin{aligned} y_c^{(1)}(t) &:= a_{c_0} + \sum_{n=1}^{\infty} a_{c_n} \cos\frac{2\pi}{T}nt + \sum_{n=1}^{\infty} b_{c_n} \sin\frac{2\pi}{T}nt, & (3.31)\\ y_o(t) &:= a_{o_0} + \sum_{n=1}^{\infty} a_{o_n} \cos\frac{2\pi}{T}nt + \sum_{n=1}^{\infty} b_{o_n} \sin\frac{2\pi}{T}nt, & (3.32)\end{aligned}$$

respectively. Note that the amplitudes of the fundamental components in both $y_c^{(1)}$ and y_o are the same (from (3.25)), i.e. $\Upsilon_c := \sqrt{|a_{c_1}|^2 + |b_{c_1}|^2} = \sqrt{|a_{o_1}|^2 + |b_{o_1}|^2} =: \Upsilon_o$.

Let

$$\begin{aligned} e_o &:= y_o - \bar{y}_o = \epsilon\tilde{\Psi}(\frac{C}{1+C}r), & (3.33)\\ e_c &:= y_c - \bar{y}_c = \frac{1}{1+C}\epsilon\tilde{\Psi}(C\cdot r - C\cdot y_c(r)), & (3.34)\\ e_c^{(1)} &:= y_c^{(1)} - \bar{y}_c = \frac{1}{1+C}\epsilon\tilde{\Psi}(\frac{C}{1+C}r). & (3.35)\end{aligned}$$

From (3.33) and (3.35),

$$e_c^{(1)} = S e_o, \tag{3.36}$$

where $S := \frac{1}{1+C}$ is referred to as the *sensitivity* function for the system in Figure 3.11, when $\epsilon \equiv 0$.

Note that e_o is periodic in the steady-state (from (3.33) and recalling that $\tilde{\Psi}$ is static). Therefore, in the steady-state, $e_c^{(1)}$ will be periodic, as well. So, using (3.25), (3.31), (3.32), (3.33), and (3.35), the Fourier decompositions of $e_c^{(1)}$ and e_o are given by

$$\begin{aligned} e_c^{(1)}(t) &= a_{c_0} + \sum_{n=2}^{\infty} a_{c_n} \cos\frac{2\pi}{T}nt + \sum_{n=2}^{\infty} b_{c_n} \sin\frac{2\pi}{T}nt, & (3.37)\\ e_o(t) &= a_{o_0} + \sum_{n=2}^{\infty} a_{o_n} \cos\frac{2\pi}{T}nt + \sum_{n=2}^{\infty} b_{o_n} \sin\frac{2\pi}{T}nt, & (3.38)\end{aligned}$$

respectively, i.e. they have the same expansions as $y_c^{(1)}$ and y_o, except that the fundamental components are removed. Then, for $\{k\}_{k=2}^{\infty}$,

$$\begin{aligned} a_{c_0} &= S(0)a_{o_0}, & (3.39)\\ a_{c_k} + b_{c_k}j &= S\left(j\frac{2\pi k}{T}\right)\left(a_{o_k} + b_{o_k}j\right), & (3.40)\end{aligned}$$

where $j := \sqrt{-1}$.

Next, augment a LTI system W to the output of the system in Figure 3.11, as shown in Figure 3.13. Note that $v = Wy_c$ and $v^{(1)} := Wy_c^{(1)}$.

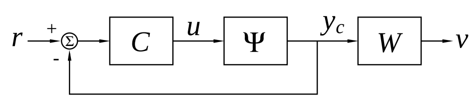

Figure 3.13: Static Nonlinearity in Dynamic Feedback with Augmented Weight

Then, (3.39) and (3.40) are modified such that for $\{k\}_{k=2}^{\infty}$,

$$\begin{aligned} \hat{a}_{c_0} &:= W(0)a_{c_0} = W(0)S(0)a_{o_0}, & (3.41)\\ \hat{a}_{c_k} + \hat{b}_{c_k}j &:= W\left(j\frac{2\pi k}{T}\right)\left(a_{c_k} + b_{c_k}j\right) & \\ &= W\left(j\frac{2\pi k}{T}\right)S\left(j\frac{2\pi k}{T}\right)\left(a_{o_k} + b_{o_k}j\right). & (3.42)\end{aligned}$$

It should be noted that $\hat{a}_{c_0}$, $\{\hat{a}_{c_n}\}_{n=2}^{\infty}$, and $\left\{\hat{b}_{c_n}\right\}_{n=2}^{\infty}$ are the Fourier coefficients of $We_c^{(1)}$.

Define the 2-norm for periodic signals with period T as

$$\|y\|_2^2 = \frac{1}{T}\int_0^T |y(t)|^2\, dt. \tag{3.43}$$

Applying *Parseval's* relationship for periodic signals to e_o and $We_c^{(1)}$ yields [42]

$$\begin{aligned} \|e_o\|_2^2 &= |a_{o_0}|^2 + \sum_{n=2}^{\infty}\left(|a_{o_n}|^2 + |b_{o_n}|^2\right), & (3.44)\\ \left\|We_c^{(1)}\right\|_2^2 &= |\hat{a}_{c_0}|^2 + \sum_{n=2}^{\infty}\left(|\hat{a}_{c_n}|^2 + \left|\hat{b}_{c_n}\right|^2\right), & (3.45)\end{aligned}$$

respectively. Therefore, from (3.41) and (3.42),

$$\begin{aligned}
&\left\|We_c^{(1)}\right\|_2^2 = \\
&|W(0)S(0)a_{o_0}|^2 + \sum_{n=2}^{\infty}\left|W\left(j\frac{2\pi n}{T}\right)S\left(j\frac{2\pi n}{T}\right)\right|^2\left(|a_{o_n}|^2+|b_{o_n}|^2\right), \\
&|\hat{a}_{c_0}|^2 + \sum_{n=2}^{\infty}\left(|\hat{a}_{c_n}|^2+\left|\hat{b}_{c_n}\right|^2\right) = \\
&|W(0)S(0)a_{o_0}|^2 + \sum_{n=2}^{\infty}\left|W\left(j\frac{2\pi n}{T}\right)S\left(j\frac{2\pi n}{T}\right)\right|^2\left(|a_{o_n}|^2+|b_{o_n}|^2\right).
\end{aligned} \tag{3.46}$$

From (3.41), $|\hat{a}_{c_0}|^2 = |W(0)S(0)a_{o_0}|^2$. So, (3.46) simplifies to

$$\sum_{n=2}^{\infty}\left(|\hat{a}_{c_n}|^2+\left|\hat{b}_{c_n}\right|^2\right) = \sum_{n=2}^{\infty}\left|W\left(j\frac{2\pi n}{T}\right)S\left(j\frac{2\pi n}{T}\right)\right|^2\left(|a_{o_n}|^2+|b_{o_n}|^2\right), \tag{3.47}$$

$$\begin{aligned}
\sqrt{\sum_{n=2}^{\infty}\left(|\hat{a}_{c_n}|^2+\left|\hat{b}_{c_n}\right|^2\right)} &= \sqrt{\sum_{n=2}^{\infty}\left|W\left(j\frac{2\pi n}{T}\right)S\left(j\frac{2\pi n}{T}\right)\right|^2\left(|a_{o_n}|^2+|b_{o_n}|^2\right)} \\
&\leq \|WS\|_\infty\sqrt{\sum_{n=2}^{\infty}\left(|a_{o_n}|^2+|b_{o_n}|^2\right)}.
\end{aligned} \tag{3.48}$$

Dividing (3.48) by $\Upsilon_c = \Upsilon_o$, and manipulating gives

$$\begin{aligned}
\frac{\sqrt{\sum_{n=2}^{\infty}\left(|\hat{a}_{c_n}|^2+\left|\hat{b}_{c_n}\right|^2\right)}}{\Upsilon_c} &\leq \|WS\|_\infty\frac{\sqrt{\sum_{n=2}^{\infty}\left(|a_{o_n}|^2+|b_{o_n}|^2\right)}}{\Upsilon_o}, \\
\frac{\left|W\left(j\frac{2\pi}{T}\right)\right|\sqrt{\sum_{n=2}^{\infty}\left(|\hat{a}_{c_n}|^2+\left|\hat{b}_{c_n}\right|^2\right)}}{\left|W\left(j\frac{2\pi}{T}\right)\right|\Upsilon_c} &\leq \|WS\|_\infty\frac{\sqrt{\sum_{n=2}^{\infty}\left(|a_{o_n}|^2+|b_{o_n}|^2\right)}}{\Upsilon_o}.
\end{aligned} \tag{3.49}$$

From (3.6), the distortions for the systems in Figures 3.12 and 3.13, when y_o and $v^{(1)}$ are the outputs due to $r := \bar{r}\sin(\omega t)$ and $\omega := \frac{2\pi}{T}$, are given by

$$\mathrm{THD}_{\mathrm{A_o}}(\Upsilon_o,\omega) := \frac{\sqrt{\sum_{n=2}^{\infty}\left(|a_{o_n}|^2+|b_{o_n}|^2\right)}}{\Upsilon_o}, \tag{3.50}$$

$$\mathrm{THD}_{\mathrm{A_c}}(\hat{\Upsilon}_c,\omega) := \frac{\sqrt{\sum_{n=2}^{\infty}\left(|\hat{a}_{c_n}|^2+\left|\hat{b}_{c_n}\right|^2\right)}}{\hat{\Upsilon}_c}, \tag{3.51}$$

respectively, where $\hat{\Upsilon}_c := \sqrt{|\hat{a}_{c_1}|^2 + \left|\hat{b}_{c_1}\right|^2}$ is the amplitude of the fundamental component in $v^{(1)}$. Note that $\hat{\Upsilon}_c = |W(j\omega)|\,\Upsilon_c$. Substituting into (3.49) yields

$$|W(j\omega)|\,\mathrm{THD}_{\mathrm{A_c}}\left(\hat{\Upsilon}_c, \omega\right) \leq \|WS\|_\infty \mathrm{THD}_{\mathrm{A_o}}\left(\Upsilon_o, \omega\right) \tag{3.52}$$

Choose W such that $|W(j\omega)|\,\big|_{\omega\in[\omega_1,\omega_2]} = 1$, while trailing off to zero elsewhere, where $[\omega_1, \omega_2]$ is the frequency range of interest. Then, for $\omega \in [\omega_1, \omega_2]$,

$$\hat{\Upsilon}_c = |W(j\omega)|\,\Upsilon_c \;=\; \Upsilon_c, \tag{3.53}$$

$$|W(j\omega)|\,\mathrm{THD}_{\mathrm{A_c}}\left(\hat{\Upsilon}_c, \omega\right) \;=\; \mathrm{THD}_{\mathrm{A_c}}\left(\Upsilon_c, \omega\right). \tag{3.54}$$

Finally, (3.52) becomes

$$\mathrm{THD}_{\mathrm{A_c}}\left(\Upsilon_c, \omega\right) \leq \|WS\|_\infty \mathrm{THD}_{\mathrm{A_o}}\left(\Upsilon_o, \omega\right) =: \mathrm{THD}_{\mathrm{A_{cp}}}\left(\Upsilon_c, \omega\right),\; \omega \in [\omega_1, \omega_2]\,. \tag{3.55}$$

3.4.3 Examples

To illustrate the linearizing effect of feedback, three examples have been devised (two for static and one for dynamic feedback) using the nonlinear functions (3.11) and (3.12), which are plotted in Figures 3.2 and 3.4.

Static Feedback

Implementing the interconnection shown in Figure 3.10 on each nonlinearity using a feedback gain of $K := 5$, the closed-loop relationship is given implicitly by (3.21). The closed-loop maps and their corresponding distortion plots (using $\mathrm{THD_A}$ as the measure) are shown in Figures 3.14, 3.15, 3.16, and 3.17. Note that the plots in Figures 3.15 and 3.17 compare the distortion in the output of the feedback interconnection with that of Figure 3.12, where $T := \frac{K}{1+K}$.

As shown in the figures, the linearizing effect is significant, with $\mathrm{THD}_{\mathrm{A_{cp}}} \approx \mathrm{THD}_{\mathrm{A_c}}$ for small Υ.

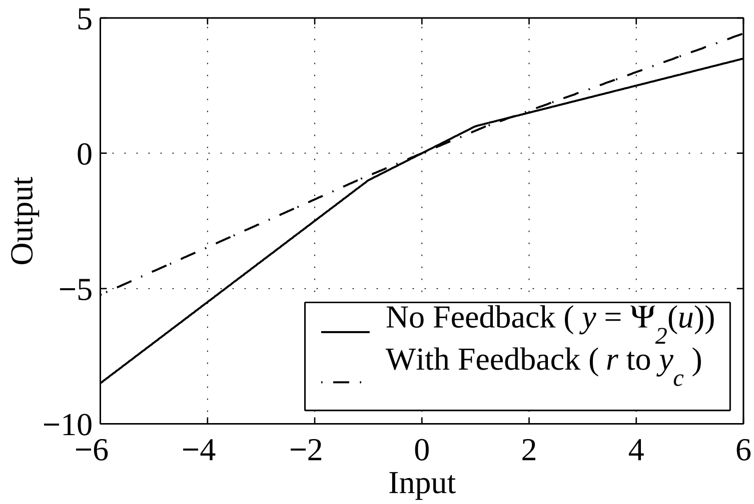

Figure 3.14: Effect of Static Feedback on the Piecewise Linear Map ($K = 5$)

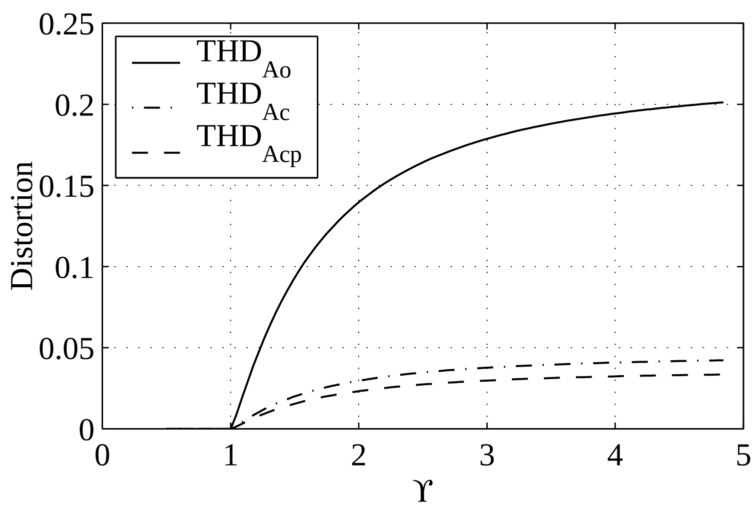

Figure 3.15: Distortion Plot for the Closed-Loop System with the Piecewise Linear Map (Static Feedback: $K = 5$)

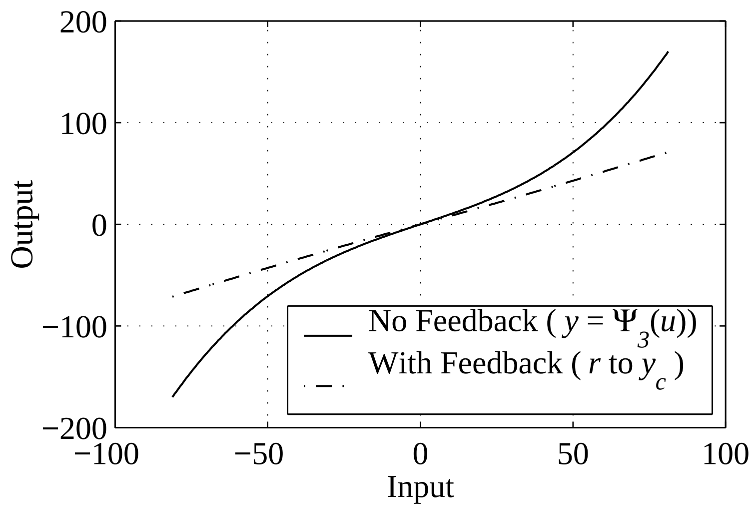

Figure 3.16: Effect of Static Feedback on the Cubic Polynomial Map ($K = 5$)

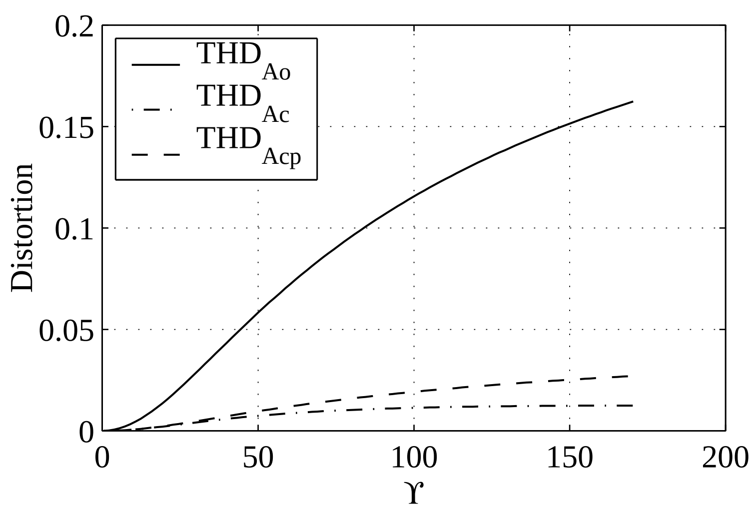

Figure 3.17: Distortion Plot for the Closed-Loop System with the Cubic Polynomial Map (Static Feedback: $K = 5$)

Dynamic Feedback

Consider the feedback interconnection shown in Figure 3.11, where the static nonlinear map (3.12) is in feedback with a dynamic system C. The distortion in the output of this system ($=:\mathrm{THD}_{\mathrm{A_c}}$) will be compared with the distortion in the output of the system shown in Figure 3.12 ($=:\mathrm{THD}_{\mathrm{A_o}}$), where the map (3.12) is pre-filtered by the linear system T (the complementary sensitivity function when $\epsilon \equiv 0$). In this example,

$$C(s) \;:=\; \frac{490s(s+6.65)(s+375.85)}{(s+10)^2(s+250)^2}, \tag{3.56}$$

$$S(s) \;:=\; \frac{1}{1+C} = \frac{(s+10)^2(s+250)^2}{(s+5)^2(s+500)^2}, \tag{3.57}$$

$$T(s) \;:=\; \frac{C}{1+C} = \frac{490s(s+6.65)(s+375.85)}{(s+5)^2(s+500)^2}, \tag{3.58}$$

are all stable. The frequency response of S (shown in Figure 3.18) illustrates the distortion reduction potential in the region between 0.1 Hz and 1 kHz. Simulating

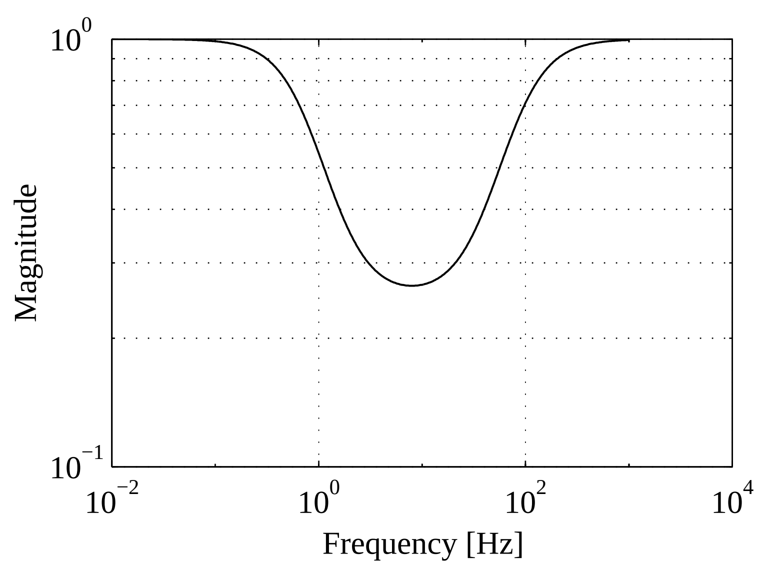

Figure 3.18: Frequency Response of S

the systems using sine-wave inputs and allowing the outputs to reach their steady states, Figure 3.19 shows the distortions for various frequencies and amplitudes. The distortion reduction is most significant at frequencies where the magnitude of S was small, e.g. the case for sine-wave inputs at 6 Hz. For sine-wave frequencies near 150 Hz, the distortion reduction was minimal. Furthermore, $\mathrm{THD}_{\mathrm{A_{cp}}}$ shows good agreement with $\mathrm{THD}_{\mathrm{A_c}}$ for small Υ.

As shown by the examples, in the instances where the nonlinear distortion is low, nonlinear distortion reduction can be incorporated as a control objective using linear control theory by designing the controller for the system's linearization such that the magnitude of S is less than unity in the frequency range of interest. This is the subject of Chapter 4.

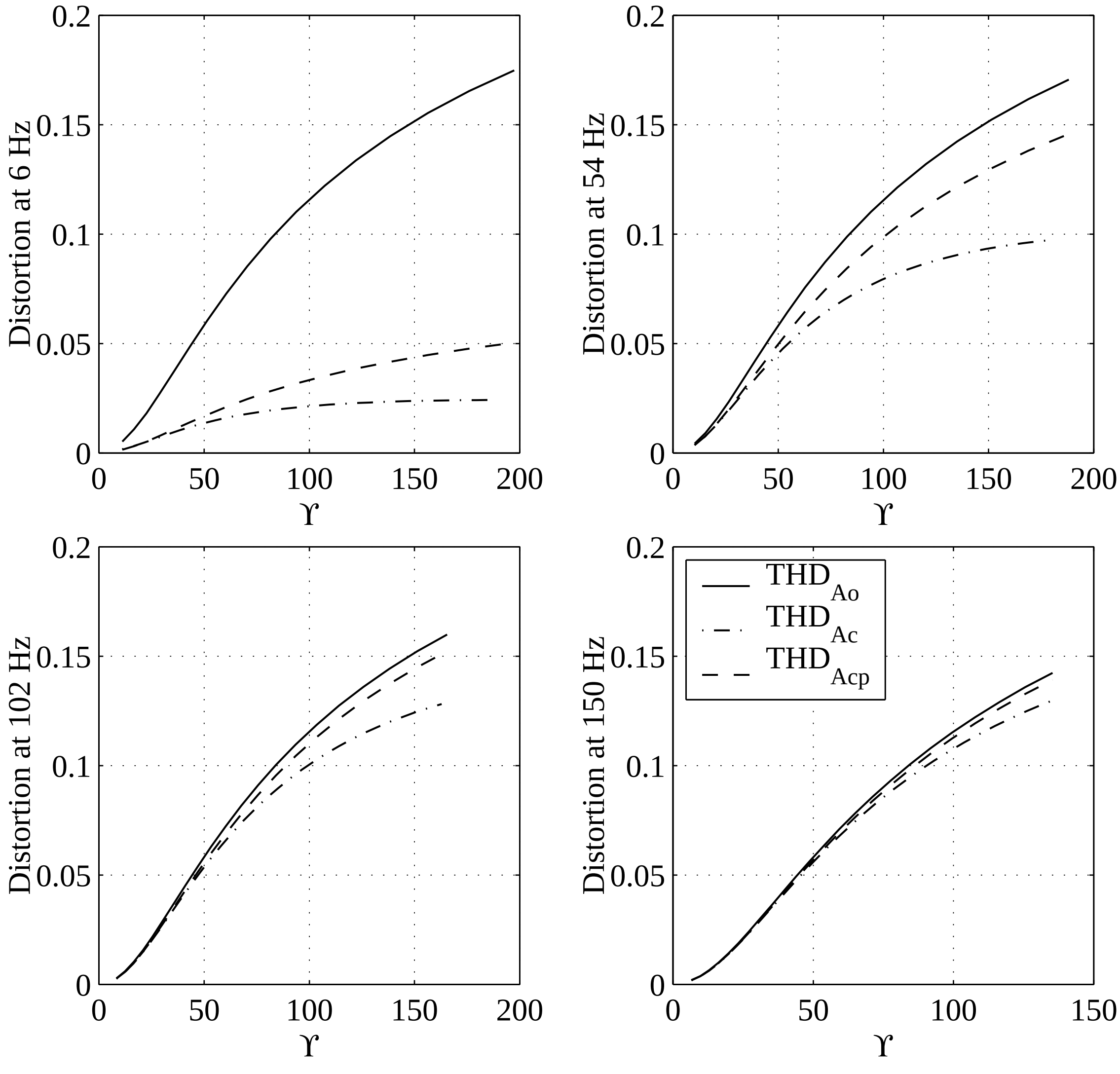

Figure 3.19: Distortion Plot for the Closed-Loop System with the Cubic Polynomial Map (Dynamic Feedback)

Chapter 4

Compensator Design

It was shown in Chapter 3 that to reduce the distortion in the output of a mildly nonlinear system (i.e. very linear for small signals), it was sufficient to design a linear feedback controller such that the magnitude of the sensitivity function S of the closed-loop system's linearization is smaller than unity, in the frequency range of interest. This design process is the focus of this chapter.

Consider the control system shown in Figure 4.1 where C, d_{ref}, u, and p are the controller to be designed, the system's input signal, the control signal to the amplifier, and the measurement of pressure for feedback, respectively. As shown, C has

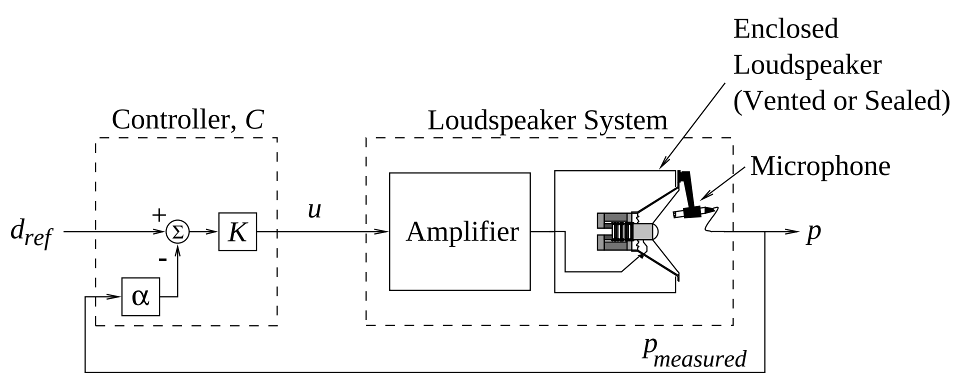

Figure 4.1: The Implemented Loudspeaker Control System

the special structure for which K contains all the dynamics and α is a nonzero normalizing constant factor such that $\frac{1}{\alpha}$ is equal to the peak in the magnitude frequency response of transfer function from u to p (for the system's linearization). Also, the dynamics of the loudspeaker system include that of the loudspeaker, amplifier, and microphone. It should be noted that the exogenous disturbances and noises are not shown in this figure. Also note that the pressure measurement is obtained via a microphone mounted as close to the loudspeaker's cone as possible, without mechanical interference. Locating it in this manner both minimizes the pure time-delay introduced in the feedback loop and increases the static gain in the map from the pressure near the cone's surface to that at the microphone's location.

The linear performance objective is to minimize the magnitude of S in the low frequency region (typically from 20 Hz to 200 Hz). This must be achieved while satisfying the following requirements:

1. Insensitivity to sensor noise.

2. Robustness of the closed-loop stability to:

   - Unmodeled dynamics: Linear model fit vs. actual plant, changes in the acoustic environment, aging, etc.

   - Disturbances: Extraneous sounds (e.g. slamming doors, sound from other loudspeakers), user touching the loudspeaker's cone, etc.

4.1 Performance Improvement: μ-Design

The design approach follows the continuous-time domain, *μ-Analysis and Synthesis* technique applied to Multi-Input, Multi-Output (MIMO) systems as proposed in [60] and described in [43]. Figure 4.2 shows the general representation of the problem, where P represents the known plant dynamics, K is the controller to be designed, and Δ is a problem dependent uncertainty. Hence, the interconnection containing the pair (P, Δ) represents the uncertain plant model.

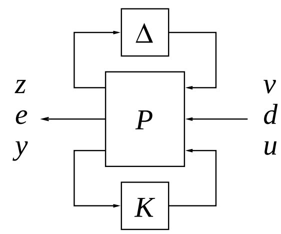

Figure 4.2: μ-Analysis and Synthesis Framework

The problem description is complete when the representation is combined with an appropriate magnitude measure for matrix transfer functions and several key results. The generalized system P contains three pairs of input/output variables: The control inputs $u(t)$ and the measured outputs $y(t)$, the disturbances $d(t)$ and performance variables $e(t)$, and the signals $v(t)$ which contain unit-norm perturbations that are fed back into P and the output signals $z(t)$ feeding into the perturbation Δ. Any linear interconnection of inputs and outputs can be cast into this general framework.

4.1.1 μ-Analysis

The goal is to find a non-conservative necessary and sufficient condition for robust performance for the system in Figure 4.3 (derived from Figure 4.2).

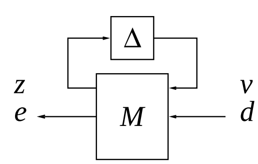

Figure 4.3: μ-Analysis Framework

$M(P, K)$ contains a 2×2 block-structured transfer function $M(s)$ which is defined in terms of a 3×3 partition of $P(s)$ in the original interconnect in Figure 4.2 by

$$M_{ij}(s) := P_{ij}(s) + P_{i3}(s)\left[I - K(s)P_{33}(s)\right]^{-1} K(s)P_{3j}(s), \qquad i, j = 1, 2. \tag{4.1}$$

Formulation (4.1) is referred to as a *Linear Fractional Transformation of P through*

K, hence $M(P, K)$. The following is true when the system shown in Figure 4.3 is stable:

1. Nominal Performance is achieved if and only if

$$\|M_{22}(j\omega)\|_\infty < 1. \tag{4.2}$$

2. Robust Stability is achieved if and only if

$$\|M_{11}(j\omega)\|_\infty < 1. \tag{4.3}$$

3. Robust Performance is achieved if and only if

$$\mu\left(M(j\omega)\right) < 1 \;\; \forall\omega, \tag{4.4}$$

where

$$\mu\left(M(j\omega)\right) := \left[\min\left\{\epsilon \;\middle|\; \begin{array}{l} \det\left(I - \epsilon X M(j\omega)\right) = 0 \\ \text{for some } X = \operatorname{diag}(\Delta_1, \Delta_2) \\ \text{with } \bar{\sigma}\left(\Delta_i\right) < 1, \; \forall i \end{array}\right\}\right]^{-1}, \tag{4.5}$$

i.e., μ is the reciprocal of the smallest scalar ϵ which makes $I - \epsilon X M(j\omega)$ singular for some X in a block diagonal perturbation set. μ is zero if no ϵ exists.

The function μ was defined in [15] for the observation that robust performance is equivalent to robust stability in the presence of *two* perturbations Δ, and Δ_p, which are connected around $M(P, K)$. Therefore, robust stability is guaranteed if and only if

$$\det\left(I - \operatorname{diag}(\Delta, \Delta_p) M(j\omega)\right) \neq 0 \;\; \forall\omega. \tag{4.6}$$

This is a tight condition for robust stability with respect to two perturbation blocks (and equivalently, for robust performance). Since the definition in (4.5) can also be used to test for stability with respect to many diagonal blocks (not just 2×2 block structures), it can be utilized to test for robust stability with respect to plant sets characterized by several unstructured perturbations (and at the same time, test for robust performance, as well).

4.1.2 μ-Synthesis

The synthesis problem is to find a controller K such that the performance objectives are met under specified uncertainties. Figure 4.4 shows the synthesis framework where the perturbations are normalized to unity and the normalizing factors are absorbed into P.

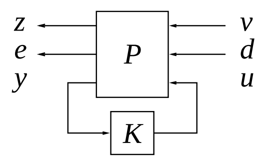

Figure 4.4: μ-Synthesis Framework

Partition P so that the map from $\begin{bmatrix} v \\ d \end{bmatrix}$ to $\begin{bmatrix} z \\ e \end{bmatrix}$ is described by

$$\begin{bmatrix} z \\ e \end{bmatrix} = M(P, K) \begin{bmatrix} v \\ d \end{bmatrix}. \tag{4.7}$$

The goal is to find a stabilizing controller such that

$$\|M(P, K)\|_\infty < \gamma, \tag{4.8}$$

where γ is the inverse of the minimum norm of the perturbation that causes the closed-loop system to become unstable. This goal is referred to as the $\mathcal{H}_\infty$ *optimal problem*. Further details can be found in [20] and [17].

Combining the analysis and synthesis frameworks in a systematic fashion such that the $\mathcal{H}_\infty$ optimal control methods and the structured singular value (μ) theory are used for synthesis and analysis, respectively, results in the *μ-Analysis and Synthesis* algorithm. The method reduces to finding a stabilizing controller K and a scaling matrix D that minimize $\|DM(P, K)D^{-1}\|_\infty$. In practice, this is solved by fixing D and minimizing with respect to K ($\mathcal{H}_\infty$ problem), then fixing the resulting K and performing the minimization with respect to D (convex optimization problem), point-wise in frequency. The resulting $D(jw)$ is then fit with a real-rational, stable, and minimum phase invertible transfer function. The algorithm is repeated until a suitable minimum is achieved. This is referred to as the *D-K Iteration* algorithm and is explained in more detail in [60] and [4].

4.2 μ-Synthesis for the Loudspeaker System

4.2.1 System Interconnection Model

Figure 4.5 is a diagram for the closed-loop system model containing considerations (in terms of weighting functions) which are necessary in achieving the design goals. By opening the connections around Δ and K (the dotted blocks) and combining

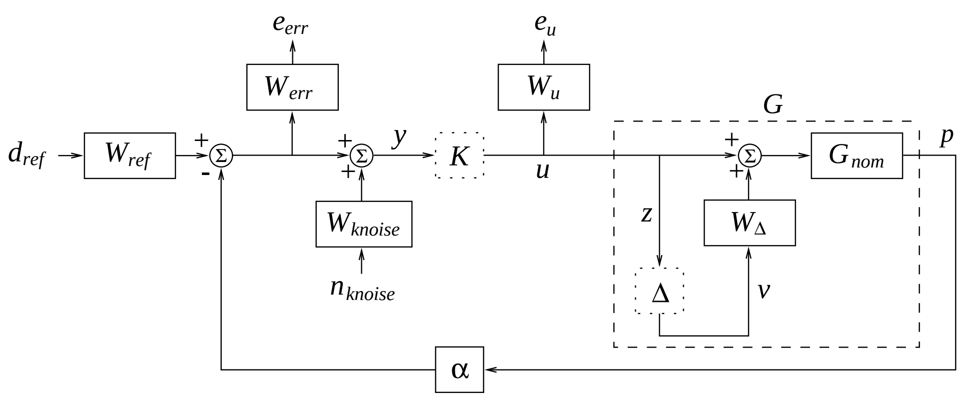

Figure 4.5: The Closed-Loop Interconnection Structure

the disturbance and error signals, the system is transformed into P, the open-loop interconnection structure shown in Figure 4.6, which is suitable for the μ-framework described in Section 4.1. Therefore, P is a 4×4 interconnection structure and the

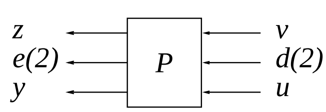

Figure 4.6: Transformed Interconnection Structure for the μ-Problem

blocks and signals involved are defined as follows:

n_{knoise}: noise at the controller's input,

d_{ref}: reference command,

e_{err}: weighted error (sensitivity) signal,

e_u: weighted control signal,

$d(2)$: disturbance vector $\begin{bmatrix} n_{knoise} \\ d_{ref} \end{bmatrix}$,

$e(2)$: error vector $\begin{bmatrix} e_{err} \\ e_u \end{bmatrix}$,

G_{nom}: nominal plant, which is the nominal loudspeaker system's linearization,

G: uncertain plant,

W_{Δ}: multiplicative uncertainty weight,

W_{err}: error signal performance weight,

W_{knoise}: noise penalty weight,

W_u: control signal penalty weight, and

W_{ref}: reference command weight.

4.2.2 Uncertainty and Performance Objectives Modeling

In order to accurately reflect the control objectives in the μ-framework, frequency-dependent weights multiplying the appropriate signals are utilized, as shown in Figure 4.5. Figure 4.7 shows a set of weights used as an example to guide the following description (these weights will be applied to a problem involving an actual loudspeaker attached to a sealed enclosure, as detailed in Chapter 5):

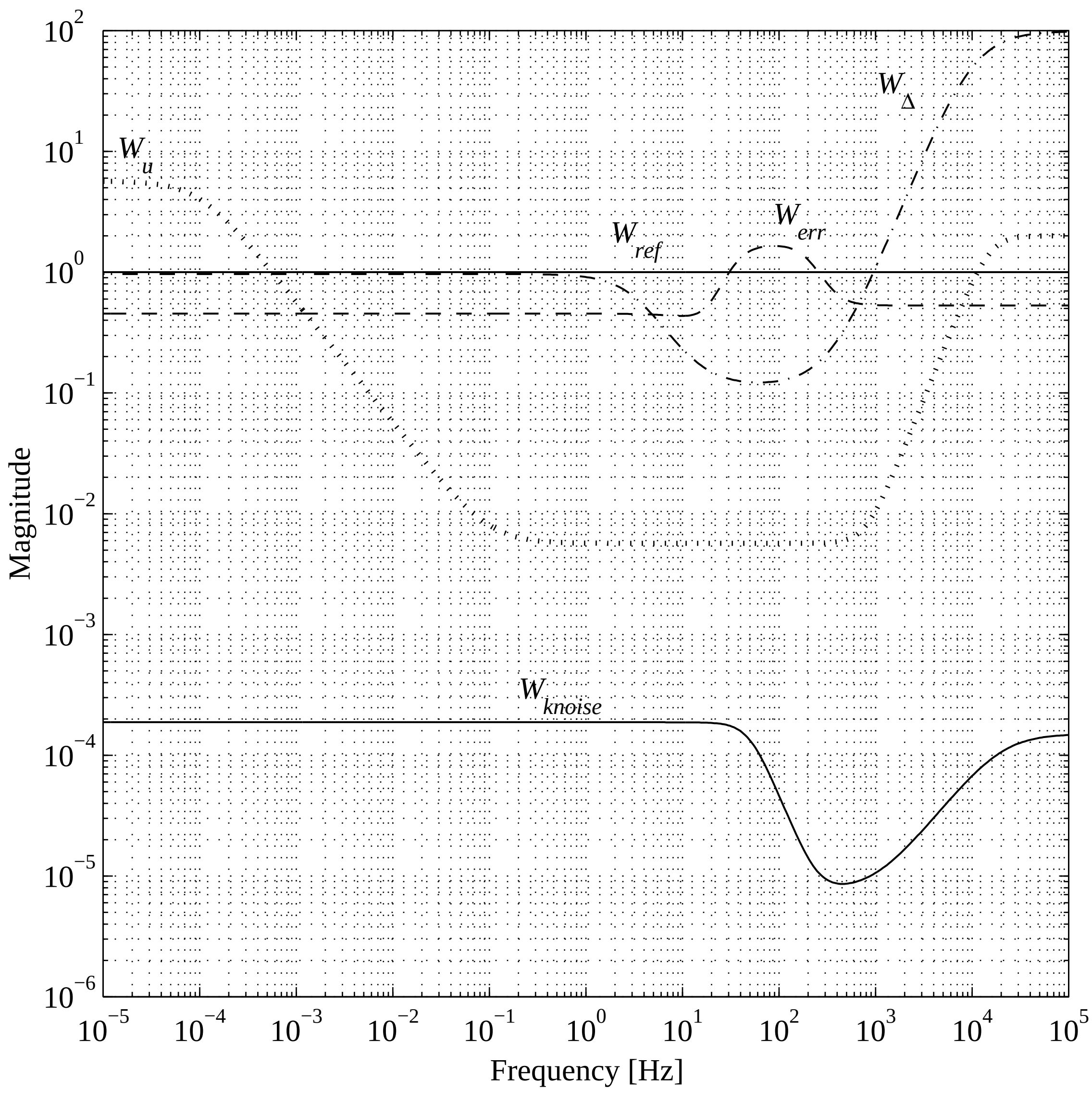

Figure 4.7: Uncertainty and Performance Weights

Uncertainty Modeling: The dashed block G in Figure 4.5 represents the linearization of the "true" loudspeaker system, shown in Figure 4.1. The elements W_Δ and Δ parameterize the modeling uncertainty. The uncertainty model is referred to as the *multiplicative uncertainty at the plant input* which is described by

$$G \in \{G_{nom}\,(I + W_\Delta \Delta) : \|\Delta\|_\infty \leq 1\}\,. \tag{4.9}$$

Figure 4.7 shows the frequency response of W_Δ. The 4^{th}-order, stable weight reflects the modeling uncertainty along with the desired robustness. Reaching a minimum magnitude of approximately 0.12 at 62 Hz, the closed loop system is required to be impervious to at least a 12% variation in G over all frequencies, up to 100% at low frequencies, and up to 10000% at high frequencies.

Performance Weight: W_{err} is used to reflect the desired closed-loop frequency response of the system from d_{ref} to e_{err} (the weighted response of the closed-loop sensitivity function $S := \frac{1}{1+\alpha GK}$). Using this weight penalizes the magnitude response of S such that it does not exceed that of W_{err}^{-1}. The weight is formulated so that the magnitude of S is required to be smaller than unity in the frequency range of interest, hence achieving a reduction in the loudspeaker's pressure distortion. Also, define $T := \frac{\alpha GK}{1+\alpha GK}$ to be the complementary sensitivity function of the closed-loop system. Then, the identity $S + T = 1$ always holds. Hence, $|S(j\omega)| = |1 - T(j\omega)| \;\; \forall \omega \in \mathbb{R}$. Therefore, penalizing $|S(j\omega)|$ so that it is small and flat in the desired frequency range penalizes $|T(j\omega)|$ so that it is flat in that region, as well. Since α is a nonzero constant, flattening the frequency response of T also flattens that of $\frac{1}{\alpha}T$, which is the transfer function from d_{ref} to p. Taking these issues into account, the weight shown in Figure 4.7 was designed to be a stable, 4^{th}-order transfer function. The magnitude of W_{err}^{-1} is less than unity from 31 Hz to 256 Hz and achieves a minimum of approximately 0.6 at 89 Hz.

Reference Signal Weight: W_{ref} is designed to reflect the ideal response to the reference command signal d_{ref}. Since the control objective involves tracking d_{ref} itself, $W_{ref} := 1.0$ (i.e. no frequency shaping of the reference signal), as shown in Figure 4.7.

Noise Weight: Noise contaminations from the measured pressure, plant, and controller is considered. The magnitude of the stable, 3$^{\text{rd}}$-order W_{knoise} shown in Figure 4.7 is treated as the upper bound for the actual noise present in y (Figure 4.5).

Control Signal Weight: The control signal is required to have an upper bound to prevent the amplifier from saturating, with possible damage to the loudspeaker. As a result, the 3$^{\text{rd}}$-order, stable W_u is formulated such that the magnitude of W_u^{-1} represents the upper limit of the magnitude of control signal u when $d_{ref} = 1$, as shown in Figure 4.7. By limiting the control action at high frequencies, this weight further helps in high-frequency noise rejection and in shaping the high frequency response of S.

4.3 Non-Minimum Phase Issues

In the case when the plant G contains non-minimum phase zeros, care must be taken when designing the performance weights [16], [69]. Let $[\omega_1, \omega_2]$ denote the frequency range for the spectrum of d_{ref} and define

$$\begin{aligned} b_1 &:= \max_{\omega_1 \leq \omega_2} \left| S(j\omega) \right|, && (4.10) \\ b_2 &:= \left\| S \right\|_\infty . && (4.11) \end{aligned}$$

The control objective is such that $b_1 \ll 1$ while b_2 is not allowed to be too large. Note that $b_2 \geq 1$, since unity is the value of S at infinite frequency. Suppose that the plant has a zero at $z_{np} := \sigma_0 + j\omega_0$, where $\sigma_0 > 0$ (non-minimum phase). Then, $S(z_{np}) = 1$, regardless of the controller. Define

$$c_1 := \frac{1}{\pi}\int_{\omega\in[-\omega_2,-\omega_1]\cup[\omega_1,\omega_2]} \frac{\sigma_0}{\sigma_0^2+(\omega-\omega_0)^2}\, d\omega, \tag{4.12}$$

$$c_2 := \frac{1}{\pi}\int_{\omega\notin[-\omega_2,-\omega_1]\cup[\omega_1,\omega_2]} \frac{\sigma_0}{\sigma_0^2+(\omega-\omega_0)^2}\, d\omega. \tag{4.13}$$

Note that c_1 and c_2 are positive constants that only depend on ω_1, ω_2, and z_{np}. Under these conditions, it can be shown that [16]

$$b_2 \geq \left(\frac{1}{b_1}\right)^{\frac{c_1}{c_2}}. \tag{4.14}$$

This implies that making $b_1 \ll 1$ simultaneously makes $b_2 \gg 1$.

In addition, define αGK to be the open-loop gain of the controlled loudspeaker system. Let $\{p_i\}$ denote the set of poles of αGK such that $\Re(p_i) > 0$ (unstable poles). Assume that the relative degree (:= the degree of the denominator minus the degree of the numerator) of αGK is at least 2. Then a formula for the area under the graph of $\log_{10}|S(j\omega)|$ vs. ω is given by [16]

$$\int_0^\infty \log_{10}|S(j\omega)|\; d\omega = \pi\log_{10}(e)\left(\sum_i \Re(p_i)\right), \tag{4.15}$$

implying that the area under $\log_{10}|S(j\omega)|$ is conserved. This means that if $|S(j\omega)| \ll 1$ for $\omega \in [\omega_1, \omega_2]$, then $|S(j\omega)| > 1$ elsewhere.

Also,

$$|W_{err}(z_{np})| = |W_{err}(z_{np})S(z_{np})| \leq \|W_{err}S\|_\infty. \tag{4.16}$$

Therefore, a necessary condition for the performance objective $\|W_{err}S\|_\infty < 1$ to be achievable is that $|W_{err}(z_{np})| < 1$. This puts constraints on the performance bandwidth. To show this consider the following example.

Let the plant G be strictly proper (i.e. $G(\infty) = 0$). The objective is to design a controller such that the magnitude of the sensitivity function S lies below that of the bound

$$Q(s) := \frac{2(s+\omega_l)}{s+\omega_p}, \tag{4.17}$$

where ω_p and ω_l are in $\mathbb{R}_+$ and $\omega_p > \omega_l$. Define ω_B so that $|Q(j\omega_B)| = 1$. Then, the bound requires a reduction in the magnitude of S for all frequencies up to ω_B, demands at least a level of $\frac{\omega_p}{2\omega_l}$ reduction for all frequencies up to ω_l, and allows for a worst-case peak of 2 for $\|S\|_\infty$. So, a stable, minimum-phase W_{err} is chosen such that

$$W_{err}(s) := Q^{-1}(s) = \frac{s+\omega_p}{2(s+\omega_l)}. \tag{4.18}$$

Note that $|W_{err}(j\omega_B)| = 1$, as well. This gives

$$\omega_B = \sqrt{\frac{\omega_p^2 - 4\omega_l^2}{3}}. \tag{4.19}$$

The frequency responses of both the performance bound and W_{err} are shown in Figure 4.8. Suppose that G has a zero at $z_{np} := \sigma_0 + j\omega_0$, where $\sigma_0 > 0$. Assume that there

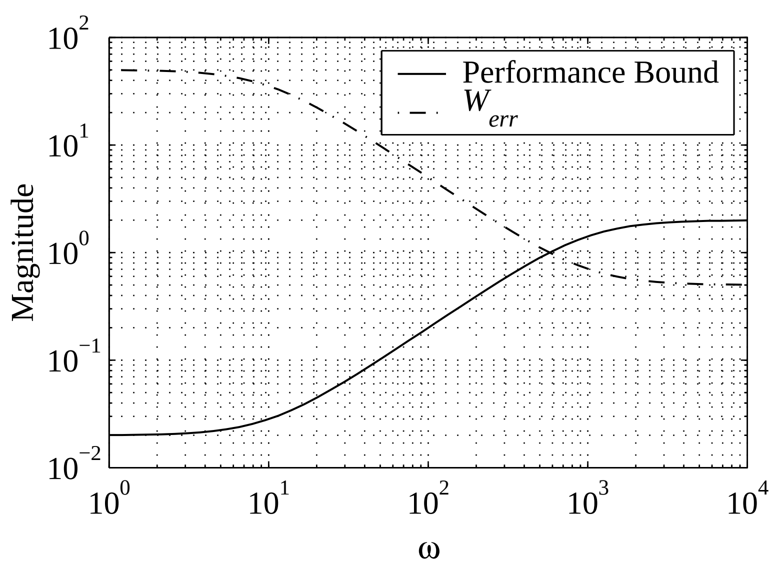

Figure 4.8: Performance Bound and W_{err} ($\omega_l = 10$ and $\omega_p = 1000$, for this plot)

is a stabilizing controller K such that $\|W_{err}S\|_\infty < 1$. Then, $|W_{err}(z_{np})| < 1$ has to hold if the performance objective is to be achieved. Using (4.18) yields

$$\frac{1}{2}\left|\frac{\sigma_0 + j\omega_0 + \omega_p}{\sigma_0 + j\omega_0 + \omega_l}\right| < 1. \tag{4.20}$$

Substituting (4.19) and simplifying gives

$$\omega_B^2 < \left(\sigma_0^2 + \omega_0^2\right) - \frac{2}{3}\sigma_0 \left(\omega_p - 4\omega_l\right). \tag{4.21}$$

Note that if $\omega_0 = 0$ (i.e. the zero is real), the relationship reduces to (after some manipulation)

$$\sigma_0 > \sqrt{3\omega_B^2 + 4\omega_l^2} - 2\omega_l. \tag{4.22}$$

Taking the limit as $\omega_l \to 0$ gives

$$\omega_B < \frac{\sigma_0}{\sqrt{3}}. \tag{4.23}$$

Coupling the above facts, the frequency response of the magnitude of S will contain peaks larger than unity, if G is non-minimum phase. Although inevitable, this is not desirable, since the performance is degraded there. This design tradeoff requires careful attention in the choice of W_{err}.

Therefore, W_{err} is chosen so that the bandwidth limits set by the non-minimum phase zeros are not exceeded, while ensuring that the unavoidable peaks above unity in the magnitude response of the sensitivity function are not too large. For the example weight in Figure 4.7, W_{err} was designed for a plant with dynamics exhibiting non-minimum phase zeros at $63 \pm 46.4j$ and 5723 rad/s. Therefore, $|W_{err}(j\omega)| < 1$ for frequencies in the intervals $[0, 31\,\mathrm{Hz})$ and $(256\,\mathrm{Hz}, \infty)$, while the weight allows for peaks (larger than unity) in the magnitude of S of up to 2.3 for frequencies in the interval $[0, 31\,\mathrm{Hz})$ and up to 1.9 in the interval $(256\,\mathrm{Hz}, \infty)$.

Chapter 5

Applications and Examples

In this chapter, the results of Chapters 2, 3, and 4 are illustrated by means of three loudspeaker examples: one based on the loudspeaker model of Chapter 2 and two based on real systems. In each example, a μ-controller is designed and the performance improvement is determined. The data is compared with the theoretical predictions and the suitability and usefulness of the developed theory to loudspeaker systems is illustrated.

5.1 Loudspeaker Model in a Vented Enclosure

Figure 5.1 shows a schematic of a loudspeaker in an insulated and vented enclosure attached to an infinite baffle in an acoustic half-space, where u is the voice-coil voltage, p and p_{f} are pressures measured at $(x = 0, y = 0, z = 0.032)$ (in meters) (i.e. 1.25 inches from the cone's surface) and $(x = 0, y = -0.15, z = 1)$ meters, respectively. A cylindrical duct mounted to the enclosure's vent has its centerline located at $(x = 0, y = -0.29)$ meters.

Using the loudspeaker model from Chapter 2, Figure 5.2 shows a schematic of the interconnection describing the loudspeaker model in a vented enclosure, where the components and signals are defined as

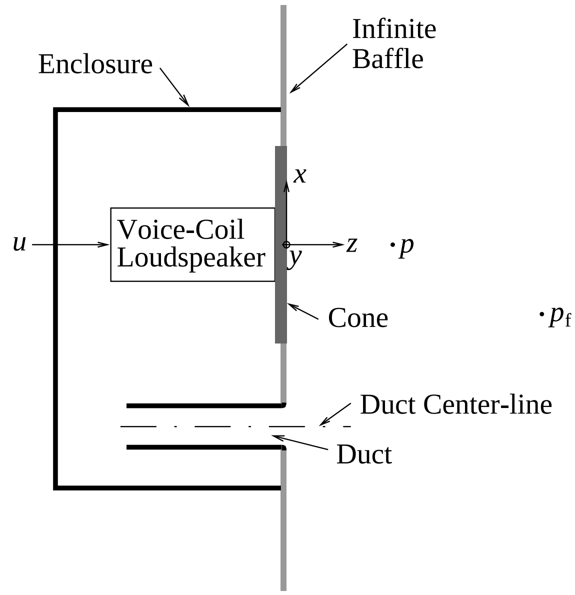

Figure 5.1: Loudspeaker in a Vented Enclosure

Ω_1, Ω_2: cross sectional areas of the faces of the loudspeaker's cone and duct, respectively,

z_1, $\dot{z}_1$: cone's position and velocity, respectively,

z_{2_0}, $\dot{z}_{2_0}$, $\ddot{z}_{2_0}$: position, velocity, and acceleration of the air particles on the face of the duct lying inside the enclosure, respectively,

$\ddot{z}_{2_L}$: acceleration of the air particles on the face of the duct (baffle side),

p_{b}: pressure inside the enclosure $(=: p_{\mathrm{b}}(z_1, z_{2_0}))$,

F_{b}: force exerted on the surface of the loudspeaker's cone (facing the inside of the enclosure), due to p_{b} $(F_{\mathrm{b}} := \Omega_1 p_{\mathrm{b}})$,

F_1, F_2: forces exerted on the surface of the loudspeaker's cone and the face of the duct (baffle side), respectively, due to the acoustic environment, and

p_2: pressure acting on the face of the duct (baffle side), due to F_2 $(p_2 := \frac{F_2}{\Omega_2})$.

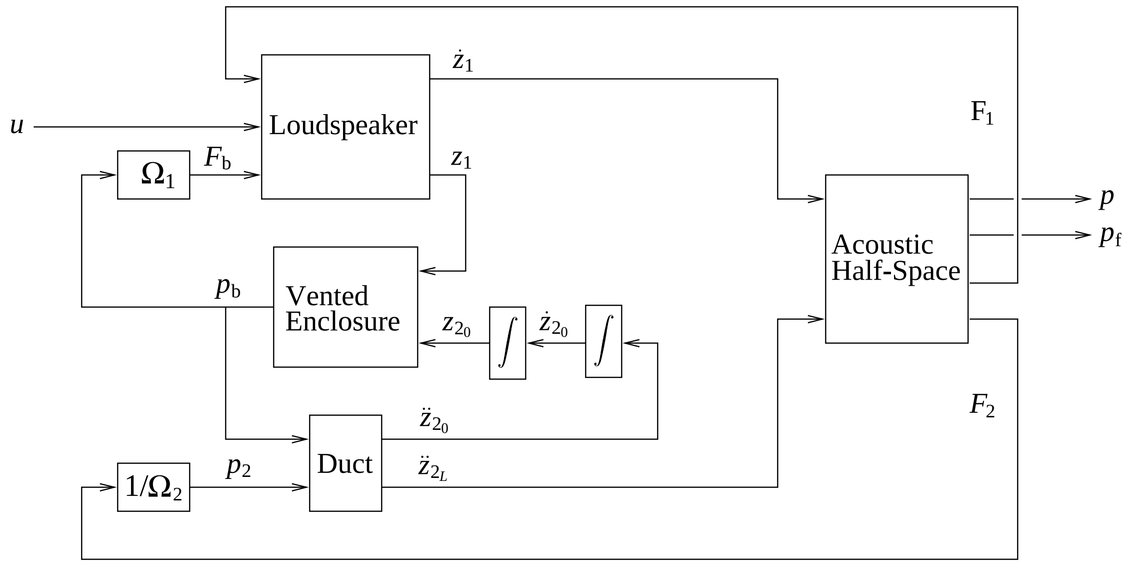

Figure 5.2: Schematic of the Loudspeaker Model in a Vented Enclosure

As the figure illustrates, the system is comprised of several components:

Loudspeaker: voice-coil loudspeaker attached to one of the enclosure's openings, with the following parameter values:

a_1**:** radius of the cone = 0.163 m,

Ω_1**:** cross-sectional area of the cone $:= \pi a_1^2 = 0.083$ m^2,

m**:** moving mass = 0.117 kg,

L_e**:** voice-coil inductance = 7×10^{-4} H,

R_e**:** voice-coil resistance = 3 Ω,

Bl_0**:** linear force factor = 30.66 T $\cdot$ m,

Bl_1**:** nonlinear force factor = 10^7 m^{-4},

κ**:** exponent in the nonlinear force term = 4,

k_0**:** linear spring constant = 5376 N/m,

k_1**:** quadratic spring coefficient = 0,

k_2**:** cubic spring coefficient $= 2 \times 10^8$ N/m^3, and

R_m**:** mechanical damping factor $= 12.83$ N $\cdot$ s/m.

Duct: cylindrical duct attached to one of the enclosure's vents with

a_2**:** radius of the duct's face $= 0.108$ m,

Ω_2**:** cross-sectional area of the duct's face $:= \pi a_2^2 = 0.037$ m^2,

L**:** duct's length $= 0.381$ m (15 inches),

N**:** number of finite-difference divisions in the duct $= 40$,

ρ_0**:** equilibrium density of the air inside the duct $= 1.21$ kg/m^3, and

c**:** speed of sound for the air inside the duct, at equilibrium $= 343$ m/s.

Vented Enclosure: enclosure with two ports, one for the loudspeaker and another for the duct with the following:

V_{b_0}**:** enclosed volume when the cone and vent are at rest $= 0.17$ m^3,

P_{b_0}**:** equilibrium pressure of the enclosed air $= 1.0133 \times 10^5$ Pa,

Ω_1**:** cross sectional area of the enclosure's opening for the loudspeaker's cone $=$ 0.083 m^2,

Ω_2**:** cross sectional area of the enclosure's opening for the duct $= 0.037$ m^2, and

γ**:** ratio of the specific heat at a constant pressure to the specific heat at a constant volume for air $= 1.4$.

Acoustic Half-Space: linear map from cone and vent motion to p, p_{f}, F_1, and F_2 that addresses the coupling of the acoustic environment to the loudspeaker and duct (modeled as a half-space with two vibrating pistons attached to an infinite baffle), as shown in Figure 5.3 with

ρ_0**:** equilibrium density of the air in the half-space $= 1.21$ kg/m,

c: speed of sound for the air in the half-space, at equilibrium = 343 m/s,

$\dot{z_{2_L}}$: velocity of the air particles on the face of the duct (baffle side),

H_1: the dynamics (with time delays removed) from the cone's velocity to p, p_{f}, F_1, and F_2,

H_2: the dynamics (with time delays removed) from the velocity of the air particles on the face of the duct (baffle side) to p, p_{f}, F_1, and F_2,

$\tilde{H}_2$: the dynamics (with time delays removed) from the acceleration of the air particles on the face of the duct (baffle side) to p, p_{f}, F_1, and F_2,

τ_1: time delay between the cone's velocity and p, computed as the time it takes a pressure wave to traverse the shortest distance between the cone's surface (at rest) and p $\left(\tau_1 = \frac{0.032}{c} = 9.3 \times 10^{-5} \text{ seconds}\right)$,

τ_2: time delay between the cone's velocity and p_{f} ($\tau_2 = \frac{1}{c} = 2.9 \times 10^{-3}$ seconds),

τ_3: time delay between the cone's velocity and F_2 (or between the velocity of the air particles at on the face of the duct (baffle side) and F_1), calculated using the shortest distance between the edge of the cone and that of the vent $\left(\tau_3 = \frac{0.29 - a_1 - a_2}{c} = 5.6 \times 10^{-5} \text{ seconds}\right)$,

τ_4: time delay between the velocity of the air particles on the face of the duct (baffle side) and p $\left(\tau_4 = \frac{\sqrt{0.032^2 + (0.29 - a_2)^2}}{c} = 5.4 \times 10^{-4} \text{ seconds}\right)$, and

τ_5: time delay between the velocity of the air particles on the face of the duct (baffle side) and p_{f} $\left(\tau_5 = \frac{\sqrt{1^2 + (0.29 - 0.15 - a_2)^2}}{c} = 2.9 \times 10^{-3} \text{ seconds}\right)$.

The transfer functions H_1 and H_2 were obtained using the method outlined in Section 2.2. Both were stable, 48^{th}-order LTI systems. Note that even though $\tilde{H}_2$ contains an extra integrator, it is still a 48^{th}-order system. This is because given an n^{th}-order, state-space realization for the dynamics of H_2, with $H_2(0) = 0_4$, the results in Appendix C imply that there exists an n^{th}-order, state-space realization for $\tilde{H}_2$. Both H_1 and $\tilde{H}_2$ can be found in Appendix D.

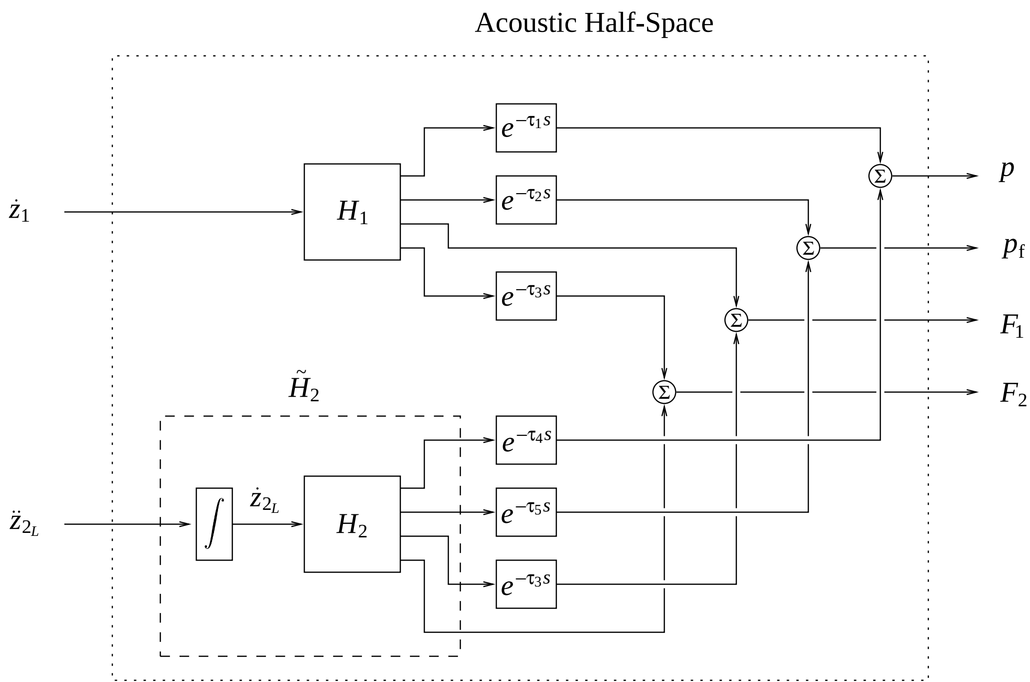

Figure 5.3: The Acoustic Half-Space Model

Even though the response from u to p_{f} is most important, p will be used for evaluation as well as the pressure output signal for feedback and u will be used as the input, while p_{f} will only be used to monitor the performance at its location. This is due to the fact that using p_{f} as the feedback signal will introduce a significant time delay in the feedback loop, making it difficult to design a controller with satisfactory performance.

5.1.1 Model Simulation

In order to measure the distortion in the loudspeaker's outputs, fixed-frequency, large amplitude sine-wave input simulations were performed. The outputs were allowed to reach their steady state, before the distortion values were calculated. Figures 5.4 and 5.5 show the distortion (=: $\mathrm{THD}_{\mathrm{A_o}}$) for p and p_{f}, respectively, at various amplitudes and frequencies. As illustrated, the nonlinear nature of the loudspeaker system is indicated by the presence of substantial distortion, especially at low frequencies.

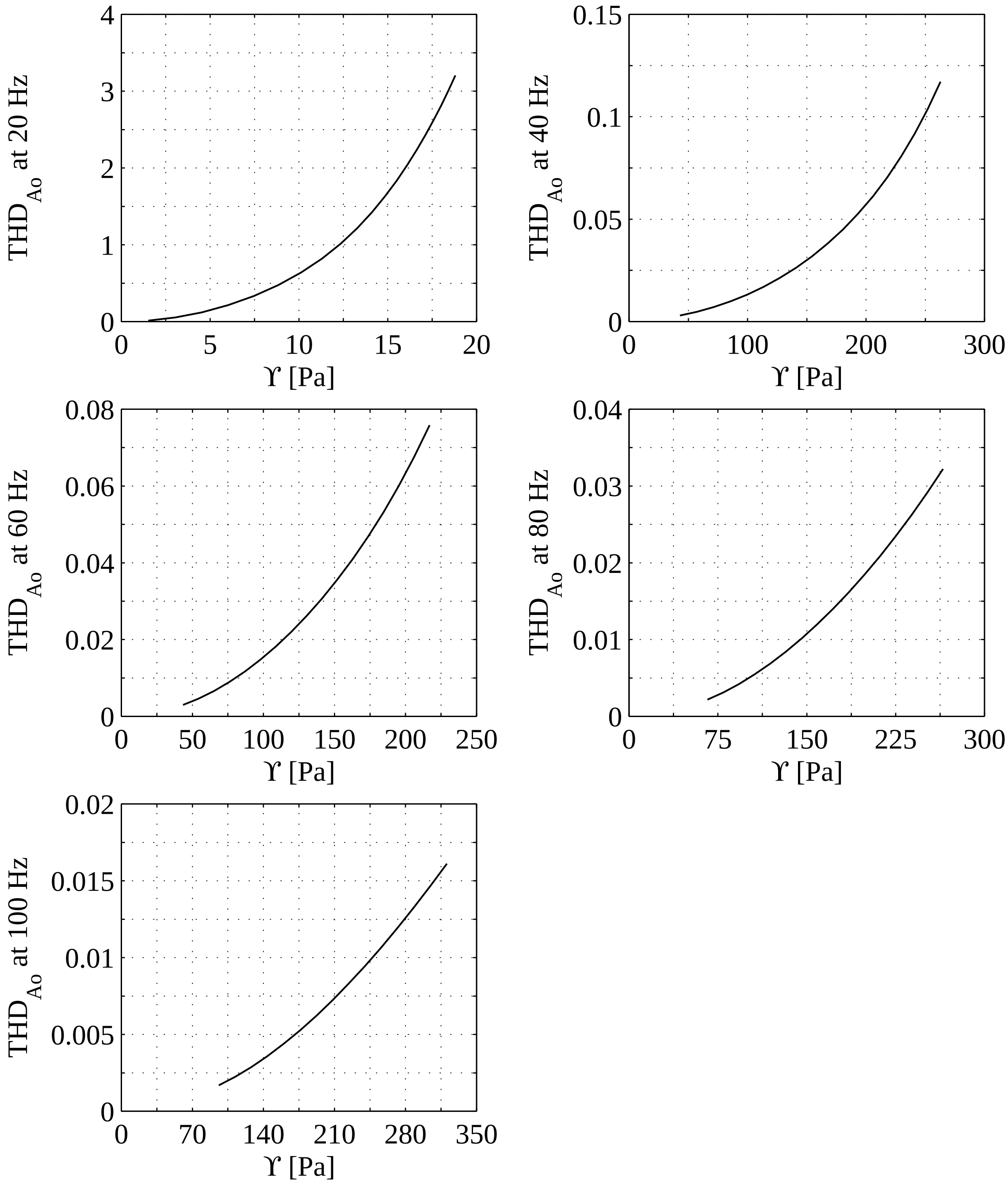

Figure 5.4: The Harmonic Distortion in p for the Vented Loudspeaker Model

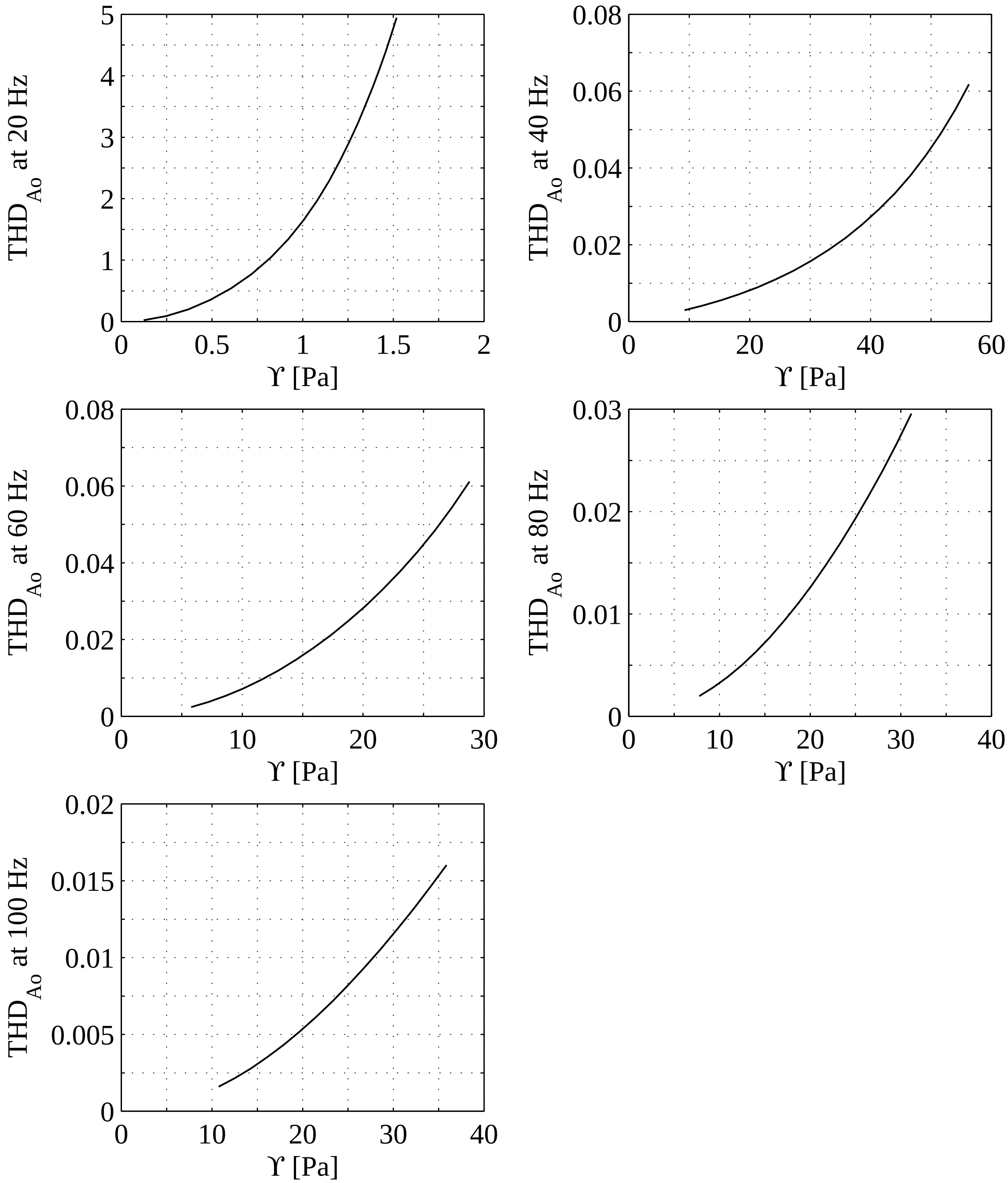

Figure 5.5: The Harmonic Distortion in p_{f} for the Vented Loudspeaker Model

5.1.2 Model Linearization

In order to apply linear control theory and design a μ-controller for the loudspeaker, a linearization (about 0) of the model must be obtained. A linearization of (2.4) can be obtained by setting $Bl_1 \equiv 0$. Hence,

$$Bl(z_1) \approx Bl_0. \tag{5.1}$$

Furthermore, (2.5) can be linearized by setting $k_1 \equiv 0$ and $k_2 \equiv 0$, which gives

$$F_k(z_1) \approx k_0 z_1. \tag{5.2}$$

Also, the enclosure equation (2.28) is linearized by performing a Taylor series expansion about $(z_1, z_{2_0}) = (0,0)$ and considering only the terms up to first-order, i.e. [35]

$$\begin{aligned} p_{\mathrm{b}}\left(z_1, z_{2_0}\right) &\approx p_{\mathrm{b}}(0,0) + \left.\frac{\partial p_{\mathrm{b}}\left(z_1, z_{2_0}\right)}{\partial z_1}\right|_{\left(z_1, z_{2_0}\right)=(0,0)} z_1 + \left.\frac{\partial p_{\mathrm{b}}\left(z_1, z_{2_0}\right)}{\partial z_{2_0}}\right|_{\left(z_1, z_{2_0}\right)=(0,0)} z_{2_0} \\ &= \frac{-\gamma P_{\mathrm{b}_0}}{V_{\mathrm{b}_0}}\left(\Omega_1 z_1 + \Omega_2 z_{2_0}\right). \end{aligned} \tag{5.3}$$

Substituting into (2.7) and (2.8) yields the linearized loudspeaker equations

$$\frac{d^2 z_1}{dt^2} \approx \frac{1}{m}\left[Bl_0 i - k_0 z_1 - R_m \frac{dz_1}{dt} - \frac{\gamma P_{\mathrm{b}_0}\Omega_1}{V_{\mathrm{b}_0}}\left(\Omega_1 z_1 + \Omega_2 z_{2_0}\right) - F_1\right], \tag{5.4}$$

$$\frac{di}{dt} \approx \frac{1}{L_{\mathrm{e}}}\left[u - R_{\mathrm{e}} i - Bl_0 \frac{dz_1}{dt}\right]. \tag{5.5}$$

In addition, the pure time delays contained in the half-space map were replaced with their respective, 1^{st}-order *Padé* approximations, i.e. the 1^{st}-order approximation for a τ second delay [22]

$$e^{-\tau s} \approx \frac{1 - \tau s/2}{1 + \tau s/2}. \tag{5.6}$$

Once the linearized equations and time-delay approximations were utilized in the interconnection shown in Figure 5.2 (along with the equations that were already linear, i.e. the equations for the duct and acoustic half-space), the frequency response of the system's linearization was computed, as illustrated in Figure 5.6.

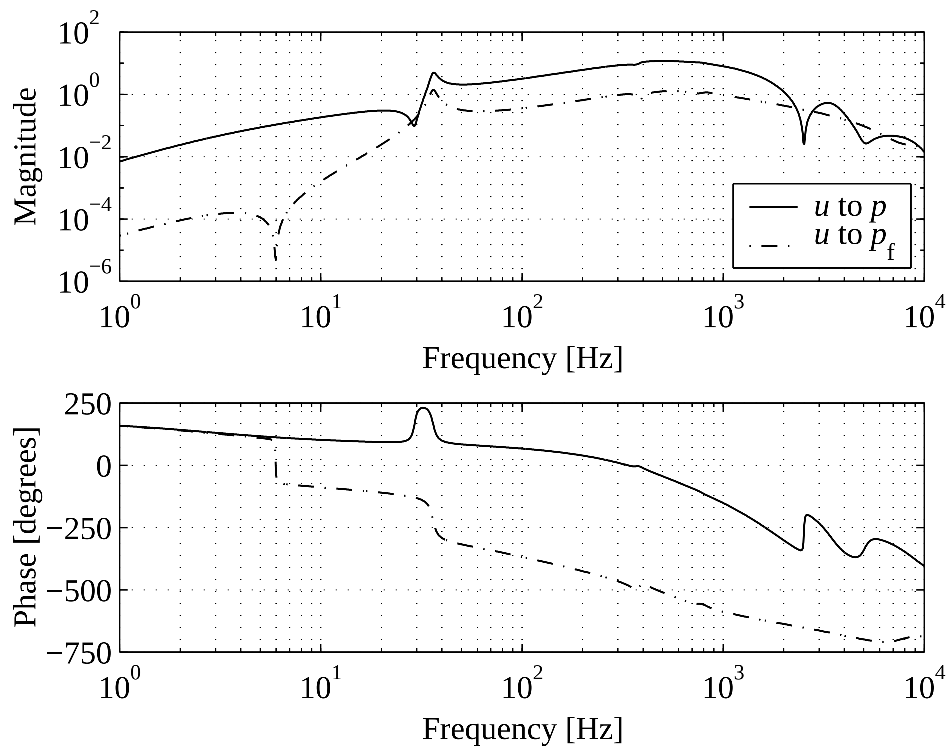

Figure 5.6: The Vented Loudspeaker Model's Frequency Response

Next, a 12$^{\text{th}}$-order, Single Input, Single Output (SISO) frequency domain fit (=: G_{nom}) was obtained for the linearized map from u to p using a frequency-domain, weighted least-squares algorithm and its frequency response is shown in Figure 5.7. The plot shows a good fit throughout the frequency region between 1 Hz and 10 kHz. Also, the plant dynamics exhibit non-minimum phase zeros at 0.41, 22750, 5359$\pm$70624j, and 76359 rad/s, which may limit the allowable performance bandwidth of the closed-loop system. Note that only the response from u to p was fit, since it is the transfer function required for the control design (recall that the transfer function from u to p_{f} is just used for monitoring the loudspeaker's performance at the 1 meter location).

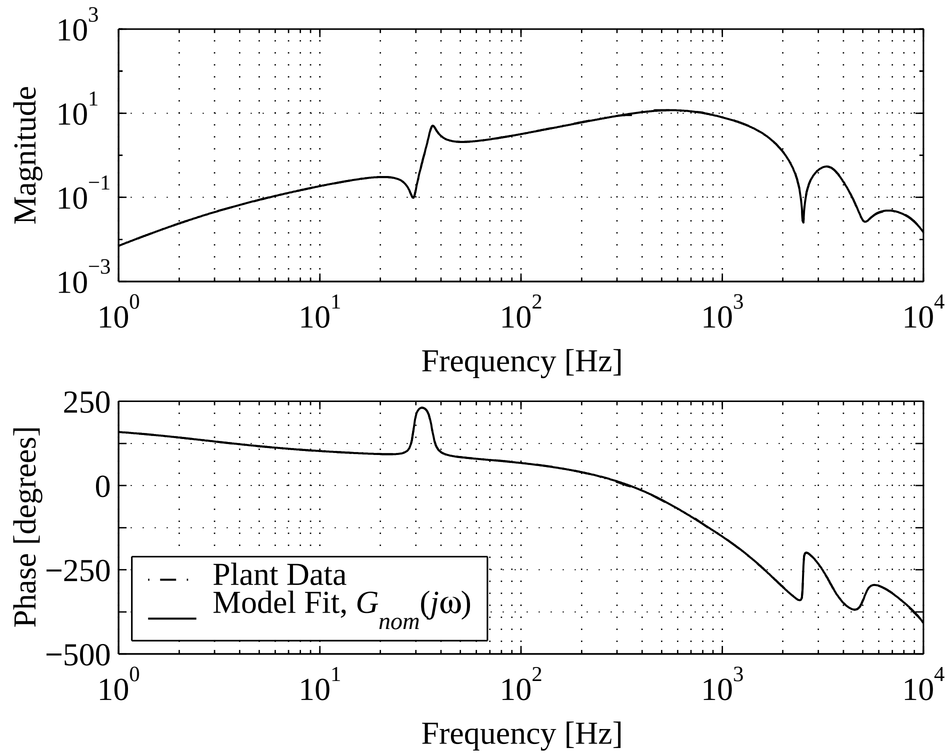

Figure 5.7: The Vented Loudspeaker Model's Nominal Frequency-Domain Fit G_{nom}

5.1.3 Control Design: Uncertainty and Performance Objective Weights

Using the fit G_{nom}, a controller can be designed using the methods of Chapter 4. Once a controller is designed, it is implemented as shown in Figure 4.1. In this example, the amplifier and microphones are replaced with unity gain blocks, i.e. the dynamics of the plant G are entirely due to the vented loudspeaker model.

As described in Section 4.2.2, frequency-domain weights applied to the interconnection shown in Figure 4.5 have to be chosen to properly reflect the control objectives. The following weights (with frequency responses shown in Figure 5.8) have been carefully designed to extract the most performance out of the closed-loop interconnection:

Uncertainty Weight: The uncertainty weight, W_Δ was chosen to be a 5^{th}-order, stable transfer function. Reaching a minimum in magnitude of approximately 0.30 at 128 Hz, the closed loop system was required to be impervious to at least a 30% variation in G over all frequencies, up to 18000% at low frequencies, and up to 13000% at high frequencies.

Performance Weight: The magnitude of W_{err} (4^{th}-order, stable transfer function) was chosen to be larger than unity in the region between 26 Hz and 246 Hz. This penalizes the magnitude of the sensitivity function S so that it will be smaller than unity in that region. Furthermore, the weight was designed such that the bandwidth limit set by the non-minimum phase zeros was not exceeded, while minimizing (yet allowing for) the unavoidable peaks above unity in the magnitude response of S outside the performance bandwidth.

Reference Signal Weight: Since the control goal involves tracking d_{ref}, $W_{ref} := 1$.

Noise Weight The stable, 3^{rd}-order W_{knoise} was treated as the upper bound for the noise present in y.

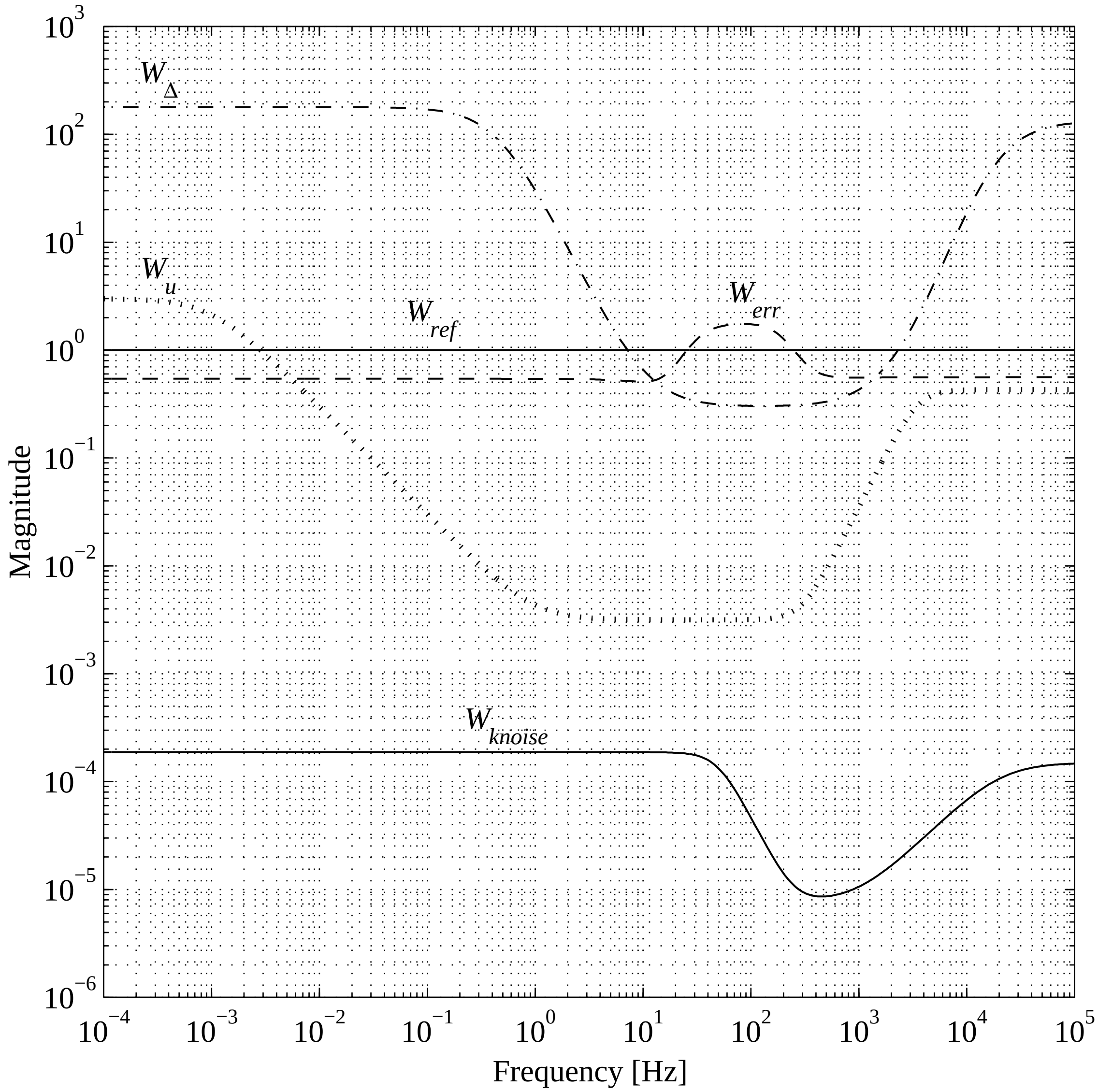

Figure 5.8: The Vented Loudspeaker Model's Uncertainty and Performance Weights

Control Signal Weight: The control signal was required to have an upper bound to prevent unreasonably large signals from being injected into the loudspeaker model, with a higher penalty being assessed at low-frequencies. As a result, the 3rd-order, stable W_u was formulated such that the magnitude of W_u^{-1} was the upper limit of the amplitude of the control signal u when $d_{ref} = 1$. Moreover, by limiting the control action at high frequencies, this weight further assisted in high-frequency noise rejection and response shaping.

5.1.4 Control Design: D-K Iteration

The weights discussed above were substituted into the interconnection structure displayed in Figure 4.5 and the open-loop interconnection shown in Figure 4.6 was generated. Note that since the frequency response of G_{nom} had a magnitude peak of 11.8, $\alpha := \frac{1}{11.8} = 0.085$. The resulting P was a stable 4×4, 27th-order transfer function and the robust performance perturbation structure was described by

$$\mathbf{\Delta} := \left\{ \mathrm{diag}\left(\Delta, \Delta_p\right) : \Delta \in \mathbb{C}^{1\times 1}, \Delta_p \in \mathbb{C}^{2\times 2} \right\}. \tag{5.7}$$

Implementing the D-K iteration scheme on the interconnection yielded a stable, 45th-order controller K, satisfying the μ-objective after six iterations. Since the order of K was relatively high, a balanced truncation (to 13th-order) was performed on K. Furthermore, the controller's zero at -2.23×10^{-3} rad/s was approximated with a zero at the origin of the complex plane and a zero at -4.79×10^{6} rad/s was replaced with a zero at ∞ and an appropriate gain. Figure 5.9 shows the upper bounds for μ for both the μ-synthesized ($=: K$) and simplified ($=: K_{trunc}$) controllers, with peaks at 0.85 and 0.98, respectively. Figure 5.10 illustrates the resulting controller which was implemented in the system displayed in Figure 4.1. Its frequency response is shown in Figure 5.11.

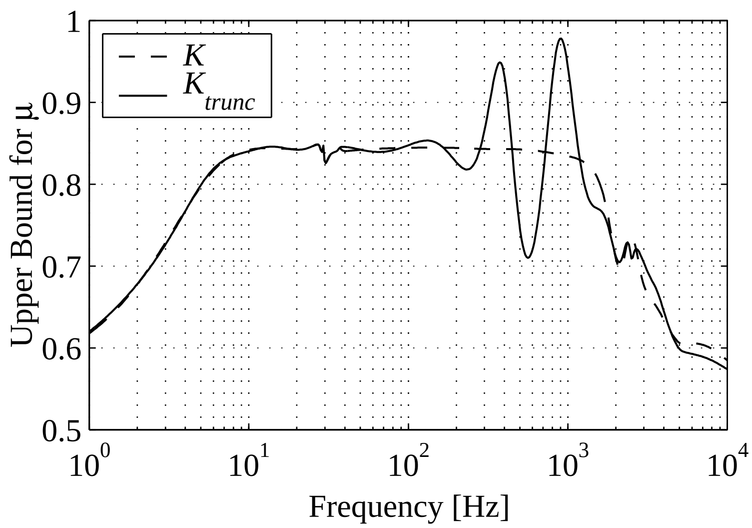

Figure 5.9: The μ Upper-Bounds for the Vented Loudspeaker Model

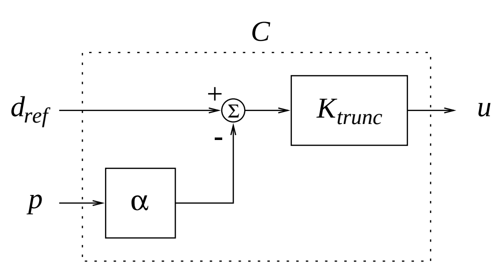

Figure 5.10: The Implemented Controller C for the Vented Loudspeaker Model

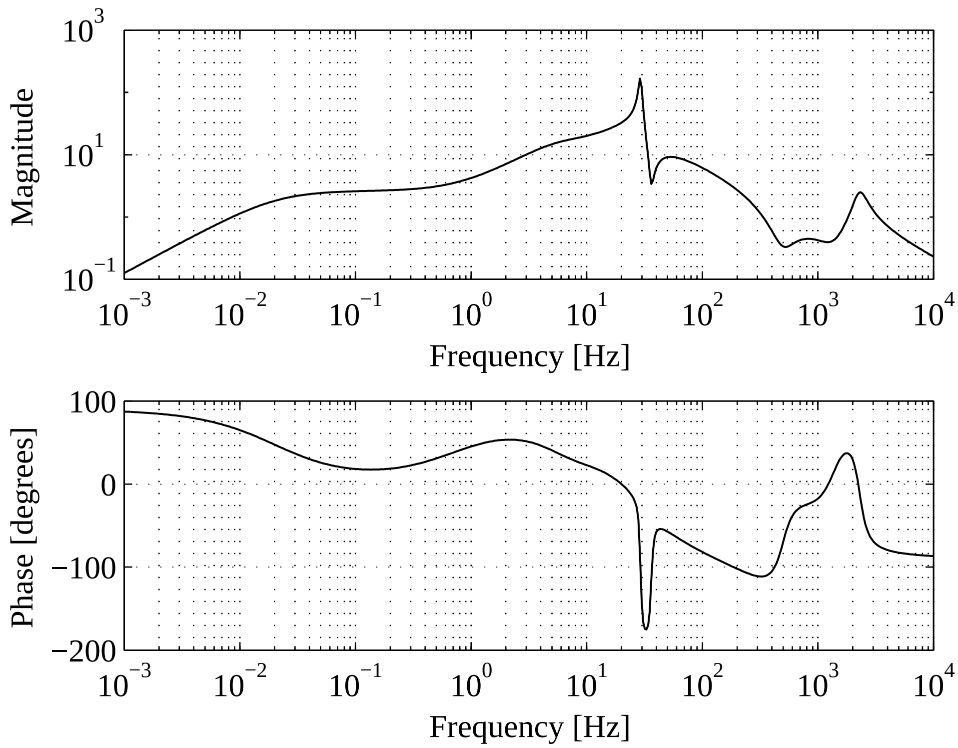

Figure 5.11: Frequency Response of the Vented Loudspeaker Model's Controller K_{trunc}

5.1.5 Results

Using K_{trunc} as the controller, Figures 5.12 and 5.13 show the frequency responses of the open-loop gain $\alpha G K_{trunc}$ and the closed-loop sensitivity function S, respectively. The closed-loop frequency responses of the loudspeaker model's linearization

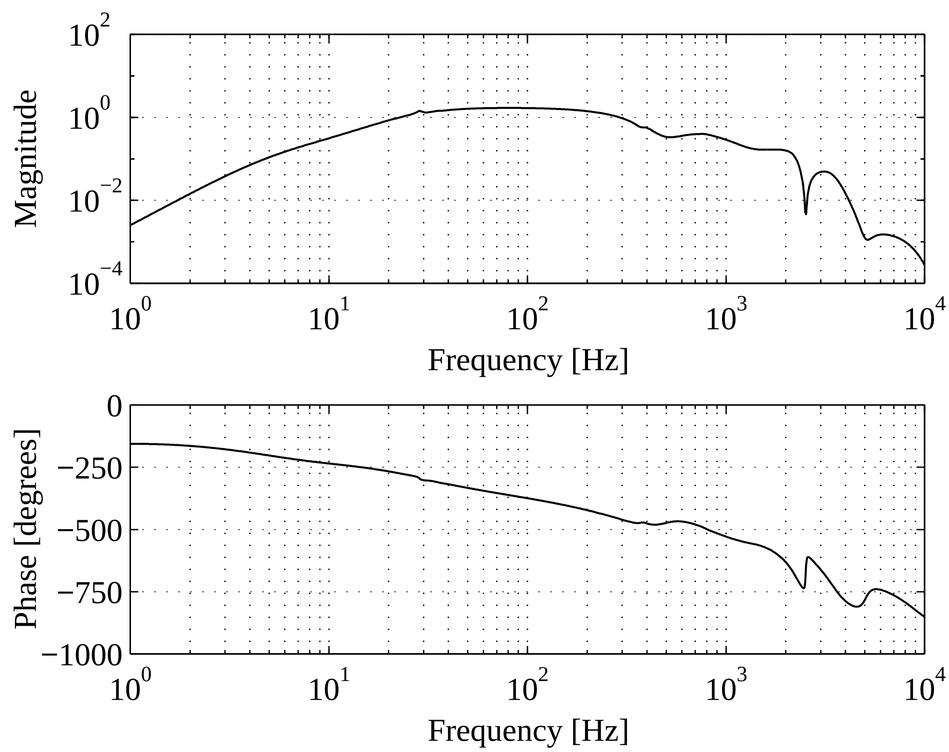

Figure 5.12: The Open-Loop Gain $\alpha G K_{trunc}$ for the Vented Loudspeaker Model

are shown in Figure 5.14 and Figure 5.15 for p and p_{f}, respectively, along with the responses for the uncontrolled case. By repeating the loudspeaker model's simulations, Figures 5.16 and 5.17 show the distortion in p and p_{f}, respectively, at various amplitudes and frequencies before control (=: $\mathrm{THD}_{\mathrm{A_o}}$) and after control (=: $\mathrm{THD}_{\mathrm{A_c}}$). Furthermore, the figures show the plots of $\mathrm{THD}_{\mathrm{A_{cp}}}$ (defined in (3.55)) for comparison.

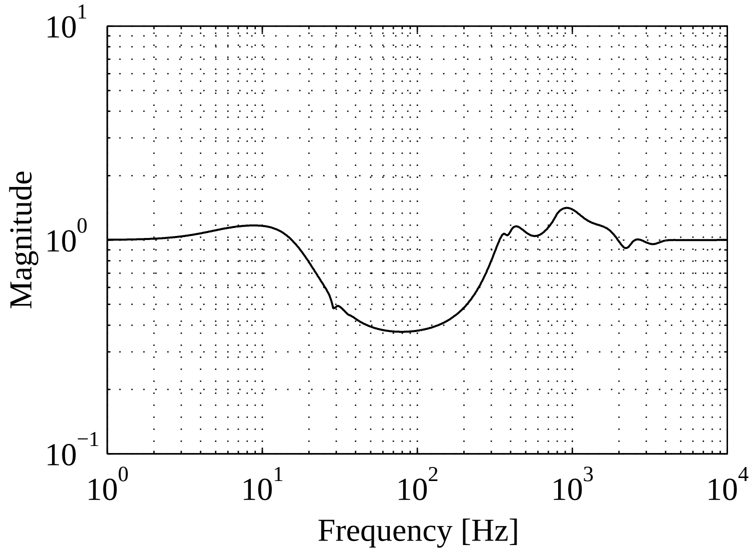

Figure 5.13: The Sensitivity Function S for the Vented Loudspeaker Model

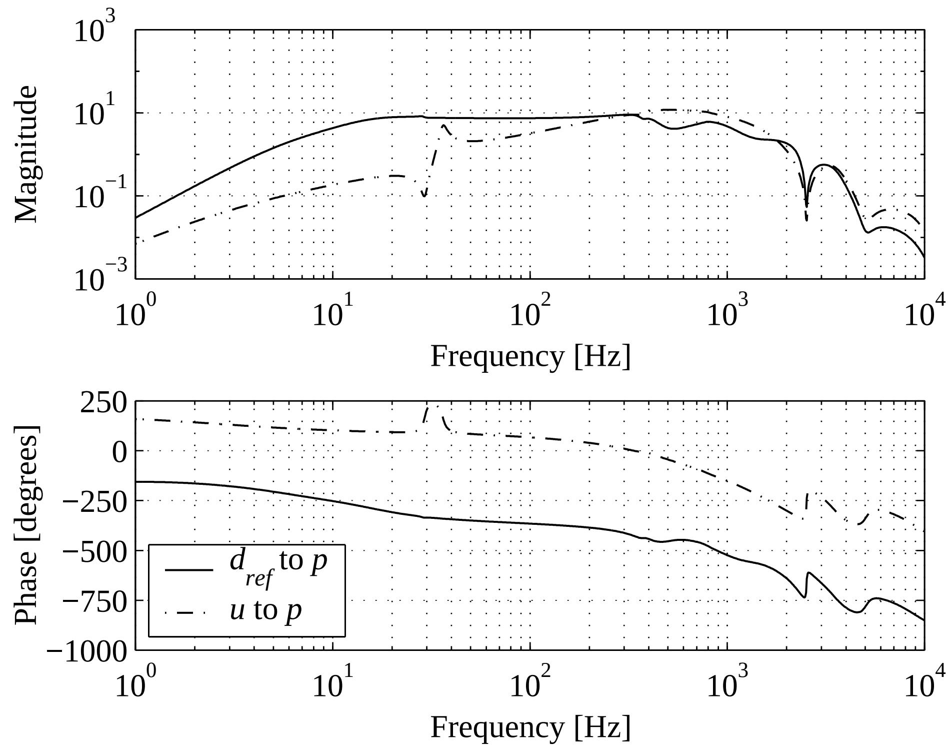

Figure 5.14: The Closed-Loop Frequency Response of p for the Vented Loudspeaker Model

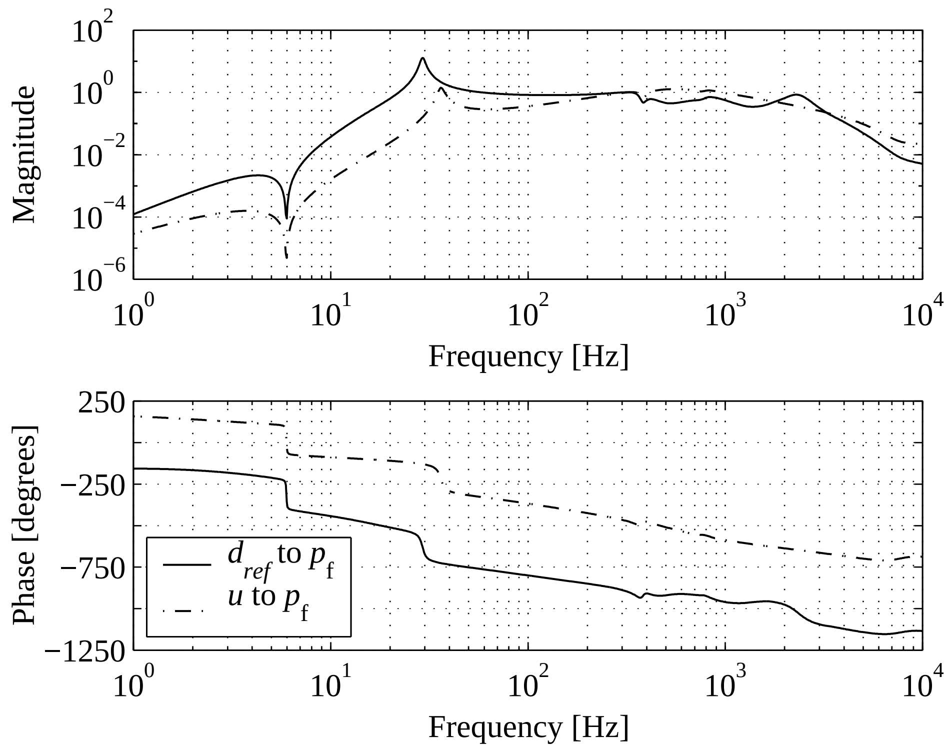

Figure 5.15: The Closed-Loop Frequency Response of p_{f} for the Vented Loudspeaker Model

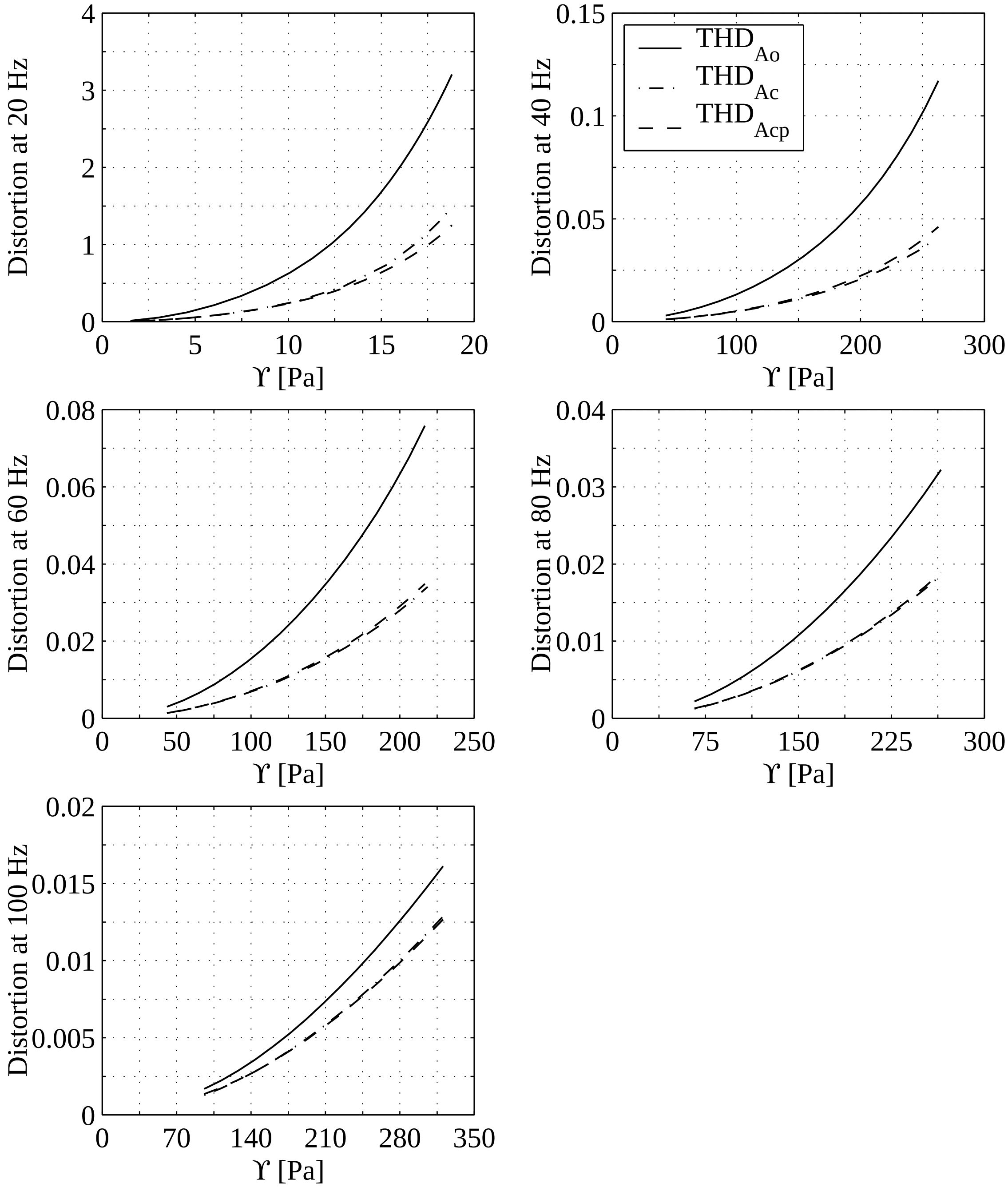

Figure 5.16: The Closed-Loop Distortion in p for the Vented Loudspeaker Model

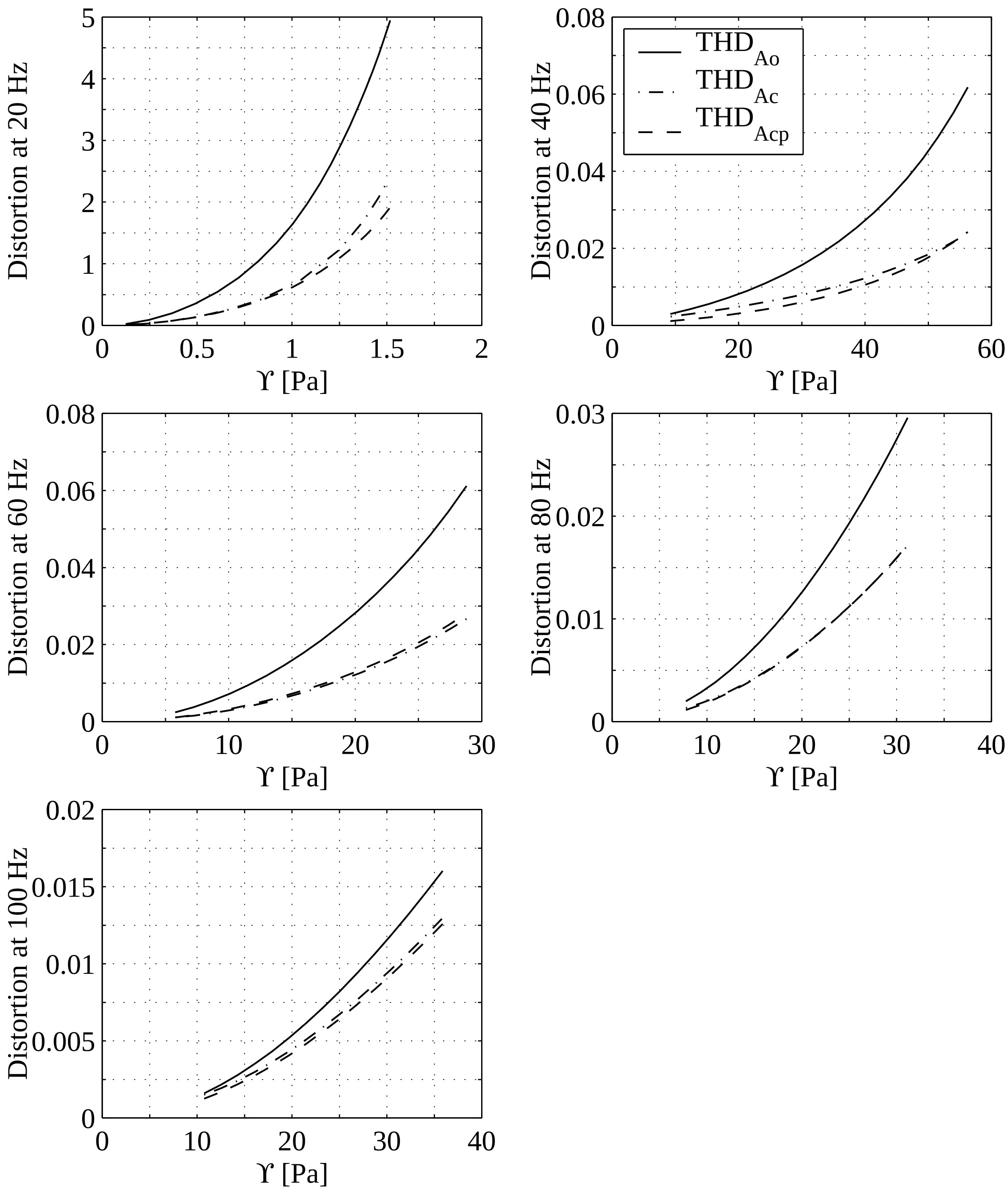

Figure 5.17: The Closed-Loop Distortion in p_{f} for the Vented Loudspeaker Model

The transient behavior of the loudspeaker was investigated using sine-wave inputs at 20 Hz, as shown in Figure 5.18. These inputs started at $t = 0.05$ seconds and stopped at $t = 1.05$ seconds, completing 20 cycles. The input to the uncontrolled loudspeaker system was u and that of the controlled case was d_{ref}. The amplitudes of the inputs were chosen so that the amplitude of the fundamental component in p (in the steady state) for both the controlled and uncontrolled cases remained the same ($\Upsilon = 7.5$ Pa for the steady-state of p, for both cases). They were also chosen so that the nonlinearities of the loudspeaker system were sufficiently excited. Figures 5.19 and 5.20 show the resulting transient responses of p and p_{f}, respectively, for the uncontrolled and controlled systems.

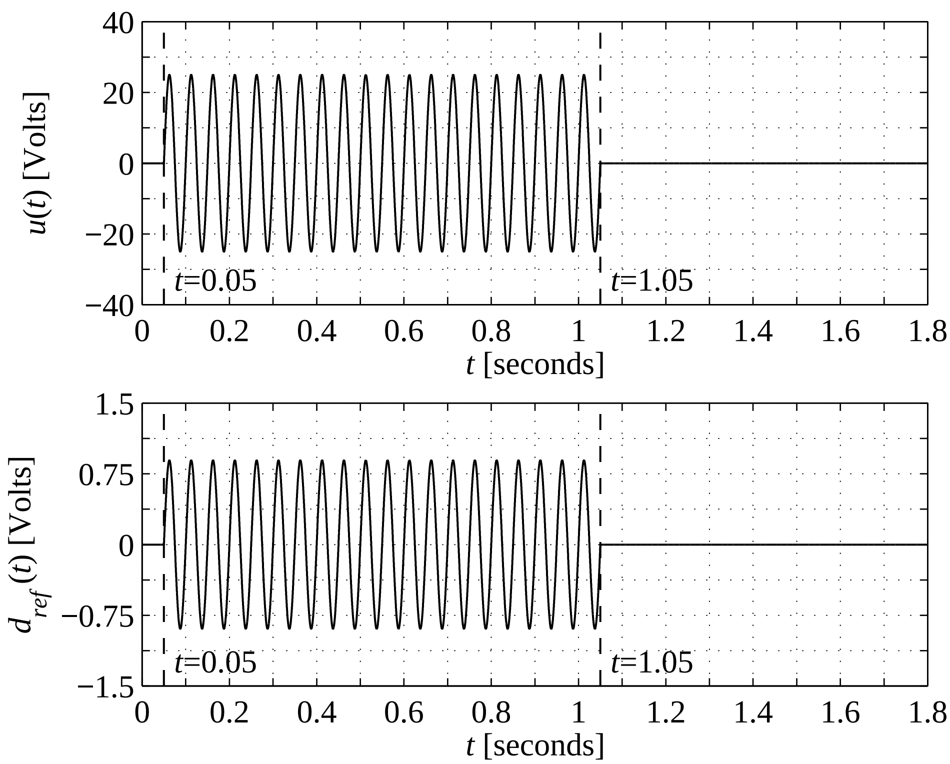

Figure 5.18: The 20 Hz Inputs Used for the Transient Response Test of the Vented Loudspeaker Model ($u(t)$ for the Uncontrolled Case and and $d_{ref}(t)$ for the Controlled System)

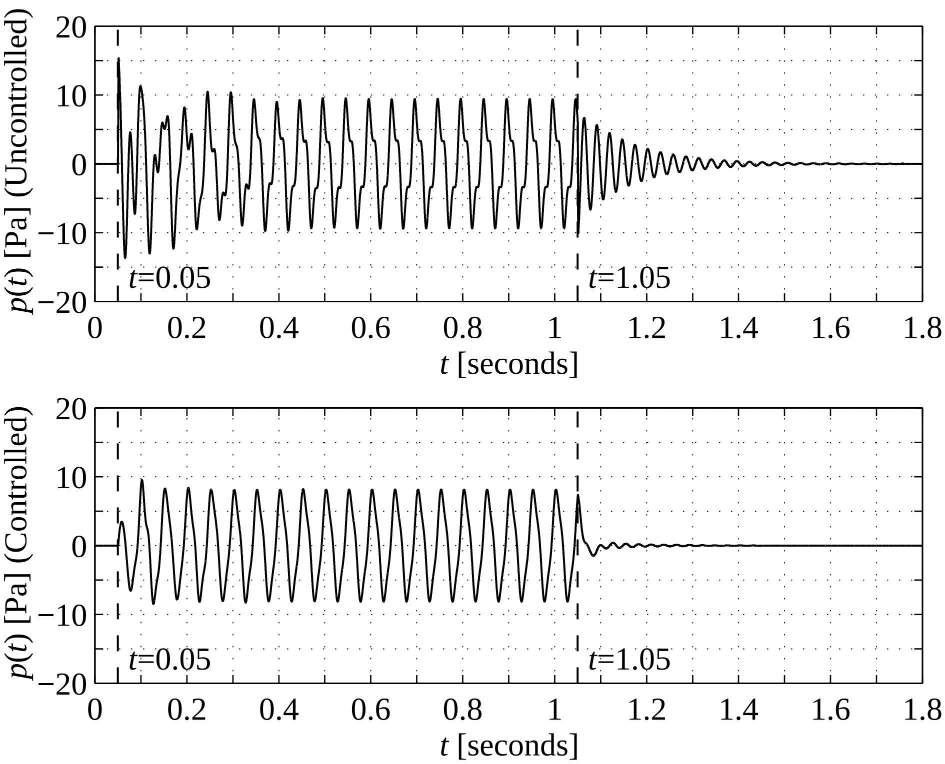

Figure 5.19: The Transient Response of $p(t)$ for the Loudspeaker Model

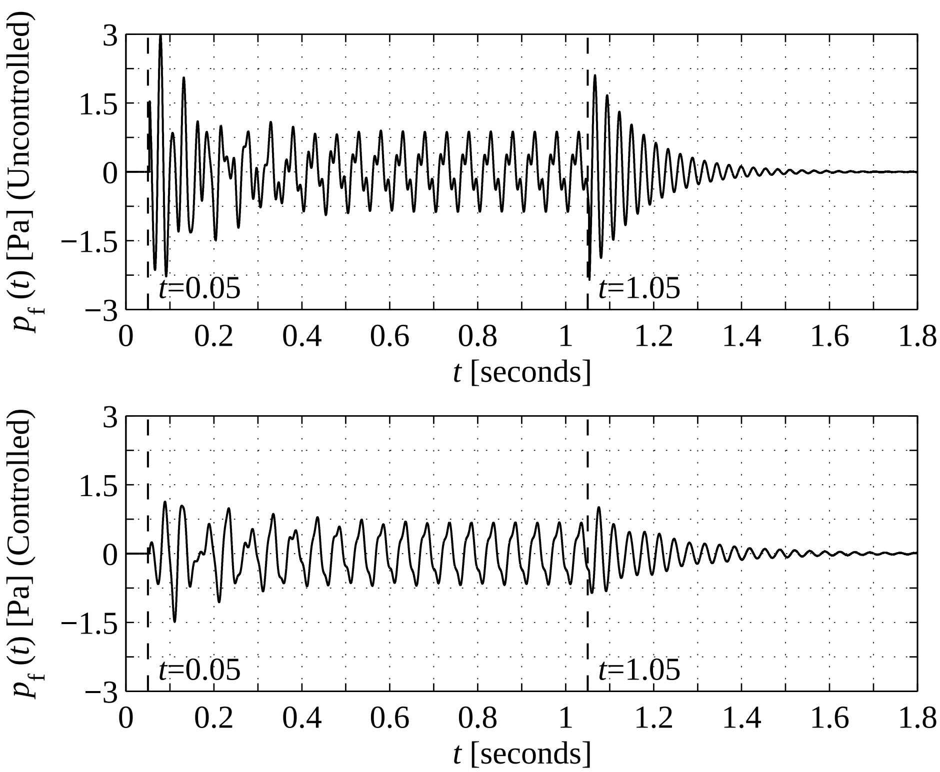

Figure 5.20: The Transient Response of $p_{\mathrm{f}}(t)$ for the Loudspeaker Model

5.1.6 Discussion

Using a μ-designed controller to control the vented loudspeaker model in the low-frequency region, the control objective of improving the model's pressure response in two locations was achieved. Figure 5.13 shows the closed-loop sensitivity function. Note that its magnitude is less than unity from 16 Hz to 336 Hz, while reaching a minimum of 0.37 at 79 Hz. The magnitude response of S, however, contained peaks of 1.17 at 8.7 Hz and 1.41 at 918 Hz, which were unavoidable (as explained in Chapter 4), yet not too large. In light of the findings of Chapter 3, measurable distortion reduction was predicted for the range where the magnitude of S was small.

Harmonic distortion tests were performed to verify the reduction in nonlinear distortion. Figure 5.16 shows large reductions for the harmonic distortion in p, for the controlled case. Note that, even though the distortion reduction relationship (3.55) holds true only for small distortion values, the upper-bound for the predicted distortion with feedback control $\mathrm{THD}_{\mathrm{A_{cp}}}$ nearly overlaps the closed-loop distortion $\mathrm{THD}_{\mathrm{A_c}}$, even for large values. This shows that (3.55) is a good approximation for this model. The distortion reduction was most significant when the loudspeaker was driven at lower frequencies, where the ratio $\frac{\mathrm{THD}_{\mathrm{A_c}}}{\mathrm{THD}_{\mathrm{A_o}}}$ reached a low of 0.38 (for the 20 Hz case). When driven at 100 Hz, the reduction was minimal $\left(\frac{\mathrm{THD}_{\mathrm{A_c}}}{\mathrm{THD}_{\mathrm{A_o}}} = 0.81\right)$. This comes as no surprise, since the controller was designed to increase the performance at low frequencies. Also, Figure 5.17 shows similar reductions for the distortion in p_{f}, even though the signal p_{f} was not part of the performance objective. As a matter of fact, $\mathrm{THD}_{\mathrm{A_{cp}}}$ shows reasonable agreement with $\mathrm{THD}_{\mathrm{A_c}}$. Therefore, reducing the distortion in p also reduces the distortion in p_{f} by a comparable amount, in this example.

To analyze the transient behavior of the loudspeaker system, Figure 5.18 shows special sine-wave inputs that were designed with amplitudes that significantly excited the nonlinearities in the loudspeaker system. As Figures 5.19 and 5.20 illustrate, the improvement in the transient response of the loudspeaker due to the control scheme is evinced by the quicker decay and smaller transient overshoots for both p and p_f. Moreover, no additional delays were added to the pressure responses due to the control method.

5.2 Real Loudspeaker in a Vented Enclosure

Even though the example with the loudspeaker model clearly illustrated the validity of the control approach, it was of practical interest to test this method on an actual loudspeaker.

Figure 5.21 shows a schematic of a typical loudspeaker in a vented enclosure (with two cylindrical ducts, in this case) including two pressure measuring microphones.

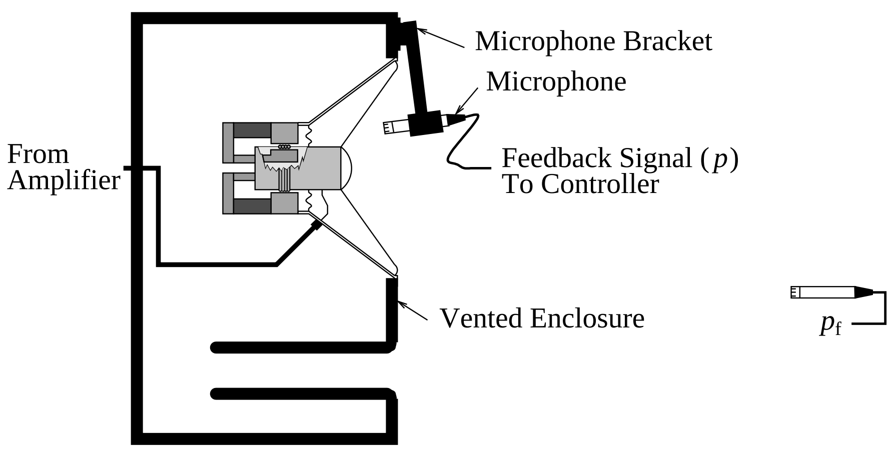

Figure 5.21: The Vented-Box Loudspeaker

Since the enclosure is assumed to be rigid, the acoustic radiation emanates entirely from the cone and vents. One microphone mounted 0.028 meters (1.1 inch) away from the cone (at rest) measures the pressure p for feedback use. The other microphone located 1 meter away from the cone's surface and 0.1 meters below the cone's centerline measures p_f.

5.2.1 Plant Identification

In order to analyze the full extent of the loudspeaker's output, two types of experiments were carried out: broadband, small amplitude sine-sweeps to measure the nominal frequency response (linear), and fixed-frequency large amplitude, steady-state sine-wave tests to measure the harmonic distortion (nonlinear). Note that since the loudspeaker system is mildly nonlinear, rather than having to compute the linearization of the loudspeaker, its linear response can be measured through small-signal experiments. For consistency and convenience, the experiments were performed in an anechoic chamber. Figure 5.22 shows the nominal frequency response measurements for the vented-box loudspeaker system, from the voltage into the amplifier ($=: u$) to the voltages from the microphones that measure p and p_{f}. Also, Figure 5.23 shows the measured distortion ($=: \mathrm{THD}_{\mathrm{A_o}}$) at various frequencies and amplitudes for both p and p_{f}. Root Mean Square (RMS) averaging and uniform windowing techniques were used.

The plant consisted of a 15 inches in diameter, professional grade loudspeaker fitted to a 6 ft^3 enclosure having two ducts. The plant also included a voltage-drive amplifier of similar quality, capable of producing 1000 Watts RMS of continuous power. Two low-noise, high quality microphones, used to measure the pressures produced by the loudspeaker system (p and p_{f}), were also parts of the plant. The microphone that measures p was used for feedback control, as well as for evaluating the pressure response. On the other hand, the one that measures p_{f} will only be used to monitor the performance at its location. Therefore, only the frequency response from u (the voltage into the amplifier) to p will be fit with an LTI system. The plant data were obtained from vector-averaged, 512-point Fast-Fourier Transforms (FFT) of the pressure signal measurements (uniform window) and a sine-sweep input using a **HP35660A Dynamic Signal Analyzer**. The input signal amplitude was kept small for the broadband tests so that the distortion was as low as possible.

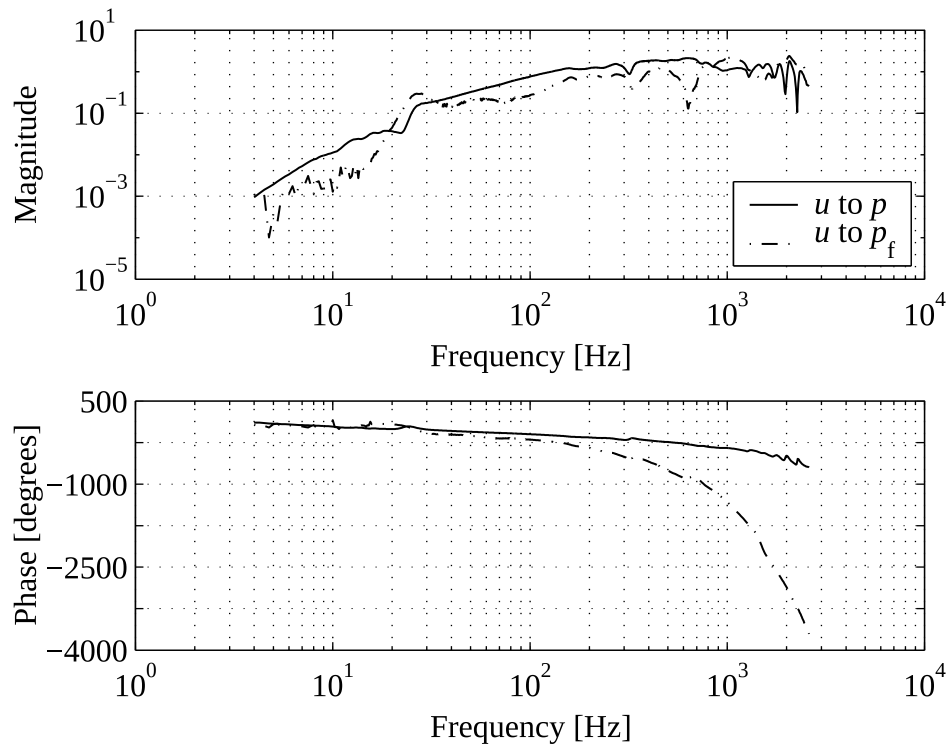

Figure 5.22: The Measured Small-Signal Frequency Response for the Vented-Box Loudspeaker System

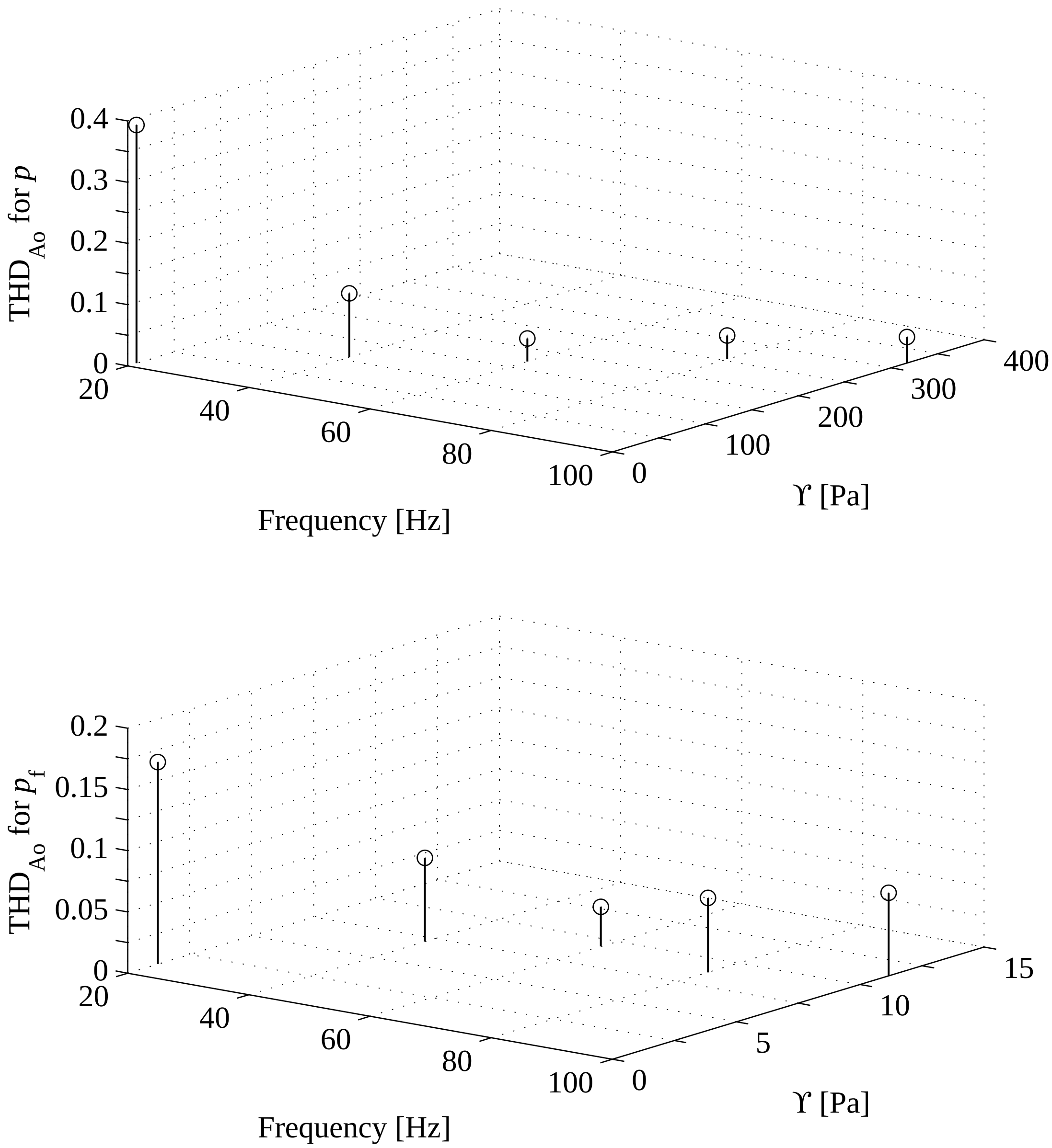

Figure 5.23: The Measured Distortion for the Vented Loudspeaker System (p at 0.028 meters and p_{f} at 1 meter)

The SISO linear model fit G_{nom} (the transfer function from u to p) shown in Figure 5.24 was obtained using a 14$^{\text{th}}$-order, frequency-domain, weighted least-squares algorithm. The plot shows a good fit in the region between 4 Hz and 1 kHz. Also, the plant dynamics exhibited non-minimum phase zeros at $6.89 \pm 8.56j$, 7254, $4585 \pm 2233j$, and $2242 \pm 34025j$ rad/s.

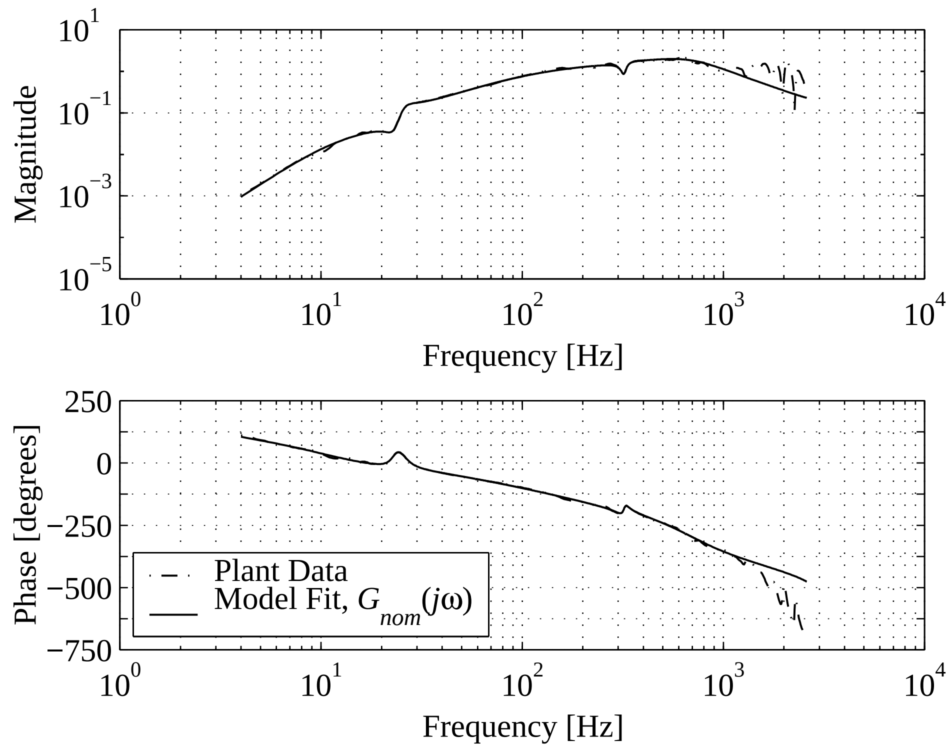

Figure 5.24: The Vented Loudspeaker System's Nominal Model Fit G_{nom}

5.2.2 Control Design: Uncertainty and Performance Objective Weights

Once G_{nom} is found, a controller can be synthesized utilizing the techniques of Chapter 4 and is implemented as shown in Figure 4.1.

Following the outline in Section 4.2.2, frequency-domain weights (Figure 5.25

shows their frequency responses) applied to the interconnection shown in Figure 4.5 were carefully designed to properly reflect the control objectives. These weights are:

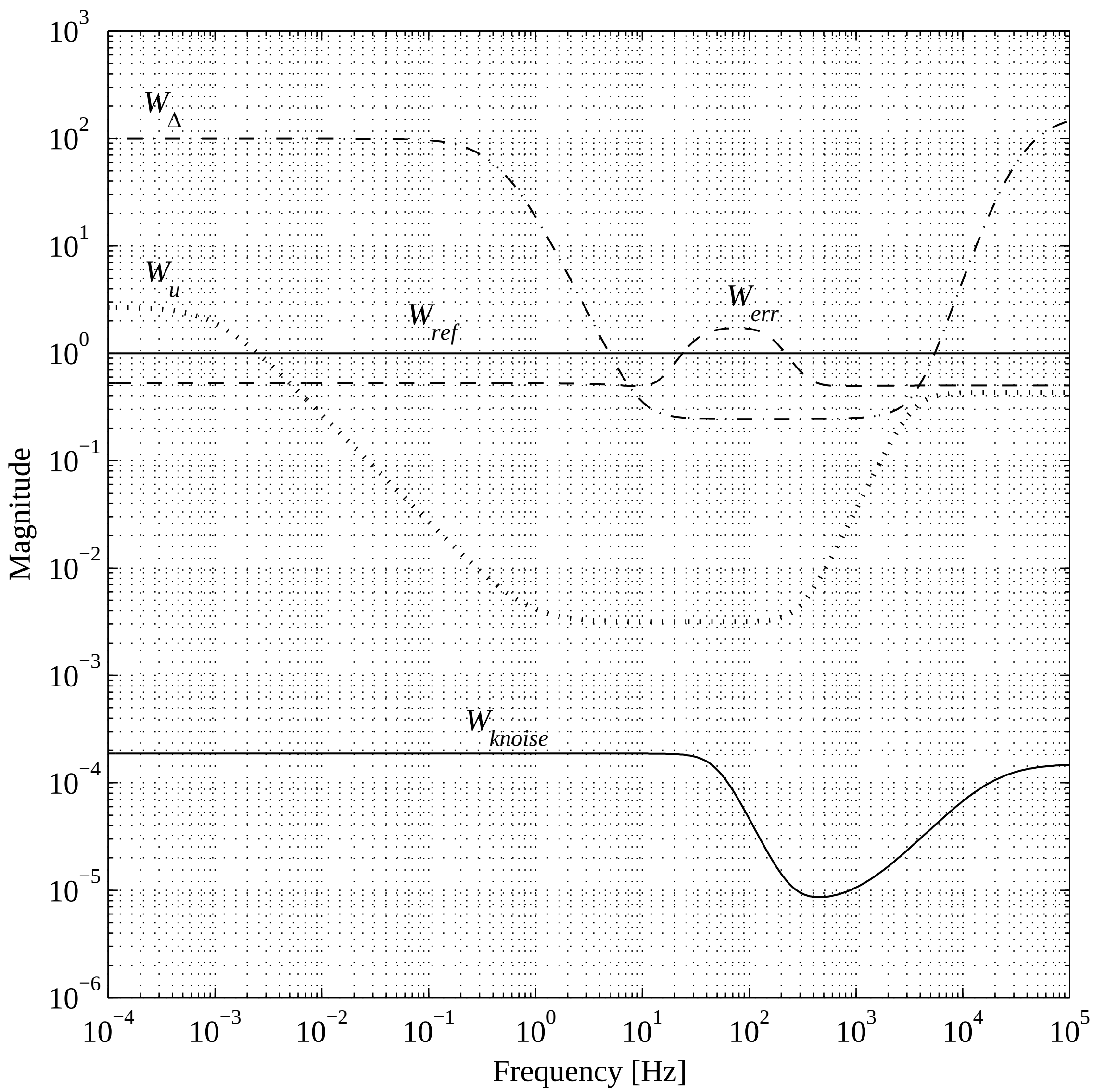

Figure 5.25: The Vented Loudspeaker System's Uncertainty and Performance Weights

Uncertainty Weight: W_{Δ} was chosen to be a 5^{th}-order, stable transfer function. With its magnitude reaching a minimum of approximately 0.24 at 147 Hz, the closed-loop system is required to be impervious to at least a 24% variation in

G over all frequencies, up to 10000% at low frequencies, and up to 17000% at high frequencies.

Performance Weight: The magnitude of W_{err} (4^{th}-order, stable transfer function) was chosen to be larger than unity in the region between 24 Hz and 218 Hz, in order to penalize the magnitude of S such that it will be smaller than unity in that region. In addition, the weight was designed with provisions for the limitations set by the non-minimum phase zeros, while minimizing the unavoidable peaks above unity in the magnitude response of S that fall outside the performance bandwidth.

Reference Signal Weight: $W_{ref} := 1$.

Noise Weight The stable, 3^{rd}-order W_{knoise} penalizes the noise present in y.

Control Signal Weight: The 3^{rd}-order, stable W_u penalizes the control signal so as to prevent potentially damaging signals from being introduced into the loudspeaker, especially at low-frequencies. Moreover, the penalty is large at high frequencies to assist in high-frequency noise rejection and response shaping.

Since the control objectives and plant dynamics are similar to that of the loudspeaker model example, the weights from the vented loudspeaker model example (Figure 5.8) closely resemble these weights, which comes as no surprise.

5.2.3 Control Design: D-K Iteration

Substituting the weights into the interconnection structure illustrated in Figure 4.5, the open-loop interconnection P shown in Figure 4.6 was generated. Note that the frequency response of G_{nom} had a magnitude peak of 2, in this case. So, $\alpha := \frac{1}{2} = 0.50$. For this example, P is a stable 4×4, 29^{th}-order transfer function with a robust performance perturbation structure described by (5.7).

Applying the D-K iteration algorithm to the interconnection produced a stable, 55^{th}-order controller K, which satisfied the μ-objective with an upper-bound peak of 0.84. Further balanced truncation and simplification yielded a 7^{th}-order controller K_{imp}, suitable for implementation, with an upper bound for μ peaking at 0.99. Figure 5.26 shows the upper bound for μ for the various controllers. The resulting controller

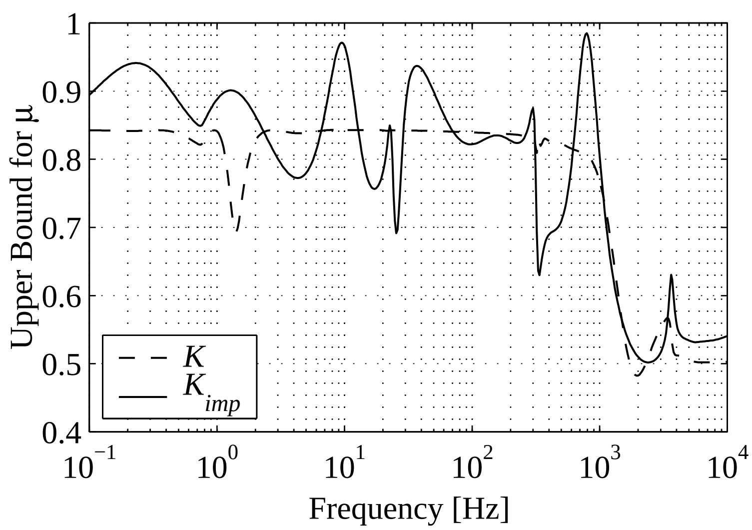

Figure 5.26: The μ Upper-Bounds for Various Controllers of the Vented Loudspeaker System

is shown in Figure 5.27 and was implemented in the system illustrated in Figure 4.1.

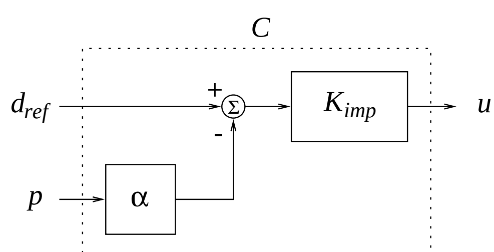

Figure 5.27: The Implemented Controller C for the Vented Loudspeaker System

5.2.4 Control Design: Hardware Implementation

The controller C (shown in Figure 5.27) was implemented both as a digital and an analog system. A Digital Signal Processor (DSP) board (manufactured by **Spectrum**) containing a **Texas Instruments TMS320C30** floating point processor, 16 bit A/D and D/A converters, and 2$^{\text{nd}}$-order, anti-aliasing filters (roll off at 20 kHz) was used to test the design before a permanent analog filter was fabricated. Since the DSP implemented discrete-time systems, the formulated controller was converted into the discrete-time domain by means of a bilinear transformation at a sampling time of 5×10^{-5} seconds, i.e., the transformation from the s-plane to the z-plane is given by [42]

$$s = \frac{2}{T}\frac{1 - z^{-1}}{1 + z^{-1}}, \tag{5.8}$$

where T is the sampling time. Because the sampling rate ($:= \frac{1}{T}$) was 200 times higher than the upper operating frequency limit of the loudspeaker (100 Hz), the discretized controller was treated as an approximation to the continuous-time controller, C. Since the relatively high cost of high-performance DSP hardware would currently prohibit the widespread use of this control system in loudspeakers, the DSP application was used primarily for rapid prototyping of the designed controller. As a result, C was finally implemented as an analog circuit.

5.2.5 Results

The control designs were implemented in hardware and the predicted loudspeaker performance improvements were verified. In Figure 5.28, both the predicted and measured responses of K_{imp} (the analog application controller) were plotted. Figure 5.29 shows both the measured and the model's open-loop gains ($=: \alpha G K_{imp}$), whereas Figure 5.30 plots the measured and the model's sensitivity functions.

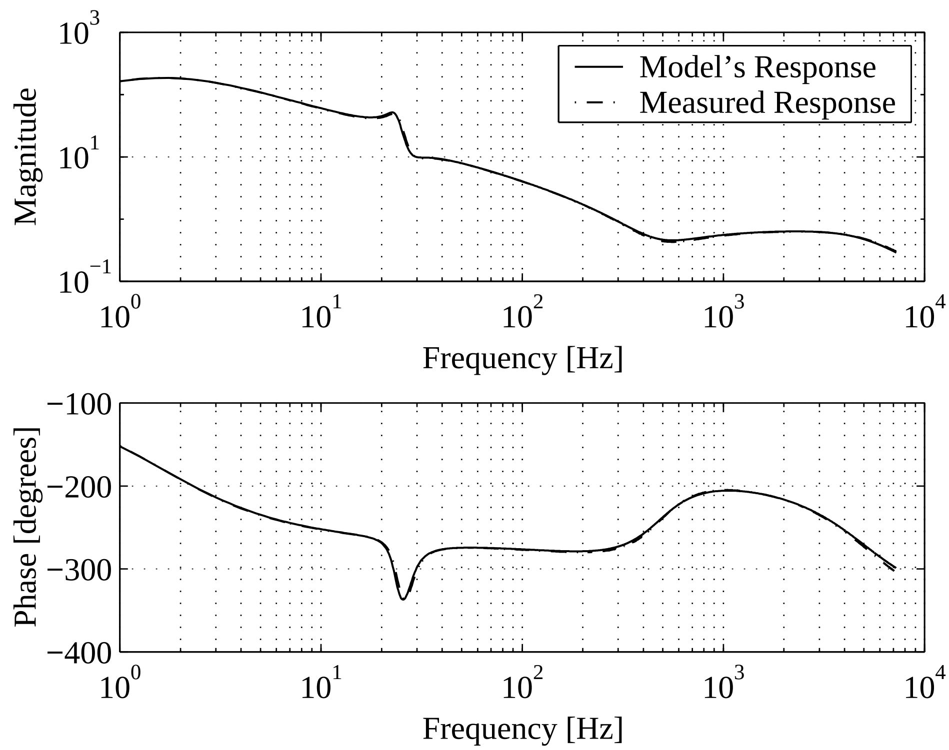

Figure 5.28: The Frequency Response of the Analog Application Controller K_{imp}

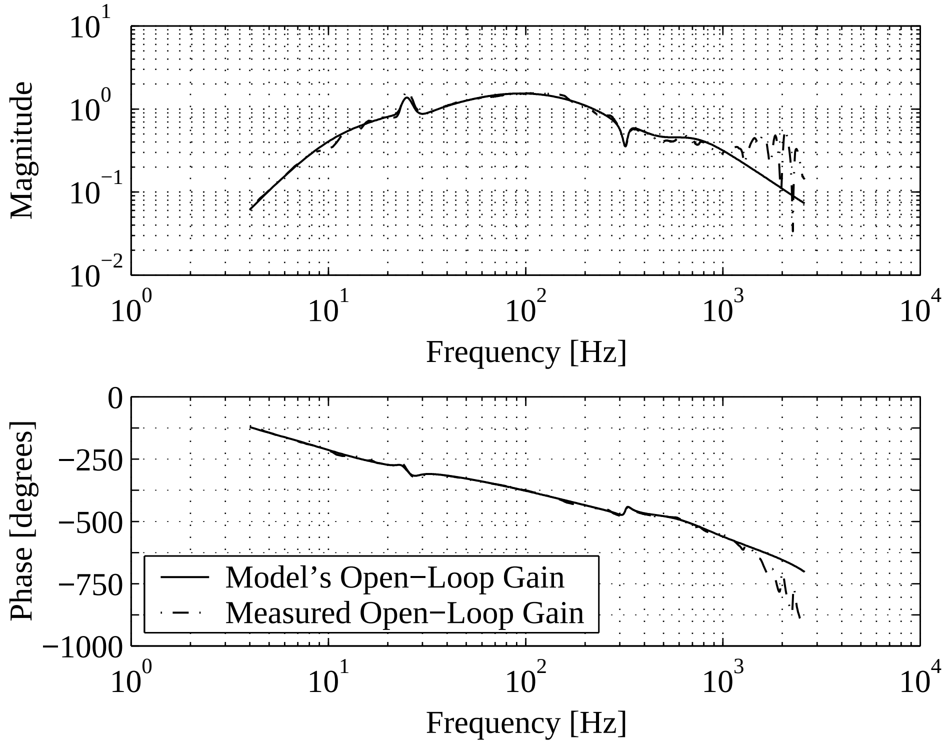

Figure 5.29: The Vented Loudspeaker System's Open-Loop Gain $\alpha G K_{imp}$

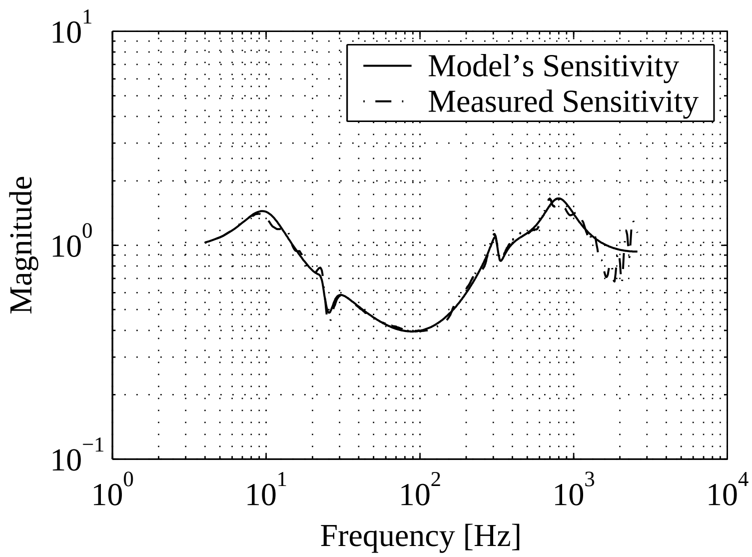

Figure 5.30: The Vented Loudspeaker System's Closed-Loop Sensitivity S

In Figures 5.31 and 5.32, the measured small-signal responses of p and p_{f} are illustrated, respectively, for both the controlled and uncontrolled cases. In addition,

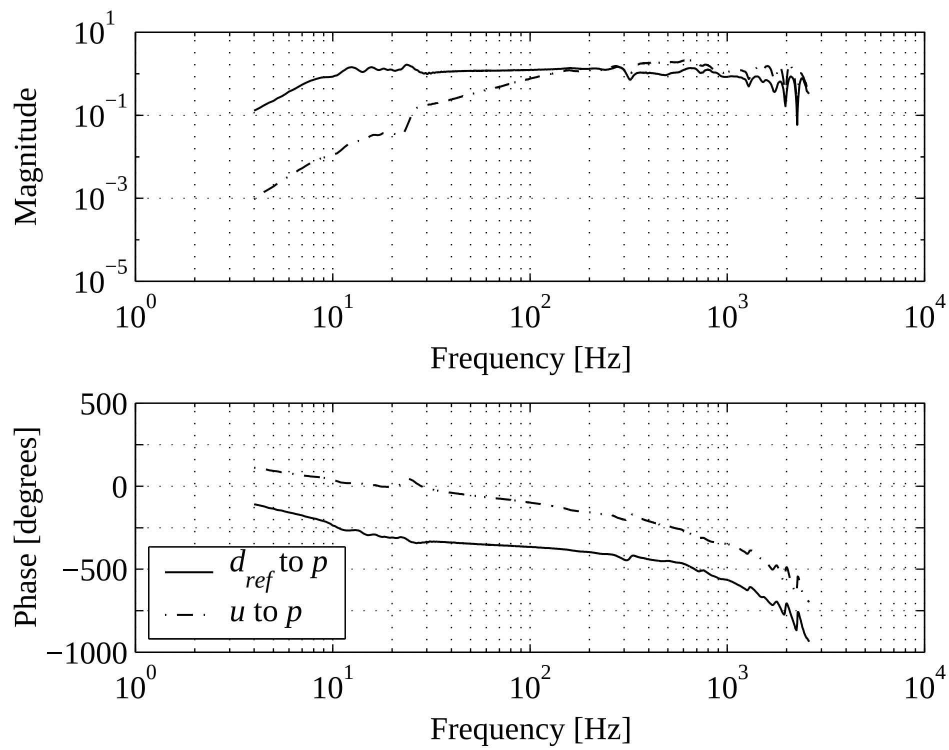

Figure 5.31: The Small-Signal, Closed-Loop Pressure Response Measurements of p for the Vented Loudspeaker System

Figure 5.33 shows the measured harmonic distortions for the system with ($=: \mathrm{THD}_{\mathrm{A_c}}$) and without ($=: \mathrm{THD}_{\mathrm{A_o}}$) control. The figure also shows the distortion reduction predictions $\mathrm{THD}_{\mathrm{A_{cp}}}$.

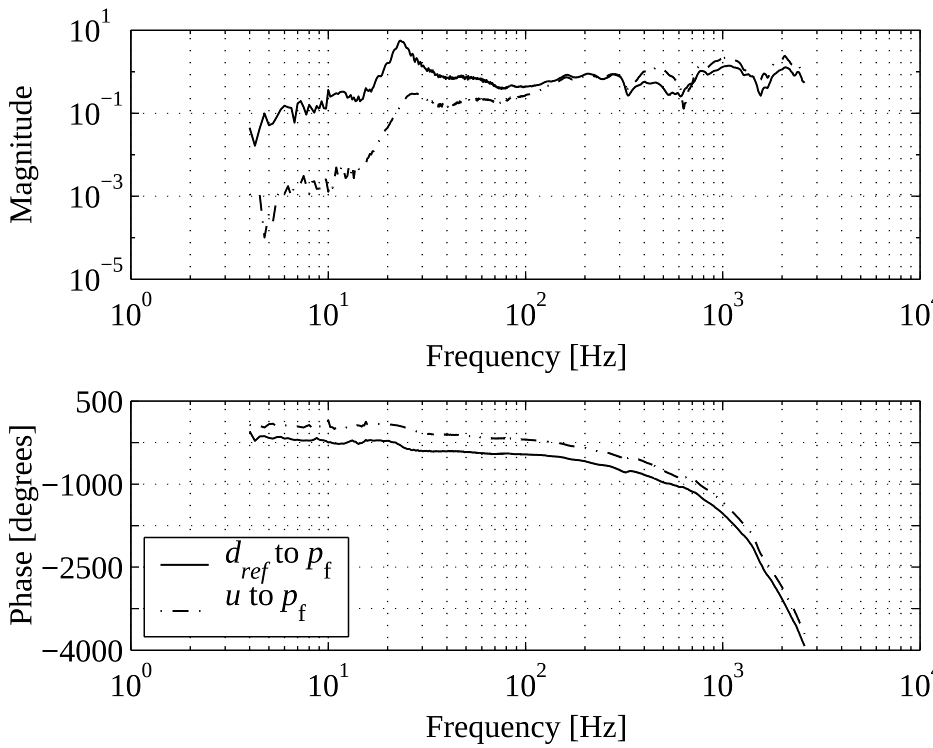

Figure 5.32: The Small-Signal, Closed-Loop Pressure Response Measurements of $p_{\rm f}$ for the Vented Loudspeaker System

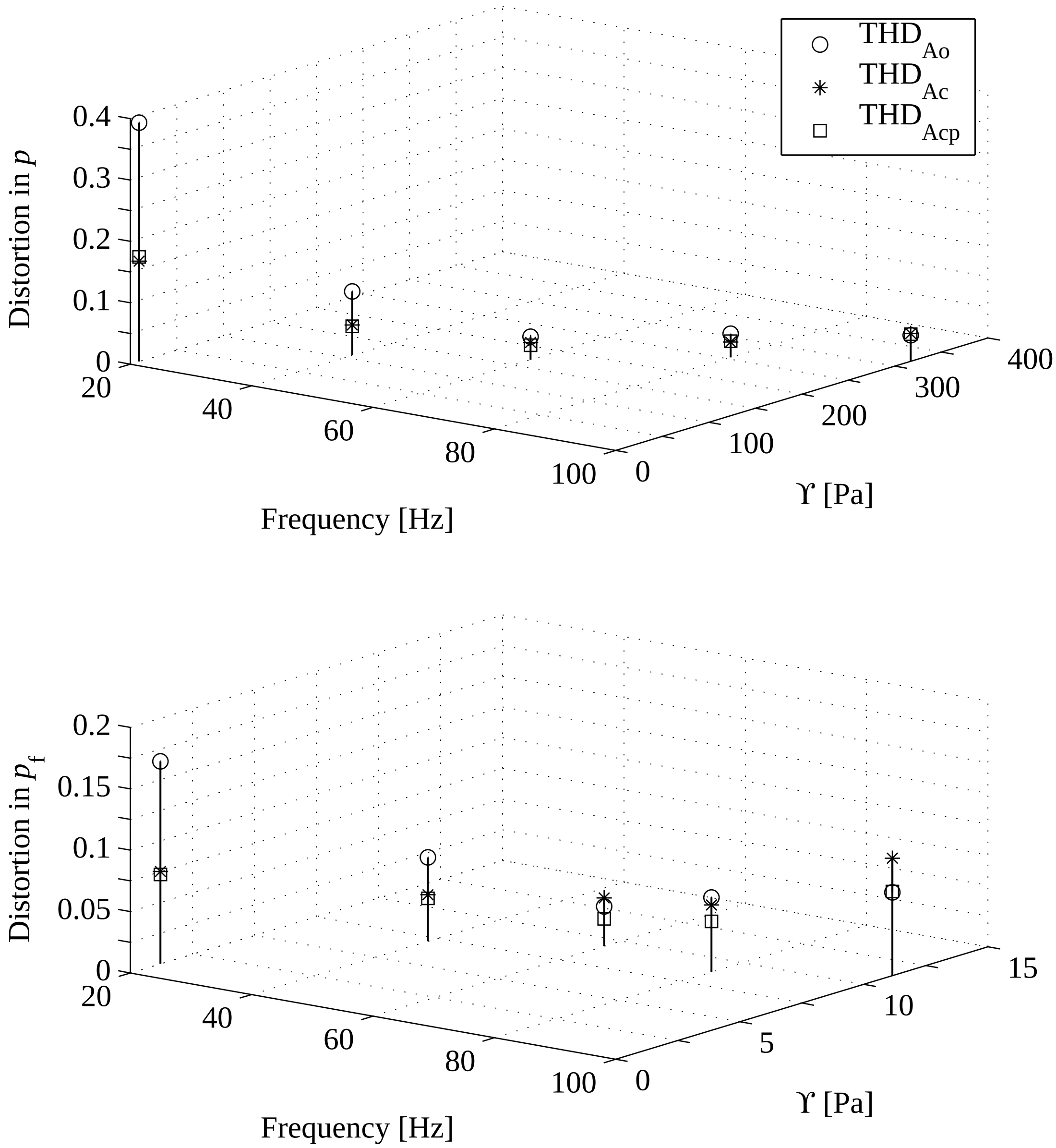

Figure 5.33: The Closed-Loop Distortion for the Vented Loudspeaker System

5.2.6 Discussion

A good quality microphone and an analog controller emulating a μ-design to control a loudspeaker in a vented enclosure were used to improve the loudspeaker's low-frequency pressure response. Figure 5.28 shows that the measured response of K_{imp} agreed well with the model in a wide range of frequencies. The same was true for Figure 5.30, in which the measured and predicted sensitivities show the desired shapes. Therefore, the results of the implementation agreed well with the simulations and the objectives for the μ-design were achieved in the implemented system. The sensitivity function's magnitude was less than unity from 15 Hz to 285 Hz and reached a minimum of 0.40 at 86 Hz, thus allowing a significant distortion reduction for the closed-loop system in that range. On the other hand, the magnitude response of S had peaks of 1.4 at 9 Hz and 1.65 at 792 Hz, due to the non-minimum phase nature of the plant dynamics. Although unavoidable, the peaks above unity were not unreasonably large.

Harmonic distortion tests were conducted to assess the reduction in nonlinear distortion. Figure 5.33 shows significant reductions in the harmonic distortion in p for the controlled case when the loudspeaker was driven with large signals, even though the uncontrolled loudspeaker already exhibited good linearity at high levels. As illustrated, these reductions were most significant when the loudspeaker was driven at lower frequencies $\left(\frac{\mathrm{THD}_{\mathrm{A_c}}}{\mathrm{THD}_{\mathrm{A_o}}} = 0.42 \text{ at } 20 \text{ Hz}\right)$. No distortion reduction was achieved beyond 100 Hz. This was expected as the controller was designed to reduce the distortion at low frequencies. Also, the distortion reduction relationship (3.55) provided a good approximation for the closed-loop distortion in p via the upper bound $\mathrm{THD}_{\mathrm{A_{cp}}}$. In addition, the figure shows similar reductions for the distortion in p_{f} (only when driven below 60 Hz), even though the signal p_{f} was not part of the performance objective. Note that $\mathrm{THD}_{\mathrm{A_{cp}}}$ shows reasonable agreement with $\mathrm{THD}_{\mathrm{A_c}}$ at those frequencies. Therefore, reducing the distortion at p will reduce the distortion at p_{f} in a comparable manner, when the system is driven below 60 Hz. On the other hand, the distortion at 60 Hz and 100 Hz were worsened in the controlled case. Even though this may seem undesirable, the distortion levels were already very low at these frequencies (without control), and were only slightly higher when the loudspeaker was controlled. Thus the degradation is not audibly significant.

5.3 Real Loudspeaker in a Sealed Enclosure

To further illustrate the usefulness of the control method to a variety of loudspeaker types, Figure 5.34 shows a diagram of a loudspeaker in a sealed enclosure along with an external feedback sensor (microphone). Since the enclosure is sealed,

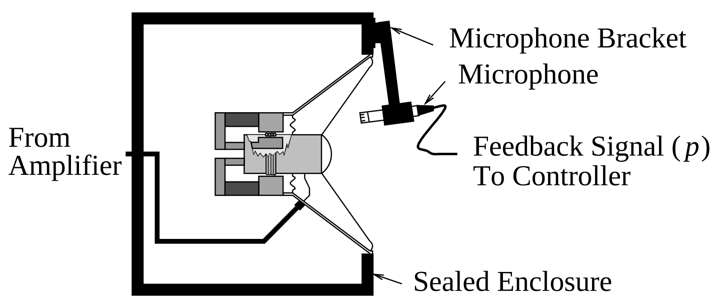

Figure 5.34: The Closed-Box Loudspeaker

it is assumed that the acoustic radiation emanates entirely from the moving cone. A microphone mounted 0.032 meters (1.25 inches) away from the cone's surface (at rest) measures the pressure p for feedback use. Unlike the vented case (where the feedback microphone is close to the cone, but far from the vent), the feedback microphone is nearest to the only source of acoustic radiation.

5.3.1 Plant Identification

To thoroughly study the loudspeaker's output, broadband, small amplitude sine-sweep experiments to measure the nominal frequency response (linear) and fixed-frequency large amplitude, steady-state sine-wave tests to measure the harmonic distortion (nonlinear) have been carried out. The experiments were performed in a 38 ft long, 19 ft wide, and 15 ft high laboratory with concrete walls, carpeted floor, and a ceiling covered with acoustical tile. Figure 5.35 shows the nominal frequency response measurements for the closed-box loudspeaker system, from the voltage into the amplifier (=: u) to the voltage from the microphone. In addition, Figure 5.36 shows the measured distortion (=: $\mathrm{THD}_{\mathrm{A_o}}$) for p at various frequencies and amplitudes. RMS averaging and uniform windowing methods were used.

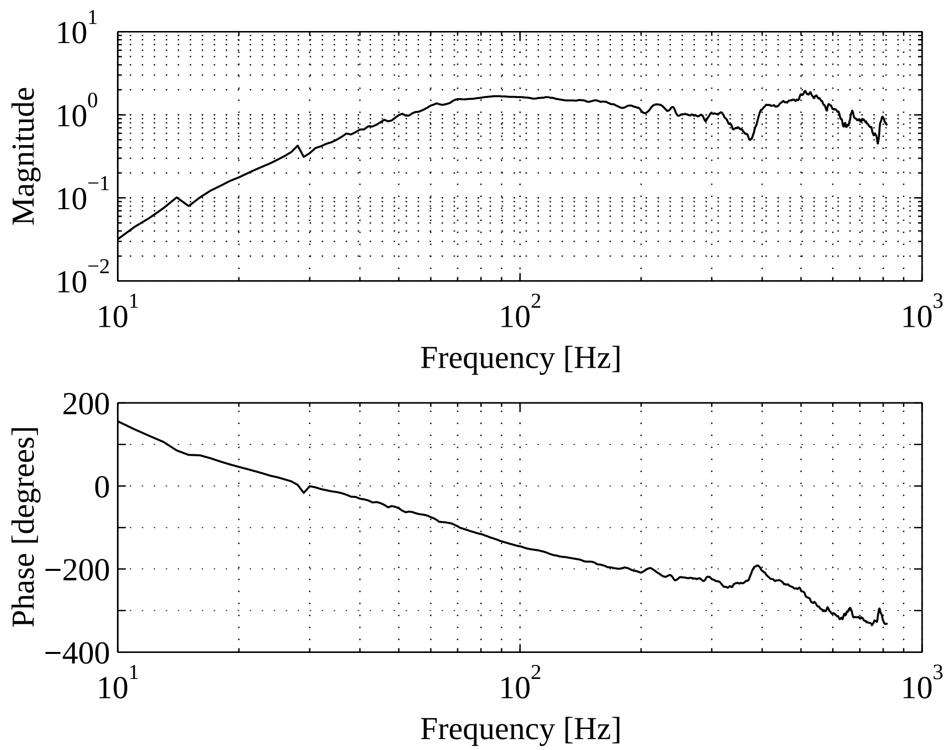

Figure 5.35: The Measured, Small-Signal Frequency Response of p for the Sealed Loudspeaker System

The plant included an 18 inch in diameter, professional grade loudspeaker (**AURA 1808**). Although a ported enclosure with 8 ft^3 of interior volume was recommended by the manufacturer for optimum performance, the transducer was mounted in a custom-made enclosure in a sealed configuration with 4 ft^3 of volume. This setup purposely limited the low-frequency response potential of the loudspeaker. The resulting system

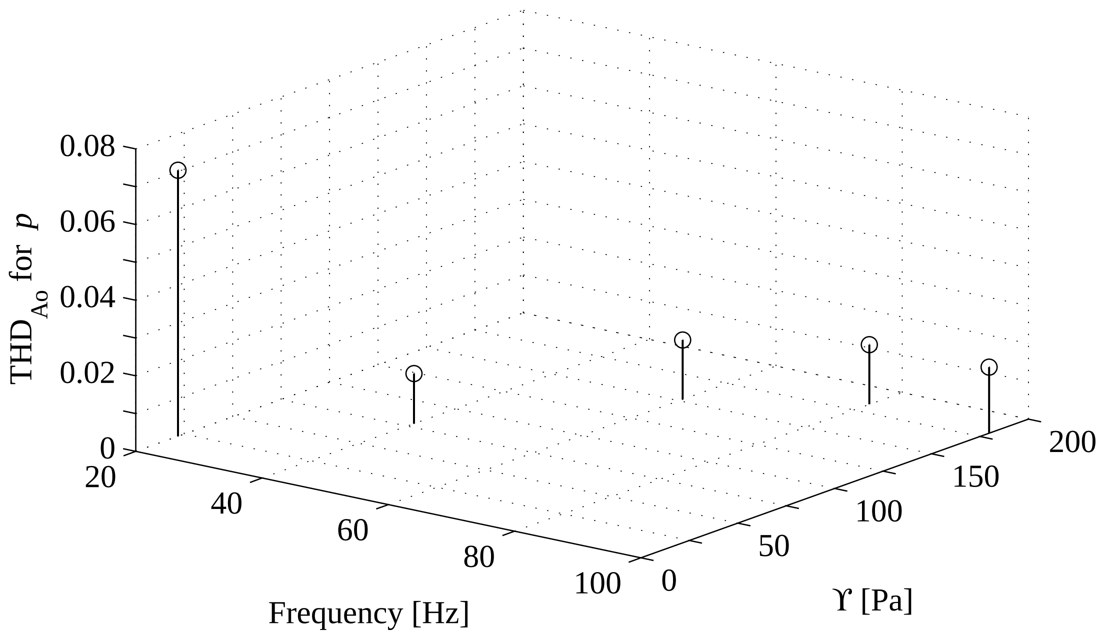

Figure 5.36: The Measured Distortion for the Sealed Loudspeaker System

was more compact, rigid, and lightweight, critical factors in some applications (e.g. automobiles). The plant also included a high-quality, voltage-drive amplifier, with the ability to produce 700 Watts RMS of continuous power (**QSC MX1000a**). A low-noise, high quality electret condenser microphone, used to measure the pressure produced by the loudspeaker, was also part of the plant (**LinearX M51**). This microphone's pressure signal was used for feedback control, as well as for evaluation. The plant data were computed from a vector-averaged, 512-point FFT of the pressure signal measurement (uniform window) and a sine-sweep input using the **HP35660A Dynamic Signal Analyzer**. As with the vented case, the input signal amplitude was kept small for the broadband test so that the distortion was as low as possible. The 7$^{\text{th}}$-order, SISO LTI model G_{nom} (shown in Figure 5.37) was fit using a frequency-domain, weighted least-squares algorithm. As the plot illustrates, the model fit agreed with the data in the region between 29 Hz and 300 Hz. Furthermore, the plant dynamics have non-minimum phase zeros at $63 \pm 46.4j$ and 5723 rad/s.

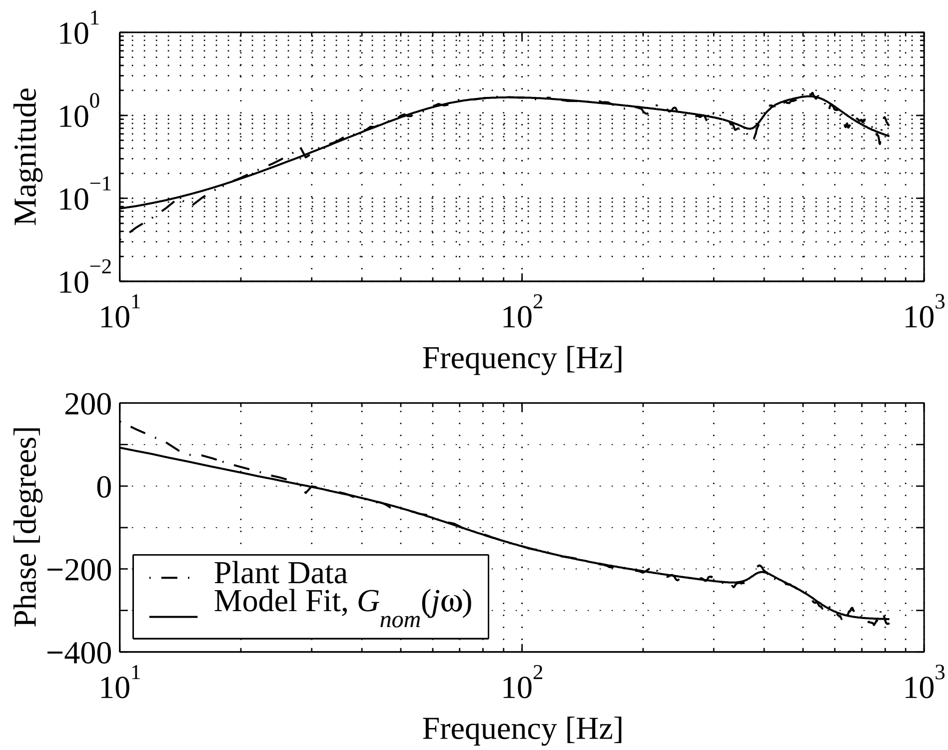

Figure 5.37: The Sealed Loudspeaker System's Nominal Model Fit, G_{nom}

5.3.2 Control Design: Uncertainty and Performance Objective Weights

Since the nominal plant is now represented by a linear system G_{nom}, a controller can be designed using the methods of Chapter 4, which can be implemented as shown in Figure 4.1.

Section 4.2.2 shows the frequency-domain weights utilized in the interconnection illustrated in Figure 4.5. In this case, the weights in Figure 4.7 were used.

5.3.3 Control Design: D-K Iteration

With the weights substituted into the interconnection structure (Figure 4.5), the open-loop interconnection (Figure 4.6) was computed. Note that since the frequency response of G_{nom} had a magnitude peak of 1.7, $\alpha := \frac{1}{1.7} = 0.59$, in this case. The 4×4, stable, transfer function P was 21^{st}-order, for this example, and the robust performance perturbation structure was given by (5.7).

The D-K iteration algorithm was implemented on the interconnection. This resulted in a stable, 45^{th}-order controller K, which satisfied the μ-objective after five iterations (the upper bound for μ achieved a peak of 0.89). Since the order of K was relatively high, a balanced truncation (to 9^{th}-order) was performed on it. Further simplification of the truncated controller was performed to make it suitable for analog circuit implementation (by manually manipulating some of the locations of its poles and zeros). Figure 5.38 shows the upper bounds for μ for both the simplified (=: K_{analog}) and μ-synthesized controllers, where a peak of 0.99 was achieved when K_{analog} was used. Figure 5.39 illustrates the finalized controller which was implemented in the system shown in Figure 4.1.

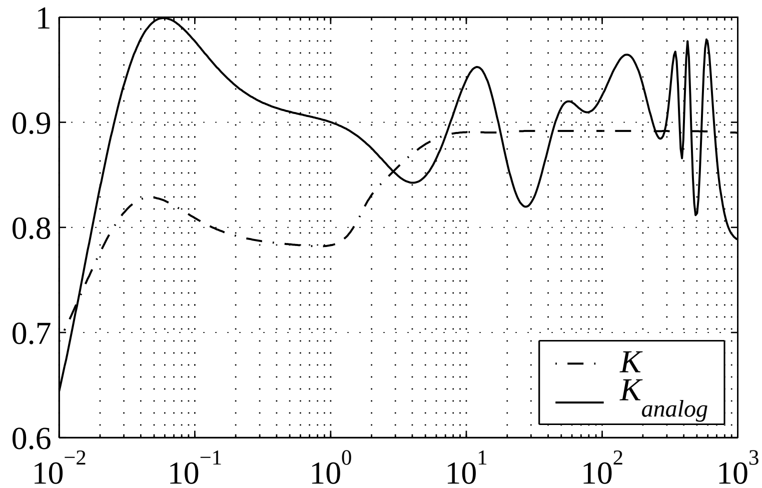

Figure 5.38: The μ Upper-Bounds for Various Controllers of the Sealed Loudspeaker System

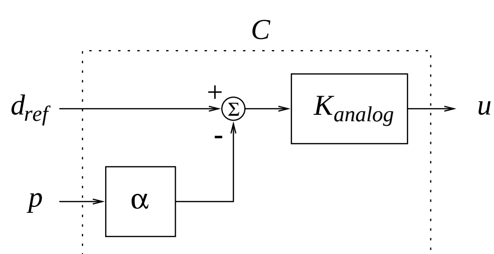

Figure 5.39: The Implemented Controller C for the Sealed Loudspeaker System

5.3.4 Control Design: Hardware Implementation

Using the same DSP mentioned for the vented loudspeaker example, the controller C (shown in Figure 5.39) was implemented as a discrete-time system. It was converted into the discrete-time domain via a bilinear transformation with a sampling time of 5×10^{-5} seconds, using (5.8). Since the sampling rate was 200 times higher than the upper operating frequency limit of the loudspeaker (100 Hz), the discretized controller was a valid approximation to C. As in the vented loudspeaker case, the DSP was used only for rapid prototyping of the designed controller. The controller C was finally implemented using a high-quality analog circuit.

5.3.5 Results

Implementing the control designs in hardware, the predicted performance improvements for the loudspeaker in a sealed enclosure were verified. Both the predicted and measured responses of K_{analog} are plotted in Figure 5.40. Also, the measured and the model's open-loop gains (=: $\alpha G K_{analog}$) and sensitivity functions are shown in Figures 5.41 and 5.42, respectively. In addition, the small-signal response measurements of p for both the controlled and uncontrolled systems are plotted in Figure 5.43. The measured harmonic distortions for the system with (=: $\mathrm{THD}_{\mathrm{A_c}}$) and without (=: $\mathrm{THD}_{\mathrm{A_o}}$) the controller are shown in Figure 5.44.

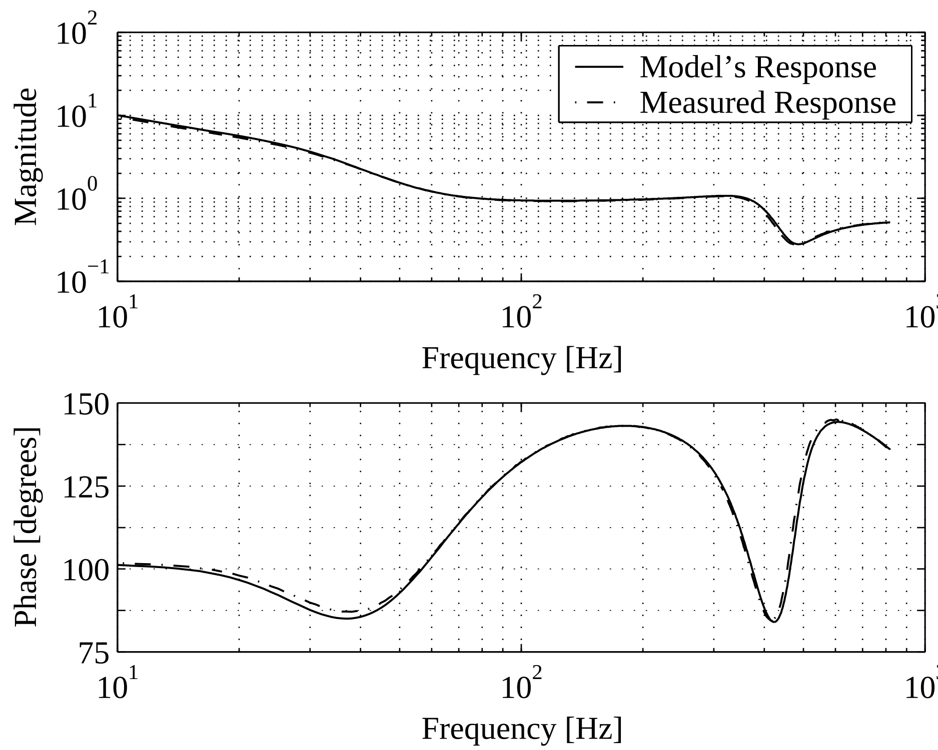

Figure 5.40: The Frequency Response of the Analog Application Controller K_{analog}

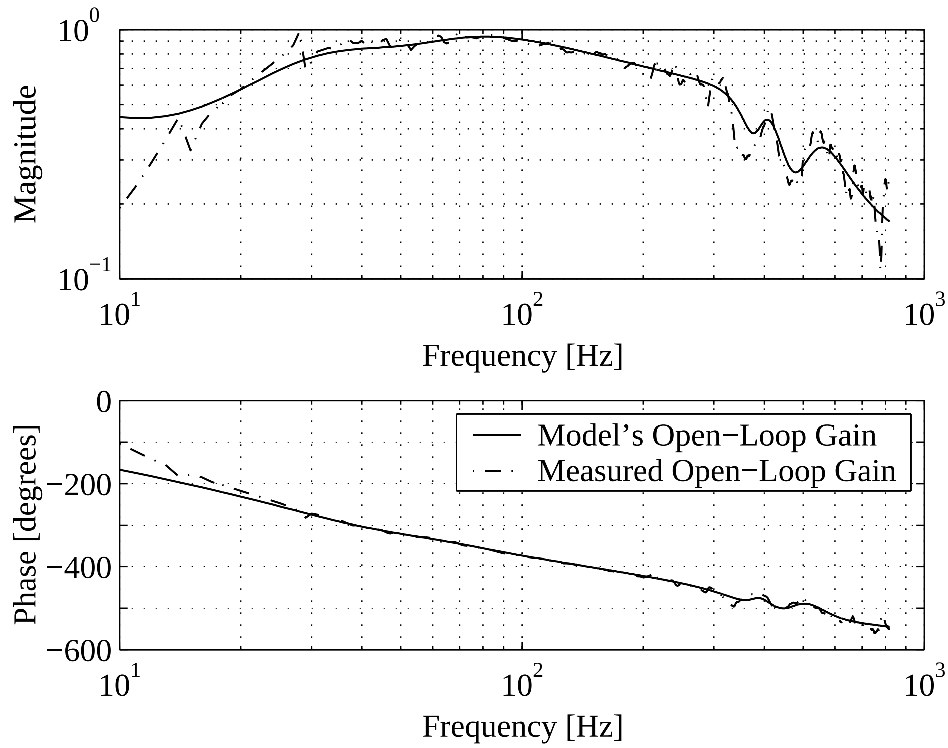

Figure 5.41: The Sealed Loudspeaker System's Open-Loop Gain αGK_{analog}

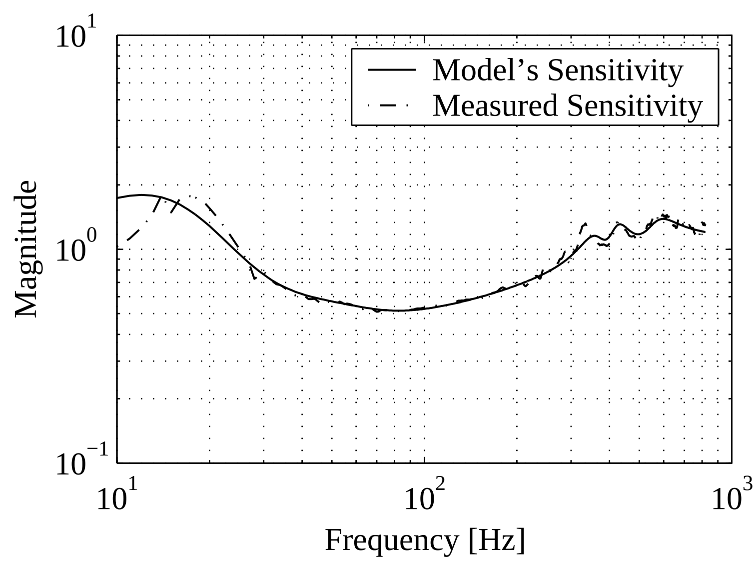

Figure 5.42: The Sealed Loudspeaker System's Closed-Loop Sensitivity S

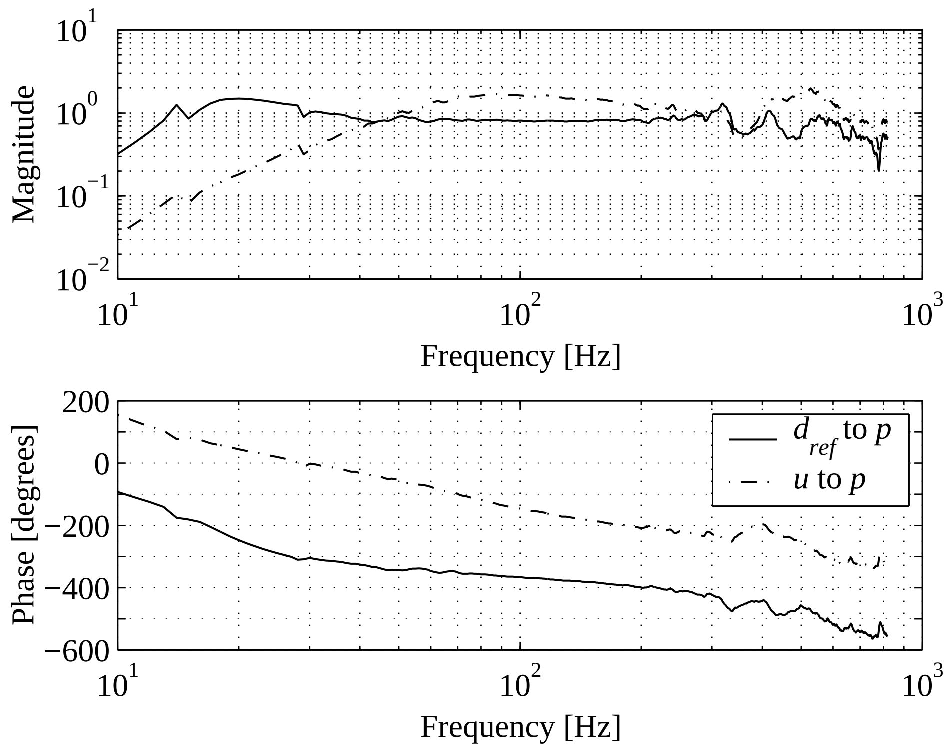

Figure 5.43: The Small-Signal, Closed-Loop Pressure Response Measurements of p for the Sealed Loudspeaker System

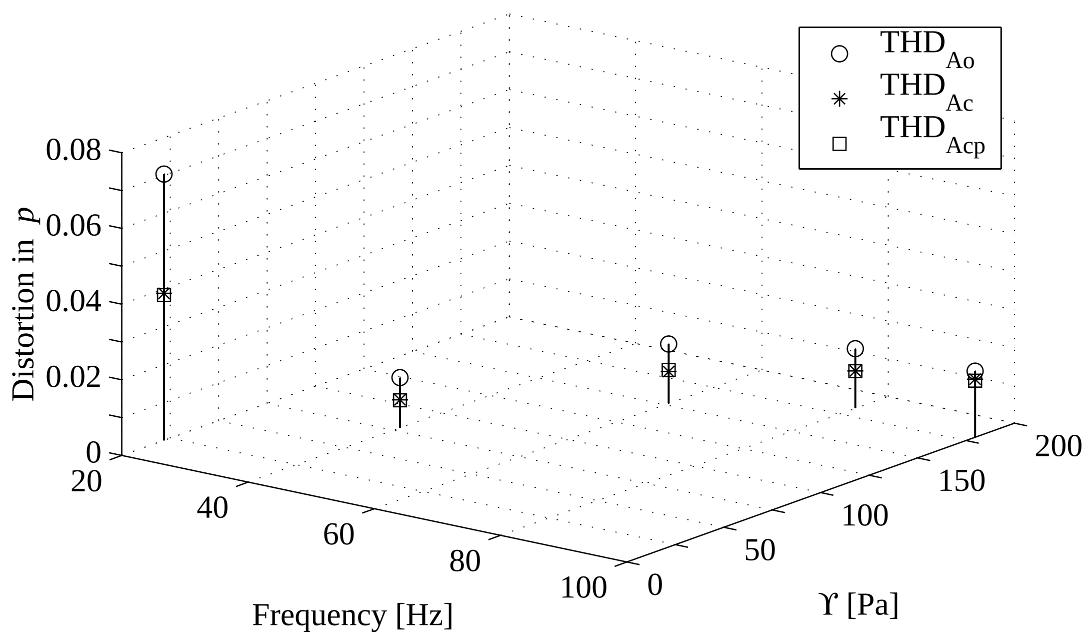

Figure 5.44: The Closed-Loop Distortion for the Sealed Loudspeaker System

5.3.6 Discussion

An improvement in the low-frequency pressure response of a loudspeaker in a sealed enclosure was achieved through the use of a high quality analog controller and a microphone implementing a μ-design. Figure 5.40 shows that the measured and predicted responses of K_{analog} agreed well in the frequency range between 10 Hz and 820 Hz. Also, Figure 5.42 shows that the measured and predicted sensitivities were in agreement between 29 and 300 Hz. Therefore, the implementation results agreed well with the simulations and the implemented system achieved the μ-design objectives. The magnitude of S was smaller than unity from 26 Hz to 312 Hz and reached a minimum of 0.51 at 70 Hz. Therefore, the closed loop system offered significant distortion reduction in this range (from (3.55)). On the other hand, the magnitude response of S contained the unavoidable (yet not too large) peaks of 1.78 at 17 Hz and 1.45 at 596 Hz (since the plant was non-minimum phase). Furthermore, the pressure response measurements for the controlled case (d_{ref} to p) showed marked improvement in the flatness of the magnitude and phase, as illustrated in Figure 5.43. This was desirable, since the response of p captured the pressure output near the cone, which was the only source of acoustic radiation.

To quantify the reduction in nonlinear distortion, harmonic distortion tests were conducted. As shown in Figure 5.44, measurable reductions in the harmonic distortion for the controlled case were observed when the loudspeaker was driven with large amplitude sinusoids. The improvement was most noticeable when the loudspeaker was driven at lower frequencies, where the ratio $\frac{\mathrm{THD}_{\mathrm{A_c}}}{\mathrm{THD}_{\mathrm{A_o}}}$ achieved a low of 0.55 (for the 20 Hz case). Small reductions in distortion were observed when the loudspeaker was driven at 100 Hz $\left(\frac{\mathrm{THD}_{\mathrm{A_c}}}{\mathrm{THD}_{\mathrm{A_o}}} = 0.88\right)$. This was expected, since the controller was designed to improve the loudspeaker's low-frequency response. In addition, $\mathrm{THD}_{\mathrm{A_{cp}}}$ agreed well with $\mathrm{THD}_{\mathrm{A_c}}$ across all tested frequencies. This further proves the usefulness of $\mathrm{THD}_{\mathrm{A_{cp}}}$ as a predictor of the distortion for the closed-loop system when a mildly nonlinear system is controlled using a linear feedback controller.

Chapter 6

Conclusion

This dissertation documented a comprehensive study of loudspeaker modeling and control. A lumped-parameter model for a voice-coil loudspeaker in a vented enclosure was presented that derived from a consideration of physical principles. Furthermore, a low-frequency (20 Hz to 100 Hz), feedback control method designed to improve the nonlinear performance of the loudspeaker and a suitable performance measure for use in design and evaluation were proposed. Data from experiments performed on a variety of actual loudspeakers confirmed the usefulness of the theory developed in this work.

In Chapter 2, a lumped-parameter loudspeaker model was analyzed. Even though the model was simple, much of the loudspeaker's nonlinear behavior was accurately captured. The model formulation allowed a relatively easy application of modern control system techniques. The model also lent itself well to modern parametric identification methods. One attractive feature of the model was its special structure, each element of which was individually studied. The modular approach to model construction allowed further refinement in each element while still keeping the overall structure simple (e.g. adding dynamics to the enclosure). It should be noted that effects such as mechanical suspension hysteresis, nonlinear mechanical damping, asymmetrical magnetic fields, and non-symmetric mechanical stiffness were not included. Their influences on the response of a properly designed loudspeaker are secondary in comparison to the nonlinearities that were considered, which may add considerable complexity to the loudspeaker model. However, these effects are currently being researched and evaluated, in order to refine the model to a level beyond what was achieved.

To properly ascertain the nonlinear performance of the loudspeaker system, a suitable nonlinear distortion measure ($\mathrm{THD_A}$) was proposed in Chapter 3 and compared with other distortion measures currently used in practice. Also, the linearizing effect of feedback using a linear controller (both static and dynamic) on some nonlinear systems was analyzed. The results showed that the distortion reduction was potentially significant and a useful upper bound (based on the sensitivity function S) on the closed-loop distortion was found (see (3.55)). Examples were given that verified the findings. In addition, the theory allowed for the proper design of a linear controller to improve the nonlinear performance (by reducing $\mathrm{THD_A}$) of mildly nonlinear systems.

Chapter 4 outlined a feedback scheme based on robust control theory, which was applied to the loudspeaker system. Using the pressure output of the loudspeaker system for feedback, the technique offered significant advantages over those previously attempted. One advantage was the simplicity of implementation. Specifically, a pressure transducer and a simple linear filter were all that was necessary for realizing the control method. Also, the controlled loudspeaker system had guaranteed specified performance even in the face of uncertainties in the loudspeaker system's dynamics. It also offered ample disturbance rejection and reduced sensitivity to sensor noise. Since this method is non-invasive to the loudspeaker, it can be used as a retrofit to existing loudspeaker systems without adverse effects. In addition, the issue of non-minimum phase dynamics of the uncontrolled system was addressed when designing the controller. Care was taken so that the fundamental limits on the performance of non-minimum phase systems were not exceeded.

Examples that prove the utility of the theory developed in this dissertation on a variety of loudspeaker systems were presented in Chapter 5. The first example involved the low-frequency control of the loudspeaker model constructed in Chapter 2, using a μ-designed controller. Even though the feedback signal only included the pressure near the loudspeaker's cone, the closed-loop system also showed predictable improvement in the pressure response at a location approximately 1 meter away. Figures 5.16 and 5.17 show large reductions in the harmonic distortion for both pressure locations. The plots revealed that the ratio $\frac{\mathrm{THD}_{\mathrm{A_c}}}{\mathrm{THD}_{\mathrm{A_o}}}$ reached a minimum of 0.38 at low-frequencies. The upper bound on the predicted closed-loop distortion also showed good agreement throughout a large range of amplitudes. The reductions in distortion were minimal when the loudspeaker was driven at high frequencies $\left(\frac{\mathrm{THD}_{\mathrm{A_c}}}{\mathrm{THD}_{\mathrm{A_o}}} = 0.81 \text{ for } 100 \text{ Hz}\right)$. This was not surprising, since the controller was designed to increase the performance at low frequencies. The transient behavior of the loudspeaker system was also studied, by using specific sinusoidal inputs with a frequency of 20 Hz and amplitudes that significantly excited the nonlinearities, as shown in Figure 5.18. The transient response of the loudspeaker was improved due to the control scheme, as illustrated in Figures 5.19 and 5.20. This was done without the introduction of extra delays in the pressure responses.

The second example examined an actual loudspeaker enclosed in a vented configuration. A μ-based analog controller was used in conjunction with a good quality microphone (which measured the pressure near the loudspeaker's cone) to control the low-frequency response of the loudspeaker with good results. As shown in Figure 5.33, measurable reductions in harmonic distortion were recorded for the controlled case. By design, the ratio $\frac{\mathrm{THD}_{\mathrm{A_c}}}{\mathrm{THD}_{\mathrm{A_o}}}$ became smaller when the loudspeaker was driven at low frequencies $\left(\frac{\mathrm{THD}_{\mathrm{A_c}}}{\mathrm{THD}_{\mathrm{A_o}}} = 0.42 \text{ for } 20 \text{ Hz}\right)$, with virtually no distortion reduction beyond 100 Hz. The bound on the predicted closed-loop distortion provided a good approximation to that of the closed-loop system, for the pressure measured near the cone. For frequencies below 60 Hz, Figure 5.33 shows similar improvements (that were accurately predicted) in performance for the measured pressure response approximately

1 meter away from the loudspeaker, even though that pressure signal was not part of the performance objective. The controlled system's performance, however, worsened at 60 Hz and 100 Hz. Happily, the distortion levels were already very low at these frequencies for the uncontrolled loudspeaker and were only slightly higher for the controlled case. The performance degradation, therefore, posed no concern.

Finally, the last example successfully implemented an analog controller (emulating a μ-design) and a microphone, which measured the pressure near the cone of a loudspeaker in a sealed enclosure, to control the pressure response in the low-frequency region. From Figure 5.43, the measured pressure response for the controlled case exhibited significant improvement in the flatness of the magnitude and phase. Furthermore, Figure 5.44 displays measurable reductions in harmonic distortion for the controlled case. As with the previous examples, the improvement was most significant when the loudspeaker was driven at lower frequencies, where the ratio $\frac{\mathrm{THD}_{\mathrm{A_c}}}{\mathrm{THD}_{\mathrm{A_o}}}$ reached a minimum of 0.55 for the 20 Hz case and increased to 0.88 for 100 Hz. The predicted closed-loop distortion demonstrated even better agreement with the measurements than that of the second example. This was true across all tested frequencies.

As can be seen from the forgoing, the methods outlined in this work can produce predictable and measurable improvements in the nonlinear performance of a low-frequency, voice-coil loudspeaker (attached to either vented or sealed enclosures). The successful implementations have motivated further work in the areas of improving the loudspeaker model, finding other suitable measures of distortion, and exploring alternative control techniques.

Appendix A

Solving the Equations for the Acoustic Half-Space

From Section 2.2, the solution that satisfies (2.12), (2.13), and (2.14) was given as (2.17). To show this, some properties of (2.18), which is radially symmetric are listed. Then, a general version of (2.17) is shown to solve the Helmholtz equation (2.12). Finally, the proposed solution is proven to satisfy the boundary condition (2.14).

A.1 Some Properties of Radially Symmetric Functions

Let $\varphi : \mathbb{R} \to \mathbb{R}$ and $\phi : \mathbb{R}^n \to \mathbb{R}$ be defined such that

$$\phi(\gamma) := \varphi\left(\|\gamma\|\right). \tag{A.1}$$

Define $\varphi'\left(\|\gamma\|\right) := \frac{d\varphi(\|\gamma\|)}{d(\|\gamma\|)}$, $\varphi''\left(\|\gamma\|\right) := \frac{d^2\varphi(\|\gamma\|)}{d(\|\gamma\|)^2}$, and let γ_i be the i^{th} element of the vector γ. Then,

$$\left(\vec{\nabla}\phi\right)_i = \varphi'\left(\|\gamma\|\right)\frac{\gamma_i}{\|\gamma\|}, \quad \gamma \neq 0_n, \tag{A.2}$$

$$\vec{\nabla}\phi = \frac{\varphi'(\|\gamma\|)}{\|\gamma\|}\gamma, \tag{A.3}$$

$$\|\vec{\nabla}\phi\| = |\varphi'(\|\gamma\|)|, \tag{A.4}$$

$$\vec{\nabla}\phi \cdot \frac{\gamma}{\|\gamma\|} = \varphi'(\|\gamma\|), \quad \gamma \neq 0_n, \tag{A.5}$$

$$\begin{aligned} \int_{\mathcal{B}(0,R)} \phi(\gamma) d\gamma &= \int_0^R \int_{\partial\mathcal{B}(0,r)} \phi(S,r)\ dS\ dr \\ &= \int_0^R \int_{\partial\mathcal{B}(0,r)} \varphi(r)\ dS\ dr \\ &= \int_0^R \varphi(r) n\alpha(n) r^{n-1}\ dr, \end{aligned} \tag{A.6}$$

where $\alpha(n)$ is the volume of the unit ball in $\mathbb{R}^n$. So, $\alpha(n)r^n$ is the volume of the ball of radius r and $n\alpha(n)r^{n-1}$ is its surface area. For $n = 3$, $n\alpha(n) = 4\pi$.

Note that

$$\int_0^R \frac{1}{r^k} dr = \begin{cases} \frac{1}{1-k} R^{1-k} & \text{if } k < 1 \\ \text{diverges} & \text{if } k \geq 1. \end{cases} \tag{A.7}$$

Therefore, $\phi \in \mathcal{L}_{1,\text{loc}}$ if $\varphi(r) = \frac{1}{r^k}$ for $k < n$; $\phi \notin \mathcal{L}_{1,\text{loc}}$ if $\varphi(r) = \frac{1}{r^k}$ for $k \geq n$.

Furthermore,

$$\int_{\partial\mathcal{B}(0,R)} \vec{\nabla}\phi \cdot \frac{\gamma}{\|\gamma\|}\ dS = n\alpha(n) R^{n-1} \varphi'(R), \tag{A.8}$$

$$\Delta\phi = \varphi''(\|\gamma\|) + \frac{n-1}{\|\gamma\|}\varphi'(\|\gamma\|), \ \gamma \neq 0_n, \tag{A.9}$$

$$\int_{\partial\mathcal{B}(0,R)} \phi\ dS = \varphi(R) n\alpha(n) R^{n-1}. \tag{A.10}$$

A.2 Solving the Helmholtz Equation

The properties for radially symmetric functions are used to show what follows. Consider a specific φ, namely

$$\varphi = \frac{q}{r} e^{\beta r}, \tag{A.11}$$

where q and β are constants (possibly complex, $\beta \neq 0$). Then,

$$\begin{aligned} \varphi'(r) &= -\frac{q}{r^2}e^{\beta r} + \frac{\beta q}{r}e^{\beta r} \\ &= \frac{q}{r}\left(-\frac{1}{r} + \beta\right)e^{\beta r}, \end{aligned} \tag{A.12}$$

$$\begin{aligned} \varphi''(r) &= \frac{2q}{r^3}e^{\beta r} - \frac{\beta q}{r^2}e^{\beta r} - \frac{\beta q}{r^2}e^{\beta r} + \frac{\beta^2 q}{r}e^{\beta r} \\ &= \left(\frac{2q}{r^3} - \frac{2\beta q}{r^2} + \frac{\beta^2 q}{r}\right)e^{\beta r}. \end{aligned} \tag{A.13}$$

For $n = 3$,

$$\begin{aligned} \varphi'' + \frac{n-1}{r}\varphi' &= \left(\frac{2q}{r^3} - \frac{2\beta q}{r^2} + \frac{\beta^2 q}{r}\right)e^{\beta r} + \frac{2}{r}\left(-\frac{q}{r^2} + \frac{\beta q}{r}\right)e^{\beta r} \\ &= \frac{\beta^2 q}{r}e^{\beta r} \\ &= \beta^2\varphi(r). \end{aligned} \tag{A.14}$$

So, for $n = 3$, $\phi(\gamma) := \frac{q}{\|\gamma\|}e^{\beta\|\gamma\|}$ and

$$\Delta\phi = \beta^2\phi, \tag{A.15}$$

which is valid on $\mathbb{R}^3/0_3$ for any q and $\beta \neq 0$. Note: For $n \geq 2$, (A.1) is locally integrable. Hence, ϕ defines a distribution. Therefore, the case of $n = 3$ will be emphasized. From (A.8) and (A.12)

$$\begin{aligned} \int_{\partial\mathcal{B}(0,R)} \vec{\nabla}\phi \cdot \frac{\gamma}{\|\gamma\|}\, dS &= 3\alpha(3)R^2\frac{q}{R}\left(\frac{-1}{R} + \beta\right)e^{\beta R} \\ &= 3\alpha(3)q\left(-1 + \beta R\right)e^{\beta R}. \end{aligned} \tag{A.16}$$

Hence,

$$\lim_{R\to 0}\int_{\partial\mathcal{B}(0,R)} \vec{\nabla}\phi \cdot \frac{\gamma}{\|\gamma\|}\, dS = -3\alpha(3)q,\ \ \beta \in \mathbb{C}. \tag{A.17}$$

Also, from (A.10)

$$\begin{aligned} \int_{\partial\mathcal{B}(0,R)} \phi\, dS &= 3\varphi(R)\alpha(3)R^2 \\ &= 3\alpha(3)qRe^{\beta R}, \end{aligned} \tag{A.18}$$

which gives

$$\lim_{R\to 0}\int_{\partial\mathcal{B}(0,R)} \phi \; dS = 0. \tag{A.19}$$

Lemma A.1 *As a distribution,*

$$\Delta\phi - \beta^2\phi = -3q\alpha(3)\delta, \tag{A.20}$$

where δ is the Dirac-delta *distribution.*

Proof: Let $v \in \mathcal{C}_c^\infty(\mathbb{R}^3)$. Then, by definition,

$$\left(\Delta\phi - \beta^2\phi\right)(v) := \int_{\mathbb{R}^3}\left(\phi\Delta v - \beta^2\phi v\right) d\gamma \tag{A.21}$$

Taking $\epsilon > 0$,

$$\begin{aligned}
\left(\Delta\phi - \beta^2\phi\right)(v) &= \int_{\mathcal{B}(0,\epsilon)}\left(\phi\Delta v - \beta^2\phi v\right) d\gamma + \int_{\mathbb{R}^3/\mathcal{B}(0,\epsilon)}\left(\phi\Delta v - \beta^2\phi v\right) d\gamma \\
&= \int_{\mathcal{B}(0,\epsilon)}\left(\phi\Delta v - \beta^2\phi v\right) d\gamma + \int_{\mathbb{R}^3/\mathcal{B}(0,\epsilon)} \phi\Delta v \; d\gamma - \beta^2\int_{\mathbb{R}^3/\mathcal{B}(0,\epsilon)} \phi v \; d\gamma \\
&= \int_{\mathcal{B}(0,\epsilon)}\left(\phi\Delta v - \beta^2\phi v\right) d\gamma + \int_{\mathbb{R}^3/\mathcal{B}(0,\epsilon)} \Delta\phi v \; d\gamma \\
&\quad + \int_{\partial\mathcal{B}(0,\epsilon)} \phi\vec{\nabla}v\cdot\frac{-\gamma}{\|\gamma\|}\; dS - \int_{\partial\mathcal{B}(0,\epsilon)} v\vec{\nabla}\phi\cdot\frac{-\gamma}{\|\gamma\|}\; dS \\
&\quad -\beta^2\int_{\mathbb{R}^3/\mathcal{B}(0,\epsilon)} \phi v \; d\gamma \\
&= \int_{\mathcal{B}(0,\epsilon)}\left(\phi\Delta v - \beta^2\phi v\right) d\gamma + \int_{\mathbb{R}^3/\mathcal{B}(0,\epsilon)}\left(\Delta\phi - \beta^2\phi\right) v \; d\gamma \\
&\quad - \int_{\partial\mathcal{B}(0,\epsilon)} \phi\vec{\nabla}v\cdot\frac{\gamma}{\|\gamma\|}\; dS + \int_{\partial\mathcal{B}(0,\epsilon)} v\vec{\nabla}\phi\cdot\frac{\gamma}{\|\gamma\|}\; dS,
\end{aligned} \tag{A.22}$$

where the second to last step was obtained using

$$\int_\Omega\left(\phi\Delta v - v\Delta\phi\right)\; d\gamma = \int_{\partial\Omega}\phi\vec{\nabla}v\cdot\vec{n}\; dS - \int_{\partial\Omega} v\vec{\nabla}\phi\cdot\vec{n}\; dS, \tag{A.23}$$

where $\vec{n}$ is the outward (from Ω) unit normal vector of $\partial\Omega$ and $v \in \mathcal{C}_c^\infty$. This is referred to as *Green's Identity* [50].

Note that since $\phi \in \mathcal{L}_{1,\mathrm{loc}}$ and $v \in \mathcal{C}_c^\infty$, it is observed from the final expression in (A.22) that

- The 1^{st} integral vanishes as $\epsilon \to 0$.
- The 2^{nd} integral $\equiv 0$, since $\Delta\phi - \beta^2\phi \equiv 0$ for $\gamma \neq 0_3$ (from (A.15)).
- Using (A.19), the 3^{rd} integral vanishes as $\epsilon \to 0$.
- Using (A.17) and by continuity of v, the 4^{th} integral tends to $-3v(0)\alpha(3)q$.

Hence,

$$\left(\Delta\phi - \beta^2\phi\right)(v) = -3q\alpha(3)v(0). \tag{A.24}$$

■

Lemma A.2 *Consider*

$$\begin{aligned}\frac{\partial\phi}{\partial\gamma_3} &= \varphi'(\|\gamma\|)\frac{\gamma_3}{\|\gamma\|} \\ &= \gamma_3\frac{q}{r^2}\left(\frac{-1}{r} + \beta\right)e^{\beta r}.\end{aligned} \tag{A.25}$$

Fix $\gamma_3 = z > 0$, and view (A.25) as a function of the two remaining variables, i.e.

$$\Psi_z(x,y) := \frac{zq}{x^2+y^2+z^2}\left(\frac{-1}{\sqrt{x^2+y^2+z^2}} + \beta\right)e^{\beta\sqrt{x^2+y^2+z^2}}, \tag{A.26}$$

where $r := \sqrt{x^2+y^2+z^2}$. Let $\beta := j\sigma,\ \sigma \in \mathbb{R}$ and take $v \in \mathcal{C}_c(\mathbb{R}^2) \cap \mathcal{L}_\infty$. Then,

$$\lim_{\substack{z\to 0\\ z>0}} \int_{\mathbb{R}^2} \Psi_z(\gamma)v(\gamma)\, d\gamma = -2\pi q v(0). \tag{A.27}$$

Proof: Note that $\Psi_z(x,y)$ is radially symmetric on $\mathbb{R}^2$. Define $\tau_z : \mathbb{R} \to \mathbb{C}$ as

$$\tau_z(R) := \frac{zq}{R^2+z^2}\left(\frac{-1}{\sqrt{R^2+z^2}} + \beta\right)e^{\beta\sqrt{R^2+z^2}}, \tag{A.28}$$

where $R := \sqrt{x^2+y^2}$. So, for any $R \neq 0$, $\lim_{z\to 0}\tau_z(R) = 0$.

Integrating over the annulus $R_i \leq \sqrt{x^2+y^2} \leq R_o$,

$$\begin{aligned}
\int_{R_i \leq \sqrt{x^2+y^2} \leq R_o} \Psi(x,y)\ dx\ dy &= \int_{R_i}^{R_o} \int_0^{2\pi} \tau_z(r,\theta) r\ d\theta\ dr \\
&= \int_{R_i}^{R_o} \frac{2\pi z q}{r^2+z^2} \left(\frac{-1}{\sqrt{r^2+z^2}} + \beta \right) e^{\beta\sqrt{r^2+z^2}}\ r\ dr \\
&= 2\pi q \int_{R_i}^{R_o} \frac{zr}{r^2+z^2} \left(\frac{-1}{\sqrt{r^2+z^2}} + \beta \right) e^{\beta\sqrt{r^2+z^2}}\ dr \\
&= 2\pi q z \left[\frac{e^{\beta\sqrt{R_o^2+z^2}}}{\sqrt{R_o^2+z^2}} - \frac{e^{\beta\sqrt{R_i^2+z^2}}}{\sqrt{R_i^2+z^2}} \right]. \qquad \text{(A.29)}
\end{aligned}$$

If $\Re(\beta) \leq 0$ and since $z > 0$,

$$\begin{aligned}
\int_{\mathbb{R}^2} \Psi_z(\gamma)\ d\gamma &= \lim_{\substack{R_i \to 0 \\ R_o \to \infty}} 2\pi \int_{R_i}^{R_o} \tau_z(r) r\ dr \\
&= 2\pi q z \lim_{R_o \to \infty} \left[\frac{e^{\beta\sqrt{R_o^2+z^2}}}{\sqrt{R_o^2+z^2}} - \frac{e^{\beta z}}{z} \right] \\
&= -2\pi q e^{\beta z}. \qquad \text{(A.30)}
\end{aligned}$$

Fix $z > 0$ and take

$$K(z) := \left| \int_{\mathbb{R}^2} \Psi_z(\gamma) \left[v(\gamma) - v(0) \right]\ d\gamma \right|. \qquad \text{(A.31)}$$

Let $\epsilon > 0$ and choose $\delta > 0$ so that $|v(\gamma) - v(0)| \leq \epsilon$ for $|\gamma| \leq \delta$. Then,

$$\begin{aligned}
K(z) &= \left| \int_{\mathcal{B}(0,\delta)} \Psi_z(\gamma) \left[v(\gamma) - v(0) \right]\ d\gamma + \int_{\mathbb{R}^2/\mathcal{B}(0,\delta)} \Psi_z(\gamma) \left[v(\gamma) - v(0) \right]\ d\gamma \right| \\
&\leq \int_{\mathcal{B}(0,\delta)} |\Psi_z(\gamma)|\, |v(\gamma) - v(0)|\ d\gamma + \int_{\mathbb{R}^2/\mathcal{B}(0,\delta)} |\Psi_z(\gamma)|\, |v(\gamma) - v(0)|\ d\gamma \\
&\leq \epsilon \int_{\mathcal{B}(0,\delta)} |\Psi_z(\gamma)|\ d\gamma + 2\, \|v\|_\infty \int_{\mathbb{R}^2/\mathcal{B}(0,\delta)} |\Psi_z(\gamma)|\ d\gamma \\
&= 2\pi \left\{ \epsilon \int_0^\delta |\tau_z(r)|\, r\ dr + 2\, \|v\|_\infty \int_\delta^{\bar{R}} |\tau_z(r)|\, r\ dr \right\}, \qquad \text{(A.32)}
\end{aligned}$$

for some finite $\bar{R}$. Note that in the step before last, the fact that $v \in \mathcal{C}_c(\mathbb{R}^2)$ (hence bounded) was exploited.

Let

$$\begin{aligned}
L\left(R_i, R_o, z\right) &:= \int_{R_i}^{R_o} \left|\tau_z(r)\right| r\ dr \\
&= \int_{R_i}^{R_o} \left|\frac{zq}{r^2+z^2}\left(\frac{-1}{\sqrt{r^2+z^2}}+\beta\right)e^{\beta\sqrt{r^2+z^2}}\right| r\ dr \\
&= |q| \int_{R_i}^{R_o} \left|\frac{-z}{\left(r^2+z^2\right)^{3/2}} + j\frac{z\sigma}{r^2+z^2}\right| r\ dr \\
&\leq |q| \left[\int_{R_i}^{R_o} \left|\frac{z}{\left(r^2+z^2\right)^{3/2}}\right| r\ dr + \sigma \int_{R_i}^{R_o} \left|\frac{z}{r^2+z^2}\right| r\ dr\right] \\
&= |q| \left[\int_{R_i}^{R_o} \frac{z}{\left(r^2+z^2\right)^{3/2}} r\ dr + \sigma \int_{R_i}^{R_o} \frac{z}{r^2+z^2} r\ dr\right] \\
&= |q| \left[I_1(R_i, R_o, z) + I_2(R_i, R_o, z)\right], \qquad \text{(A.33)}
\end{aligned}$$

where

$$I_1\left(R_i, R_o, z\right) := \int_{R_i}^{R_o} \frac{z}{\left(r^2+z^2\right)^{3/2}} r\ dr, \qquad \text{(A.34)}$$

$$I_2\left(R_i, R_o, z\right) := \sigma \int_{R_i}^{R_o} \frac{z}{r^2+z^2} r\ dr. \qquad \text{(A.35)}$$

Integrating (A.34) yields

$$\begin{aligned}
I_1\left(R_i, R_o, z\right) &= \int_{R_i}^{R_o} \frac{z}{\left(r^2+z^2\right)^{3/2}} r\ dr \\
&= -z\left[\frac{1}{\sqrt{R_o^2+z^2}} - \frac{1}{\sqrt{R_i^2+z^2}}\right]. \qquad \text{(A.36)}
\end{aligned}$$

Similarly with (A.35),

$$\begin{aligned}
I_2\left(R_i, R_o, z\right) &= \sigma \int_{R_i}^{R_o} \frac{z}{r^2+z^2} r\ dr \\
&= \frac{\sigma z}{2}\left[\ln\left(R_o^2+z^2\right) - \ln\left(R_i^2+z^2\right)\right] \\
&= \frac{\sigma z}{2} \ln\left(\frac{R_o^2+z^2}{R_i^2+z^2}\right). \qquad \text{(A.37)}
\end{aligned}$$

Substituting (A.36) and (A.37) into (A.33),

$$L\left(R_i, R_o, z\right) \leq |q| z \left[\frac{1}{\sqrt{R_i^2+z^2}} - \frac{1}{\sqrt{R_o^2+z^2}} + \frac{\sigma}{2}\ln\left(\frac{R_o^2+z^2}{R_i^2+z^2}\right)\right]. \qquad \text{(A.38)}$$

Note that

$$\lim_{R_i \to 0} I_1(R_i, R_o, z) = \frac{-z}{\sqrt{R_o^2 + z^2}} + 1 = I_1(0, R_o, z), \tag{A.39}$$

$$\lim_{z \to 0} I_1(0, R_o, z) = 1. \tag{A.40}$$

Similarly,

$$\lim_{R_i \to 0} I_2(R_i, R_o, z) = \frac{\sigma z}{2} \ln\left(\frac{R_o^2 + z^2}{z^2}\right) = I_2(0, R_o, z), \tag{A.41}$$

$$\begin{aligned} \lim_{z \to 0} I_2(0, R_o, z) &= \lim_{z \to 0} \frac{\sigma z}{2} \ln\left(\frac{R_o^2 + z^2}{z^2}\right) \\ &= \frac{\sigma}{2} \lim_{z \to 0} \left[\frac{\ln\left(\frac{R_o^2+z^2}{z^2}\right)}{\frac{1}{z}}\right] = \frac{\sigma}{2} \lim_{z \to 0} \left[\frac{\frac{z^2}{R_o^2+z^2}\frac{\left(-2R_o^2\right)}{z^3}}{\frac{-1}{z^2}}\right] \\ &= \sigma R_o^2 \lim_{z \to 0} \frac{z}{R_o^2 + z^2} = 0, \end{aligned} \tag{A.42}$$

where the step before last utilized *l'Hospital's Rule* [50].

Note that substituting (A.39) and (A.41) into (A.38) yields

$$L(0, R_o, z) \leq |q| \left[\frac{-z}{\sqrt{R_o^2 + z^2}} + 1 + \frac{\sigma z}{2} \ln\left(\frac{R_o^2 + z^2}{z^2}\right)\right]. \tag{A.43}$$

Using (A.40) and (A.42) in (A.38) produces

$$\lim_{z \to 0} L(0, \delta, z) \leq |q|, \tag{A.44}$$

$$\lim_{z \to 0} L(\delta, \bar{R}, z) \leq 0. \tag{A.45}$$

Combining (A.32), (A.38), and (A.43) gives

$$\begin{aligned} K(z) \leq\ & 2\pi\epsilon|q| \left\{1 - \frac{z}{\sqrt{\delta^2 + z^2}} + \frac{\sigma z}{2} \ln\left(\frac{\delta^2 + z^2}{z^2}\right) + \right. \\ & \left. 2z \|v\|_\infty \left[\frac{1}{\sqrt{\delta^2 + z^2}} - \frac{1}{\sqrt{\bar{R}^2 + z^2}} + \frac{\sigma}{2} \ln\left(\frac{\bar{R}^2 + z^2}{\delta^2 + z^2}\right)\right]\right\}. \end{aligned} \tag{A.46}$$

Using (A.44), (A.45), and the fact that

$$K(z) \leq 2\pi \left\{\epsilon L(0, \delta, z) + 2 \|v\|_\infty L(\delta, \bar{R}, z)\right\} \tag{A.47}$$

yields

$$\lim_{z \to 0} K(z) \leq 2\pi\epsilon|q|, \tag{A.48}$$

which holds for any $\epsilon > 0$. Therefore,

$$\lim_{z \to 0} K(z) \leq 0. \tag{A.49}$$

However, $K(z) \geq 0$, by definition. Then,

$$\lim_{z \to 0} K(z) = 0. \tag{A.50}$$

Hence, using (A.30)

$$\begin{aligned}
\lim_{\substack{z\to 0\\ z>0}} \int_{\mathbb{R}^2} \Psi_z(\gamma)v(\gamma)\ d\gamma &= \lim_{\substack{z\to 0\\ z>0}} \int_{\mathbb{R}^2} \Psi_z(\gamma)v(0)\ d\gamma \\
&= v(0) \lim_{\substack{z\to 0\\ z>0}} \int_{\mathbb{R}^2} \Psi_z(\gamma)\ d\gamma \\
&= -2\pi q v(0). \qquad \text{(A.51)}
\end{aligned}$$

■

Therefore, by letting $\beta := -j\frac{\omega}{c}$, $q := \frac{j\omega\rho_0}{2\pi}$, and $v(\gamma) := l(x, y)$, it is now clear that (2.17) solves the half-space equations (2.12), (2.13), and (2.14).

Appendix B

Converting Implicit State-Space Equations to Explicit Formulations

Consider the LTI system with implicit equations

$$\begin{bmatrix} \dot{\eta} \\ 0_q \end{bmatrix} = \begin{bmatrix} \hat{A} & \hat{B} \\ \hat{C} & \hat{D} \end{bmatrix} \begin{bmatrix} \eta \\ v \end{bmatrix}, \tag{B.1}$$

where $\hat{A} \in \mathbb{R}^{n\times n}$, $\hat{B} \in \mathbb{R}^{n\times m}$, $\hat{C} \in \mathbb{R}^{q\times n}$, $\hat{D} \in \mathbb{R}^{q\times m}$, $\dot{\eta} \in \mathbb{R}^n$, $\eta \in \mathbb{R}^n$, and $v \in \mathbb{R}^m$. Define $v := \begin{bmatrix} u \\ y \end{bmatrix}$, where $u \in \mathbb{R}^{m-q}$ and $y \in \mathbb{R}^q$. Then, $\hat{B} := \begin{bmatrix} \hat{B}_1 & \hat{B}_2 \end{bmatrix}$ and $\hat{D} := \begin{bmatrix} \hat{D}_1 & \hat{D}_2 \end{bmatrix}$ are appropriately partitioned. Therefore, the implicit equations are written as

$$\dot{\eta} = \hat{A}\eta + \hat{B}_1 u + \hat{B}_2 y \tag{B.2}$$

$$0_q = \hat{C}\eta + \hat{D}_1 u + \hat{D}_2 y. \tag{B.3}$$

Consider the explicit formulation where u is the input and y is the output so that

$$\dot{\eta} = A\eta + Bu \tag{B.4}$$

$$y = C\eta + Du. \tag{B.5}$$

If $\hat{D}_2$ is invertible, then (B.3) can written to resemble (B.5) as

$$y = -\hat{D}_2^{-1}\hat{C}\eta - \hat{D}_2^{-1}\hat{D}_1 u. \tag{B.6}$$

Substituting (B.6) into (B.2) and making (B.2) resemble (B.4) gives

$$\dot{\eta} = \hat{A}\eta + \hat{B}_1 u + \hat{B}_2(-\hat{D}_2^{-1}\hat{C}\eta - \hat{D}_2^{-1}\hat{D}_1 u) \tag{B.7}$$

$$= (\hat{A} - \hat{B}_2\hat{D}_2^{-1}\hat{C})\eta + (\hat{B}_1 - \hat{B}_2\hat{D}_2^{-1}\hat{D}_1)u. \tag{B.8}$$

Comparing (B.4) with (B.8) and (B.5) with (B.6) yields

$$A = \hat{A} - \hat{B}_2\hat{D}_2^{-1}\hat{C}, \tag{B.9}$$

$$B = \hat{B}_1 - \hat{B}_2\hat{D}_2^{-1}\hat{D}_1, \tag{B.10}$$

$$C = -\hat{D}_2^{-1}\hat{C}, \tag{B.11}$$

$$D = -\hat{D}_2^{-1}\hat{D}_1. \tag{B.12}$$

Appendix C

State-Space Extraction of a Blocking Zero

Lemma C.1 *Consider the single-input, multi output, LTI system given by*

$$\begin{bmatrix} \dot{x} \\ y \end{bmatrix} = \begin{bmatrix} A & B \\ C & D \end{bmatrix} \begin{bmatrix} x \\ u \end{bmatrix}, \tag{C.1}$$

where $A \in \mathbb{R}^{n\times n}$*,* $B \in \mathbb{R}^{n}$*,* $C \in \mathbb{R}^{n_y\times n}$*, and* $D \in \mathbb{R}^{n_y}$*. Suppose* A *is invertible (i.e. has no eigenvalues at 0) and*

$$-CA^{-1}B + D = 0_{n_y}, \tag{C.2}$$

i.e. the system has at least one blocking zero at $s = 0$*. Then, there exists* $E \in \mathbb{R}^{n_y\times n}$ *such that the system*

$$\begin{bmatrix} \dot{\eta} \\ y \end{bmatrix} = \begin{bmatrix} A & B \\ E & 0_{n_y} \end{bmatrix} \begin{bmatrix} \eta \\ \dot{u} \end{bmatrix} \tag{C.3}$$

relates the same input-output pair (u, y) *as (C.1).*

Proof: From (C.2),

$$\begin{bmatrix} A & B \\ C & D \end{bmatrix} \begin{bmatrix} -A^{-1}B \\ 1 \end{bmatrix} = 0_{n+n_y}. \tag{C.4}$$

Hence,

$$\operatorname{rank}\begin{bmatrix} A & B \\ C & D \end{bmatrix} \le n. \tag{C.5}$$

By virtue of it dimension, $\begin{bmatrix} A & B \\ C & D \end{bmatrix}$ has a left null space of dimension at least $n_y - 1$. Actually, it has a left null space of dimension at least n_y, since it is rank deficient.

Consider the matrices $V_1 \in \mathbb{R}^{n_y \times n}$ and $V_2 \in \mathbb{R}^{n_y \times n_y}$ such that $[V_1\ V_2]$ has full row rank and

$$\begin{bmatrix} V_1 & V_2 \end{bmatrix} \begin{bmatrix} A & B \\ C & D \end{bmatrix} = 0_{n_y \times (n+1)}. \tag{C.6}$$

Then,

$$V_1 \begin{bmatrix} A & B \end{bmatrix} + V_2 \begin{bmatrix} C & D \end{bmatrix} = 0_{n_y \times (n+1)}. \tag{C.7}$$

Note that V_2 is invertible. If not, there exists a nonzero vector $w \in \mathbb{R}^{n_y}$ such that

$$w^T V_2 = 0_{1 \times n_y}. \tag{C.8}$$

Then, left-multiplying (C.7) by w^T gives

$$w^T V_1 \begin{bmatrix} A & B \end{bmatrix} = 0_{1 \times (n+1)}. \tag{C.9}$$

Since $[V_1\ V_2]$ has full row rank,

$$w^T V_1 \neq 0_{1 \times n}. \tag{C.10}$$

However, A has no eigenvalues at 0. Therefore, (C.9) is a contradiction. Hence, V_2 is invertible.

Then, (C.7) can be written as

$$-V_2^{-1} V_1 \begin{bmatrix} A & B \end{bmatrix} = \begin{bmatrix} C & D \end{bmatrix}. \tag{C.11}$$

Let $E := -V_2^{-1} V_1$ and $\eta := \dot{x}$. Using (C.11),

$$y = \begin{bmatrix} C & D \end{bmatrix} \begin{bmatrix} x \\ u \end{bmatrix} = E \begin{bmatrix} A & B \end{bmatrix} \begin{bmatrix} x \\ u \end{bmatrix} = E\dot{x} = E\eta. \tag{C.12}$$

Differentiating the state equation in (C.1) yields

$$\dot{\eta} = A\eta + B\dot{u}. \tag{C.13}$$

Finally,

$$\begin{bmatrix} \dot{\eta} \\ y \end{bmatrix} = \begin{bmatrix} A & B \\ E & 0_{n_y} \end{bmatrix} \begin{bmatrix} \eta \\ \dot{u} \end{bmatrix}. \tag{C.14}$$

■

Appendix D

Transfer Functions for the Vented Loudspeaker Model Example

D.1 The Acoustic Half-Space

From Chapter 5, let H_1 and $\tilde{H}_2$ be written as

$$H_1 := \left[\begin{array}{c|c} A_{H_1} & B_{H_1} \\ \hline C_{H_1} & D_{H_1} \end{array}\right], \quad \tilde{H}_2 := \left[\begin{array}{c|c} A_{\tilde{H}_2} & B_{\tilde{H}_2} \\ \hline C_{\tilde{H}_2} & D_{\tilde{H}_2} \end{array}\right]. \tag{D.1}$$

The entries of the matrices are given by tables on the following pages. Note that $A_{H_1} = A_{\tilde{H}_2} =: A_H$ and has the form $A_H := \operatorname{diag}(A_{H_1}, A_{H_2}, \ldots, A_{H_{27}})$, i.e. it is block-diagonal with entries A_{H_i} given in Tables D.1 and D.2 (see Chapters 2 and 5 and Appendix C). Tables D.3 and D.4 give B_{H_1} and $B_{\tilde{H}_2}$, respectively. Also, C_{H_1} is given in Tables D.5 and D.6, while $C_{\tilde{H}_2}$ is found in Tables D.7 and D.8. Table D.9 shows the elements of both D_{H_1} and $D_{\tilde{H}_2}$.

Table D.1: The Elements of $A_H := \mathrm{diag}\left(A_{H_1}, A_{H_2}, \ldots, A_{H_{27}}\right)$ (Elements 1 to 19)

i	A_{H_i}
1	$-3.623 \times 10^{+03}$
2	$-4.236 \times 10^{+03}$
3	$\begin{bmatrix} -3.420 \times 10^{+03} & -3.539 \times 10^{+03} \\ 3.539 \times 10^{+03} & -3.420 \times 10^{+03} \end{bmatrix}$
4	$\begin{bmatrix} -4.351 \times 10^{+03} & -2.408 \times 10^{+03} \\ 2.408 \times 10^{+03} & -4.351 \times 10^{+03} \end{bmatrix}$
5	$\begin{bmatrix} -4.043 \times 10^{+03} & -3.174 \times 10^{+03} \\ 3.174 \times 10^{+03} & -4.043 \times 10^{+03} \end{bmatrix}$
6	$\begin{bmatrix} -3.451 \times 10^{+03} & -6.464 \times 10^{+03} \\ 6.464 \times 10^{+03} & -3.451 \times 10^{+03} \end{bmatrix}$
7	$\begin{bmatrix} -2.998 \times 10^{+03} & -7.399 \times 10^{+03} \\ 7.399 \times 10^{+03} & -2.998 \times 10^{+03} \end{bmatrix}$
8	$\begin{bmatrix} -7.456 \times 10^{+03} & -3.515 \times 10^{+03} \\ 3.515 \times 10^{+03} & -7.456 \times 10^{+03} \end{bmatrix}$
9	$\begin{bmatrix} -3.058 \times 10^{+03} & -8.295 \times 10^{+03} \\ 8.295 \times 10^{+03} & -3.058 \times 10^{+03} \end{bmatrix}$
10	$-9.884 \times 10^{+03}$
11	$\begin{bmatrix} -2.690 \times 10^{+03} & -9.972 \times 10^{+03} \\ 9.972 \times 10^{+03} & -2.690 \times 10^{+03} \end{bmatrix}$
12	$\begin{bmatrix} -5.403 \times 10^{+03} & -9.556 \times 10^{+03} \\ 9.556 \times 10^{+03} & -5.403 \times 10^{+03} \end{bmatrix}$
13	$\begin{bmatrix} -8.755 \times 10^{+03} & -6.867 \times 10^{+03} \\ 6.867 \times 10^{+03} & -8.755 \times 10^{+03} \end{bmatrix}$
14	$-1.127 \times 10^{+04}$
15	$\begin{bmatrix} -5.061 \times 10^{+03} & -1.127 \times 10^{+04} \\ 1.127 \times 10^{+04} & -5.061 \times 10^{+03} \end{bmatrix}$
16	$\begin{bmatrix} -5.044 \times 10^{+03} & -1.130 \times 10^{+04} \\ 1.130 \times 10^{+04} & -5.044 \times 10^{+03} \end{bmatrix}$
17	$\begin{bmatrix} -6.497 \times 10^{+03} & -1.545 \times 10^{+04} \\ 1.545 \times 10^{+04} & -6.497 \times 10^{+03} \end{bmatrix}$
18	$\begin{bmatrix} -3.726 \times 10^{+03} & -2.147 \times 10^{+04} \\ 2.147 \times 10^{+04} & -3.726 \times 10^{+03} \end{bmatrix}$
19	$\begin{bmatrix} -4.985 \times 10^{+03} & -2.547 \times 10^{+04} \\ 2.547 \times 10^{+04} & -4.985 \times 10^{+03} \end{bmatrix}$

Table D.2: The Elements of $A_H := \mathrm{diag}\left(A_{H_1}, A_{H_2}, \ldots, A_{H_{27}}\right)$ (Elements 20 to 27)

i	A_{H_i}
20	$-3.038 \times 10^{+04}$
21	$\begin{bmatrix} -2.495 \times 10^{+04} & -3.670 \times 10^{+04} \\ 3.670 \times 10^{+04} & -2.495 \times 10^{+04} \end{bmatrix}$
22	$\begin{bmatrix} -1.629 \times 10^{+04} & -5.443 \times 10^{+04} \\ 5.443 \times 10^{+04} & -1.629 \times 10^{+04} \end{bmatrix}$
23	$\begin{bmatrix} -5.805 \times 10^{+04} & -2.551 \times 10^{+04} \\ 2.551 \times 10^{+04} & -5.805 \times 10^{+04} \end{bmatrix}$
24	$\begin{bmatrix} -2.538 \times 10^{+04} & -6.135 \times 10^{+04} \\ 6.135 \times 10^{+04} & -2.538 \times 10^{+04} \end{bmatrix}$
25	$\begin{bmatrix} -1.718 \times 10^{+04} & -7.811 \times 10^{+04} \\ 7.811 \times 10^{+04} & -1.718 \times 10^{+04} \end{bmatrix}$
26	$\begin{bmatrix} -4.447 \times 10^{+04} & -7.968 \times 10^{+04} \\ 7.968 \times 10^{+04} & -4.447 \times 10^{+04} \end{bmatrix}$
27	$-5.723 \times 10^{+05}$

Table D.3: The Elements of B_{H_1}

Row	Row Elements	Row	Row Elements
1	$-9.954 \times 10^{+02}$	25	$-1.048 \times 10^{+02}$
2	0	26	$3.216 \times 10^{+02}$
3	$-8.899 \times 10^{+02}$	27	0
4	$-6.384 \times 10^{+02}$	28	0
5	$-2.213 \times 10^{+04}$	29	0
6	$-1.478 \times 10^{+04}$	30	0
7	0	31	$1.808 \times 10^{+03}$
8	0	32	$-2.871 \times 10^{+03}$
9	0	33	0
10	0	34	0
11	$-3.908 \times 10^{+02}$	35	$1.612 \times 10^{+05}$
12	$2.294 \times 10^{+02}$	36	$6.148 \times 10^{+04}$
13	0	37	$3.124 \times 10^{+04}$
14	0	38	$2.151 \times 10^{+03}$
15	$2.015 \times 10^{+03}$	39	$3.710 \times 10^{+03}$
16	$-6.086 \times 10^{+02}$	40	0
17	0	41	0
18	0	42	$-1.241 \times 10^{+02}$
19	0	43	$1.222 \times 10^{+03}$
20	$6.369 \times 10^{+03}$	44	$7.201 \times 10^{+03}$
21	$4.330 \times 10^{+03}$	45	$-7.127 \times 10^{+03}$
22	0	46	0
23	0	47	0
24	$-1.141 \times 10^{+04}$	48	$-8.154 \times 10^{+02}$

Table D.4: The Elements of $B_{\tilde{H}_2}$

Row	Row Elements	Row	Row Elements
1	0	25	0
2	-7.038	26	0
3	0	27	2.846
4	0	28	-8.662×10^{-01}
5	0	29	-5.886
6	0	30	-3.125
7	2.857	31	0
8	4.056	32	0
9	-5.722×10^{-01}	33	8.625×10^{-02}
10	3.533×10^{-01}	34	-6.978×10^{-01}
11	0	35	0
12	0	36	0
13	-5.738	37	0
14	-9.355	38	0
15	0	39	0
16	0	40	-2.050
17	$9.625 \times 10^{+01}$	41	2.021
18	4.387×10^{-02}	42	0
19	1.123×10^{-02}	43	0
20	0	44	0
21	0	45	0
22	$5.069 \times 10^{+01}$	46	-2.863×10^{-02}
23	$3.751 \times 10^{+01}$	47	3.811×10^{-01}
24	0	48	0

Table D.5: The Elements of C_{H_1} (Columns 1 to 37)

Column	Column Elements (4 per column)			
1	0	0	0	$9.998 \times 10^{+01}$
2	0	0	-6.949	0
3	0	0	0	$5.881 \times 10^{+01}$
4	0	0	0	$-1.250 \times 10^{+02}$
5	0	0	$-1.498 \times 10^{+01}$	0
6	0	0	$1.360 \times 10^{+01}$	0
7	0	0	-3.048	0
8	0	0	$-1.152 \times 10^{+01}$	0
9	0	0	$-1.508 \times 10^{+01}$	0
10	0	0	-7.829	0
11	0	0	0	$-7.590 \times 10^{+01}$
12	0	0	0	$3.809 \times 10^{+01}$
13	0	0	0	3.714
14	0	0	0	-3.786
15	0	0	$-3.478 \times 10^{+01}$	0
16	0	0	9.139	0
17	$1.423 \times 10^{+01}$	0	0	0
18	0	0	$2.334 \times 10^{+01}$	0
19	0	0	-5.347	0
20	$-2.850 \times 10^{+02}$	0	0	0
21	$2.956 \times 10^{+03}$	0	0	0
22	$-1.017 \times 10^{+01}$	0	0	0
23	$-2.024 \times 10^{+01}$	0	0	0
24	$2.714 \times 10^{+03}$	0	0	0
25	0	0	0	$2.433 \times 10^{+01}$
26	0	0	0	$7.796 \times 10^{+01}$
27	0	0	0	-6.854×10^{-01}
28	0	0	0	-1.910
29	$2.352 \times 10^{+01}$	0	0	0
30	$-2.471 \times 10^{+01}$	0	0	0
31	$1.898 \times 10^{+03}$	0	0	0
32	$-9.277 \times 10^{+02}$	0	0	0
33	$4.944 \times 10^{+01}$	0	0	0
34	$-1.866 \times 10^{+01}$	0	0	0
35	0	$-1.473 \times 10^{+02}$	0	0
36	0	$-1.335 \times 10^{+02}$	0	0
37	0	$2.735 \times 10^{+02}$	0	0

Table D.6: The Elements of C_{H_1} (Columns 38 to 48)

Column	Column Elements (4 per column)			
38	$-2.478 \times 10^{+03}$	0	0	0
39	$1.771 \times 10^{+03}$	0	0	0
40	0	$-3.891 \times 10^{+02}$	0	0
41	0	$-7.074 \times 10^{+02}$	0	0
42	0	0	$-1.695 \times 10^{+02}$	0
43	0	0	$2.103 \times 10^{+02}$	0
44	0	$5.481 \times 10^{+02}$	0	0
45	0	$1.996 \times 10^{+01}$	0	0
46	0	$1.774 \times 10^{+02}$	0	0
47	0	$1.148 \times 10^{+03}$	0	0
48	0	0	0	$-7.601 \times 10^{+02}$

Table D.7: The Elements of $C_{\tilde{H}_2}$ (Columns 1 to 23)

Column	Column Elements (4 per column)			
1	0	0	0	$9.998 \times 10^{+01}$
2	0	0	-6.939	0
3	0	0	0	$5.881 \times 10^{+01}$
4	0	0	0	$-1.250 \times 10^{+02}$
5	0	0	$-1.496 \times 10^{+01}$	0
6	0	0	$1.358 \times 10^{+01}$	0
7	0	0	-3.044	0
8	0	0	$-1.151 \times 10^{+01}$	0
9	0	0	$-1.506 \times 10^{+01}$	0
10	0	0	-7.818	0
11	0	0	0	$-7.590 \times 10^{+01}$
12	0	0	0	$3.809 \times 10^{+01}$
13	0	0	0	3.714
14	0	0	0	-3.786
15	0	0	$-3.473 \times 10^{+01}$	0
16	0	0	9.126	0
17	$1.400 \times 10^{+01}$	0	0	0
18	0	0	$2.331 \times 10^{+01}$	0
19	0	0	-5.339	0
20	$-2.805 \times 10^{+02}$	0	0	0
21	$2.910 \times 10^{+03}$	0	0	0
22	$-1.001 \times 10^{+01}$	0	0	0
23	$-1.992 \times 10^{+01}$	0	0	0

Table D.8: The Elements of $C_{\tilde{H}_2}$ (Columns 24 to 48)

Column	Column Elements (4 per column)			
24	$2.671 \times 10^{+03}$	0	0	0
25	0	0	0	$2.433 \times 10^{+01}$
26	0	0	0	$7.796 \times 10^{+01}$
27	0	0	0	-6.854×10^{-01}
28	0	0	0	-1.910
29	$2.315 \times 10^{+01}$	0	0	0
30	$-2.432 \times 10^{+01}$	0	0	0
31	$1.868 \times 10^{+03}$	0	0	0
32	$-9.130 \times 10^{+02}$	0	0	0
33	$4.866 \times 10^{+01}$	0	0	0
34	$-1.836 \times 10^{+01}$	0	0	0
35	0	$-1.589 \times 10^{+02}$	0	0
36	0	$-1.440 \times 10^{+02}$	0	0
37	0	$2.949 \times 10^{+02}$	0	0
38	$-2.439 \times 10^{+03}$	0	0	0
39	$1.743 \times 10^{+03}$	0	0	0
40	0	$-4.197 \times 10^{+02}$	0	0
41	0	$-7.629 \times 10^{+02}$	0	0
42	0	0	$-1.692 \times 10^{+02}$	0
43	0	0	$2.100 \times 10^{+02}$	0
44	0	$5.911 \times 10^{+02}$	0	0
45	0	$2.152 \times 10^{+01}$	0	0
46	0	$1.913 \times 10^{+02}$	0	0
47	0	$1.238 \times 10^{+03}$	0	0
48	0	0	0	$-7.601 \times 10^{+02}$

Table D.9: The Elements of D_{H_1} and $D_{\tilde{H}_2}$

Elements of D_{H_1}	
Row	Row Elements
1	$2.196\times10^{+02}$
2	$3.266\times10^{+02}$
3	$2.704\times10^{+01}$
4	-8.911×10^{-01}

Elements of $D_{\tilde{H}_2}$	
Row	Row Elements
1	0
2	0
3	0
4	0

D.2 The Uncertainty and Performance Weights

Let the uncertainty and performance weights, given in Chapter 5, be written as

$$W_\Delta := \left[\begin{array}{c|c} A_{W_\Delta} & B_{W_\Delta} \\ \hline C_{W_\Delta} & D_{W_\Delta} \end{array}\right], \tag{D.2}$$

$$W_{err} := \left[\begin{array}{c|c} A_{W_{err}} & B_{W_{err}} \\ \hline C_{W_{err}} & D_{W_{err}} \end{array}\right], \tag{D.3}$$

$$W_{knoise} := \left[\begin{array}{c|c} A_{W_{knoise}} & B_{W_{knoise}} \\ \hline C_{W_{knoise}} & D_{W_{knoise}} \end{array}\right], \tag{D.4}$$

$$W_u := \left[\begin{array}{c|c} A_{W_u} & B_{W_u} \\ \hline C_{W_u} & D_{W_u} \end{array}\right], \tag{D.5}$$

$$\tag{D.6}$$

$$W_{ref} := 1. \tag{D.7}$$

The entries for the matrices (except for W_{ref}, since it is just a constant unit gain) are found on the following page.

Table D.10: The Elements of A_{W_Δ}

Row	Row Elements (5 per row)				
1	-4.500×10^{-01}	1.055×10^{+01}	-3.375×10^{+02}	-4.235×10^{+02}	-4.235×10^{+02}
2	0	-4.500×10^{-01}	-3.375×10^{+02}	-4.235×10^{+02}	-4.235×10^{+02}
3	0	0	-1.200×10^{+04}	-1.355×10^{+04}	-1.355×10^{+04}
4	0	0	0	-2.000×10^{+04}	-1.700×10^{+04}
5	0	0	0	0	-2.000×10^{+04}

Table D.11: The Elements of B_{W_Δ}, C_{W_Δ}, and D_{W_Δ}

Elements of B_{W_Δ}	
Row	Row Elements
1	-4.320×10^{+02}
2	-4.320×10^{+02}
3	-1.382×10^{+04}
4	-1.734×10^{+04}
5	-1.734×10^{+04}

Elements of C_{W_Δ}	
Column	Column Elements
1	−3.248
2	−3.248
3	1.039×10^{+02}
4	1.304×10^{+02}
5	1.304×10^{+02}

D_{W_Δ} = 1.330×10^{+02}

W_{err} =

$$\left[\begin{array}{cccc|c} -2.918\times10^{+01} & -2.266\times10^{+01} & 8.448\times10^{+01} & 4.816\times10^{+01} & -2.839 \\ 2.266\times10^{+01} & -1.324\times10^{+01} & -2.597\times10^{+01} & -1.481\times10^{+01} & 8.730\times10^{-01} \\ 0 & 0 & -9.970\times10^{+01} & -1.437\times10^{+02} & -9.331 \\ 0 & 0 & 1.437\times10^{+02} & -1.549\times10^{+02} & 5.319 \\ \hline 5.071 & 1.559 & -1.666\times10^{+01} & -9.498 & 5.600\times10^{-01} \end{array}\right]$$

$$W_{knoise} = \left[\begin{array}{ccc|c} -2.028\times10^{+01} & -3.844\times10^{+01} & -3.443\times10^{+03} & -3.747\times10^{-03} \\ 3.844\times10^{+01} & -5.042\times10^{+01} & 2.546\times10^{+03} & 2.770\times10^{-03} \\ 0 & 0 & -2.000\times10^{+04} & -2.068\times10^{-02} \\ \hline -2.498\times10^{+01} & -1.847\times10^{+01} & 1.378\times10^{+02} & 1.500\times10^{-04} \end{array}\right]$$

$$W_u = \left[\begin{array}{ccc|c} -1.000\times10^{-03} & -6.828\times10^{+01} & -1.918\times10^{+01} & -4.189\times10^{-01} \\ 0 & -3.740\times10^{+03} & -2.780\times10^{+03} & -3.014\times10^{+01} \\ 0 & 2.780\times10^{+03} & -1.209\times10^{+03} & 8.466 \\ \hline -9.742\times10^{-01} & 7.009\times10^{+01} & 1.969\times10^{+01} & 4.300\times10^{-01} \end{array}\right]$$

Bibliography

[1] Khalid M. Al-Ali and Andy K. Packard. Control of closed-box loudspeaker systems. In Janos J. Gertler, Jose B. Cruz, Jr., Michael Peshkin, L. Basanez, F. Nicolo, and A. Ollero, editors, *Proceedings of the 13th IFAC World Congress*, volume A. Robotics, Components and Instruments, pages 481–486, San Francisco, CA, USA, June–July 1996. International Federation of Automatic Control.

[2] Brian D. O. Anderson and John B. Moore. *Optimal Control, Linear Quadratic Methods*. Prentice Hall, Englewood Cliffs, NJ, 1990.

[3] Mingsian R. Bai and Hsinping Wu. Robust control of a sensorless bass-enhanced moving-coil loudspeaker system. *Journal of the Acoustical Society of America*, 105(6):3283–3289, June 1999.

[4] G. J. Balas, John C. Doyle, K. Glover, Andrew K. Packard, and Roy Smith. *μ-Analysis and Synthesis Toolbox*. The MathWorks, Natick, MA, USA, January 1994.

[5] A. Bellini, G. Cibelli, E. Ugolotti, A. Farina, and C. Morandi. Non-linear digital audio processor for dedicated loudspeaker systems. *IEEE Transactions on Consumer Electronics*, 44(3):1024–1031, August 1998.

[6] Samir Bennani, Bob J. A. Mulder, and Ton J. J.vd Weiden. Design of an integrated autopilot/autothrottle using μ-synthesis. In O. H. Bosgra and P. M. J. Van den Hof, editors, *Selected Topics in Identification, Modeling and Control*,

volume 6 of *Progress Report on Research Activities in the Mechanical Engineering Systems and Control Group*, pages 95–106. Delft University Press, December 1993.

[7] Leo Leroy Beranek. *Acoustics*. McGraw-Hill, New York, NY, USA, 1954.

[8] H. S. Black. Stabilized feedback amplifiers. *The Bell System Technical Journal*, pages 1–18, January 1934.

[9] E. De Boer. Theory of motional feedback. *IRE Trans. Audio*, January–February 1961.

[10] Po-Rong Chang, C. G. Lin, and Bao-Fuh Yeh. Inverse filtering of a loudspeaker and room acoustics using time-delay neural networks. *Journal of the Acoustical Society of America*, 95(6):3400–3408, June 1994.

[11] D. de Greef and J. Vandewege. Acceleration feedback loudspeaker. *Wireless World*, 87(1548):32–36, September 1981.

[12] Ruurd de Vries, Arthur P. Berkhoff, Cornelis H. Slump, and Otto E. Herrmann. Digital compensation of nonlinear distortion in loudspeakers. In *Proceedings of the 1993 IEEE International Conference on Acoustics, Speech, and Signal Processing*, volume 1, pages 165–168, Minneapolis, MN, USA, April 1993.

[13] C. A. Desoer and M. Vidyasagar. *Feedback Systems: Input-Output Properties*. Electrical Science Series. Academic Press, New York, NY, USA, 1975.

[14] C. A. Desoer and Y. T. Wang. Foundations of feedback theory for nonlinear dynamical systems. *IEEE Transactions on Circuits and Systems*, 1979.

[15] John C. Doyle. Analysis of feedback systems with structured uncertainties. In *IEE Proceedings D (Control Theory and Applications)*, volume 129, pages 242–250, November 1982.

[16] John C. Doyle, Bruce A. Francis, and Allen R. Tannenbaum. *Feedback Control Theory*. Macmillan, New York, NY, USA, 1992.

[17] John C. Doyle, K. Glover, P. Khargonekar, and B.A. Francis. State-space solutions to standard $\mathcal{H}_2$ and $\mathcal{H}_\infty$ control problems. In *Proceedings of the 1988 American Control Conference*, volume 2, pages 1691–1696, Atlanta, GA, USA, June 1988.

[18] John C. Doyle and Gunter Stein. Multivariable feedback design: Concepts for a classical/modern synthesis. *IEEE Transactions on Automatic Control*, AC-26:4–16, 1981.

[19] Louis D. Fielder and Eric M. Benjamin. Subwoofer performance for accurate reproduction of music. *Journal of the Audio Engineering Society*, 36(6):443–456, June 1988.

[20] Bruce. A. Francis. *A Course in $\mathcal{H}_\infty$ Control Theory*. Lecture Notes in Control and Information Sciences; 88. Springer-Verlag, New York, NY, USA, 1987.

[21] Walter Frank, Rita Reger, and Ulrich Appel. Loudspeaker nonlinearities-analysis and compensation. In *Conference Record of The Twenty-Sixth Asilomar Conference on Signals, Systems and Computers*, volume 2, pages 756–760, Pacific Grove, CA, USA, October 1992.

[22] Gene F. Franklin, J. David Powell, and Abbas Emami-Naeini. *Feedback Control of Dynamic Systems*. Addison-Wesley Series in Electrical and Computer Engineering: Control Engineering. Addison-Wesley, Reading, MA, USA, second edition, 1991.

[23] Franklin X. Y. Gao and W. Martin Snelgrove. Adaptive linearization of a loudspeaker. In *1991 International Conference on Acoustics, Speech and Signal Processing*, volume 5, pages 3589–3592, Toronto, Ont., Canada, April 1991.

[24] R. A. Greiner and Travis M. Sims, Jr. Loudspeaker distortion reduction. *Journal of the Audio Engineering Society*, 32(12):956–963, December 1984.

[25] Hewlett-Packard Company, 8600 Soper Hill Road, Everett, WA 98205, USA. *HP 35660A Operating Manual Set*, July 1988.

[26] Jeongho Hong, James C. Akers, Ravinder Venugopal, Miin-Nan Lee, Andrew G. Sparks, Peter D. Washabaugh, and Dennis S. Bernstein. Modeling, identification, and feedback control of noise in an acoustic duct. *IEEE Transactions on Control Systems Technology*, 4(3):283–291, May 1996.

[27] Jose B. Cruz Jr. *Feedback Systems*, volume 14 of *Inter-University Electronics Series*, chapter 3, pages 66–98. McGraw-Hill, New York, NY, USA, 1972.

[28] A. J. M. Kaizer. Modeling of the nonlinear response of an electrodynamic loudspeaker by a volterra series expansion. *Journal of the Audio Engineering Society*, 35(6):421–433, June 1987.

[29] Lawrence Kinsler, Austin R. Frey, Alan B. Coppens, and James V. Sanders. *Fundamentals of Acoustics*. John Wiley & Sons, Toronto, Canada, third edition, 1982.

[30] J. A. Klaassen and S. H. de Koning. Motional feedback with loudspeakers. *Phillips Tech. Rev.*, 28(5):148–157, 1968.

[31] Wolfgang Klippel. Dynamic measurement and interpretation of the nonlinear parameters of electrodynamic loudspeakers. *Journal of the Audio Engineering Society*, 38(12):944–955, December 1990.

[32] Wolfgang Klippel. The mirror filter-a new basis for reducing nonlinear distortion and equalizing response in woofer systems. *Journal of the Audio Engineering Society*, 40(9):675–691, September 1992.

[33] Wolfgang Klippel. Nonlinear large-signal behavior of electrodynamic loudspeakers at low frequencies. *Journal of the Audio Engineering Society*, 40(6):483–496, June 1992.

[34] Wolfgang Klippel. Direct feedback linearization of nonlinear loudspeaker systems. *Journal of the Audio Engineering Society*, 46(6):499–507, June 1998.

[35] Erwin Kreyszig. *Advanced Engineering Mathematics*. John Wiley & Sons, New York, NY, USA, seventh edition, 1993.

[36] Joji Kuriyama and Yasuyuki Furukawa. Adaptive loudspeaker system. *Journal of the Audio Engineering Society*, 37(11):919–926, November 1989.

[37] Steven A. Lane and Robert L. Clark. Active control of a reverberant enclosure using an approximate constant volume velocity source. In *Proceedings of the 1998 American Control Conference. ACC*, volume 4, pages 2606–2610, Philadelphia, PA, USA, June 1998.

[38] Steven A. Lane and Robert L. Clark. Improving loudspeaker performance for active noise control applications. *Journal of the Audio Engineering Society*, 46(6):508–519, June 1998.

[39] Leonard Meirovitch. *Analytical Methods in Vibrations*. Macmillan Series in Applied Mechanics. Macmillan, New York, NY, USA, 1967.

[40] Ben Nobel and James W. Daniel. *Applied Linear Algebra*. Prentice-Hall, Englewood Cliffs, NJ, third edition, 1988.

[41] James F. Novak. Performance of enclosures for low resonance high compliance loudspeakers. *Journal of the Audio Engineering Society*, 7:29–37, 1959.

[42] Alan V. Oppenheim, Alan S. Willsky, and Ian T. Young. *Signals and Systems*. Prentice Hall, Englewood Cliffs, NJ, USA, 1983.

[43] Andrew Packard, John Doyle, and Gary Balas. Linear, multivariable robust control with a μ perspective. *Transactions of the ASME. Journal of Dynamic Systems, Measurement and Control*, 115(2B):426–438, June 1993.

[44] Allan D. Pierce. *Acoustics: An Introduction to Its Physical Principles and Applications*. McGraw Hill, New York, NY, USA, 1981.

[45] Edward M. Purcell. *Electricity and Magnetism*. Berkeley physics course v. 2. McGraw-Hill, New York, NY, USA, second edition, 1985.

[46] Michael Renardy. *An Introduction to Partial Differential Equations*. Texts in Applied Mathematics; 13. Springer-Verlag, New York, NY, USA, 1993.

[47] William C. Reynolds and Henry C. Perkins. *Engineering Thermodynamics*. McGraw-Hill, New York, NY, USA, second edition, 1977.

[48] James K. Roberge. *Operational Amplifiers, Theory and Practice*, chapter 2, pages 21–32. John Wiley & Sons, New York, NY, USA, 1975.

[49] Mario Rossi. *Acoustics and Electroacoustics*. Artech House, 1988.

[50] Walter Rudin. *Principles of Mathematical Analysis*. International Series in Pure and Applied Mathematics. McGraw-Hill, Inc., New York, NY, USA, third edition, 1972.

[51] Shankar Sastry. *Nonlinear Systems: Analysis, Stability, and Control*. Interdisciplinary Applied Mathematics; V. 10. Springer-Verlag, New York, NY, USA, 1999.

[52] H. Schurer, A. G. J. Nijmeijer, M. A. Boer, C. H. Slump, and O. E. Herrmann. Identification and compensation of the electrodynamic transducer nonlinearities. In *IEEE International Conference on Acoustics, Speech, and Signal Processing*, volume 3, pages 2381–2384, Munich, Germany, April 1997.

[53] Steven E. Schwarz and William G. Oldham. *Electrical Engineering: An Introduction*. Saunders College Publishing, Fort Worth, TX, second edition, 1993.

[54] Richard H. Small. Closed-box loudspeaker systems, part i: Analysis. *Journal of the Audio Engineering Society*, 20(10):798–808, December 1972.

[55] Richard H. Small. Direct-radiator loudspeaker system analysis. *Journal of the Audio Engineering Society*, 20(5):383–395, June 1972.

[56] Richard H. Small. Simplified loudspeaker measurements at low frequencies. *Journal of the Audio Engineering Society*, 20(1):28–33, January–February 1972.

[57] Richard H. Small. Closed-box loudspeaker systems, part ii: Synthesis. *Journal of the Audio Engineering Society*, 21(1):11–18, February 1973.

[58] K. E. Stahl. Synthesis of loudspeaker mechanical parameters by electrical means: A new method for controlling low-frequency loudspeaker behavior. *Journal of the Audio Engineering Society*, 29(9):587–596, September 1981.

[59] Gunter Stein and Michael Athans. The LQG/LTR procedure for multivariable feedback control design. *IEEE Transactions on Automatic Control*, AC-32:105–114, 1987.

[60] Gunter Stein and John C. Doyle. Beyond singular values and loop shapes. *Journal of Guidance, Control, and Dynamics*, 14(1):5–16, January–February 1991.

[61] Johan Suykens, Joos Vandewalle, and Johan van Ginderdeuren. Feedback linearization of nonlinear distortion in electrodynamic loudspeakers. *Journal of the Audio Engineering Society*, 43(9):690–694, September 1995.

[62] R. L. Tanner. Improving loudspeaker response with motional feedback. *Electronics*, (142):228–240, March 1951.

[63] Peter W. Tappan. Analysis of a low-frequency loudspeaker system. *Journal of the Audio Engineering Society*, 7(1):38–46, January 1959.

[64] A. N. Thiele. Loudspeakers in vented boxes: Part 1. *Journal of the Audio Engineering Society*, 19(5):382–391, May 1971.

[65] A. N. Thiele. Loudspeakers in vented boxes: Part 2. *Journal of the Audio Engineering Society*, 19(6):471, June 1971.

[66] A. N. Thiele. Loudspeakers, enclosures and equalisers. In *Proceedings of the Institution of Radio and Electronics Engineers*, volume 34, pages 425–448, Australia, November 1973.

[67] Claire Tomlin, John Lygeros, Luca Benvenuti, and Shankar Sastry. Output tracking for a non-minimum phase dynamic CTOL aircraft model. In *Proceedings of the 34th IEEE Conference on Decision and Control*, volume 2, pages 1867–1872, New Orleans, LA, USA, December 1995.

[68] Benson H. Tongue. *Principles of Vibration*. Oxford University Press, New York, NY, USA, 1996.

[69] Kemin Zhou, John C. Doyle, and Keith Glover. *Robust and Optimal Control*. Prentice Hall, Upper Saddle River, NJ 07458, USA, 1995.